République Algérienne Démocratique et Populaire
Ministère de l'Enseignement Supérieur et de la Recherche Scientifique
Université A.MIRA-BEJAIA

جامعة بجاية
Tasdawit n Bgayet
Université de Béjaïa

Faculté de Technologie
Département de Génie Electrique
Laboratoire ou unité de recherche de rattachement : Laboratoire de Maîtrise des Energies Renouvelables

THÈSE

EN VUE DE L'OBTENTION DU DIPLOME DE DOCTORAT

Domaine : Sciences et Technologie Filière : Electrotechnique
Spécialité : Haute Tension et Réseaux Electriques

Présentée par
Yacine AYACHI AMOR

Thème

Contribution to Preventive Strategy for Harmonic Depollution in Grid-connected Photovoltaic System

Soutenue le : 22/10/2022 **Devant le Jury composé de :**

Nom et Prénom	**Grade**		
Mr Kassa IDJDARENE	Professeur	Univ. de Bejaia	Président
Mr Farid HAMOUDI	Professeur	Univ. de Bejaia	Rapporteur
Mr Gaëtan DIDIER	Maître de Conférences	Univ de Lorraine	Co-Rapporteur
Mr Hamid BENTARZI	Professeur	Univ. de Boumerdes	Examinateur
Mm Sofia BELAID	Professeur	Univ. de Bejaia	Examinateur
Mr Nabil TAIB	Professeur	Univ. de Bejaia	Examinateur

Année Universitaire : 2022/2023

Declaration

I hereby declare that the work presented in this thesis has not been submitted for any other degree or professional qualification and that it is the result of my own independent work.

This research is conducted at the *Laboratoire de Maitrise des Energies Renouvelables (LMER), Faculté de Technologie, Université de Bejaia, Bejaia, Algeria*.

Yacine AYACHI AMOR

Date: 2 February 2022

Publications

Relevant Publications

Journal articles:

- **Y. Ayachi Amor**, F. Hamoudi, F. Kheldoun, G. Didier, Z. Rabiai 'Fuzzy logic enhanced control for a single-stage grid-tied photovoltaic system with shunt active filtering capability' *International Transactions on Electrical Energy Systems*, 2021, 31(10), e13008. https://doi.org/10.1002/2050-7038.13008
- **Y. Ayachi Amor**, A. Kheldoun, B. Metidji, F. Hamoudi, A. Merazka, Y. Lazoueche 'Design and Implementation of Three-level T-type Inverter based on Simplified SVPWM Using cost-effective STM32F4 Board', *Int. J. Digital Signals and Smart Systems*, 2021, Vol. 5, No. 1, pp.20–39. http://dx.doi.org/10.1504/IJDSSS.2021.10034968
- **Y. Ayachi Amor**, F. Hamoudi, A. Kheldoun, 'Three-phase Three-level Inverter Grid-tied PV System with Fuzzy Logic Control based MPPT', *Algerian Journal of Signals and Systems*, Vol.3, Issue 3, September 2018. pp: 96-105. https://doi.org/10.51485/ajss.v3i3.65

Conference papers:

- **Y. Ayachi Amor**, C. Dekari, S. Dehmani, A. Kheldoun , B. Metidji, F. Hamoudi, A. Ammar, A. Slami, 'Design and Implementation of Shunt Active Power Filter using STM32F4 Board' *The Electrical Engineering International Conference EEIC'19*, Bejaia, Algeria, 2019, pp. 0–4.
- **Y. Ayachi Amor**, A. Kheldoun, B. Metidji, F. Hmoudi, A. Merazka, Y. Lazoueche 'Implementation of Modified SVPWM for Three-level Inverter Using STM32F4', *3rd International Conference on Electrical Sciences and Technologies in Maghreb (CISTEM 2018)*, 28-31 Oct 2018 Algiers, ALGERIA. https://ieeexplore.ieee.org/document/8613592

Other Publications

Books:

- **Y. Ayachi Amor**, N. Ayachi Amor, and A. Kheldoun 'Design of Grid Connected Photovoltaic System' *LAP LAMBERT Academic Publishing*, May 2018, ISBN: 978-613-9-82929-3.

Journal articles:

- **Y. Ayachi Amor**, G. Didier, F. Hamoudi, T. LUBIN, 'Application of a Novel Approach of Resistive Type Superconducting Fault Current Limiter with a Fast Protection System in Multi-terminal DC Network' *International Transactions on Electrical Energy Systems*, 30(10) 2020; e12568. https://doi.org/10.1002/2050-7038.12568

- **Y. Ayachi Amor**, G. Didier, F. Hamoudi ‘Protection of MTDC Network using a Resistive Type Superconducting Fault Current Limiter’ *European Journal of Electrical Engineering* 23(6) PP: 475-480, 2021. https://doi.org/10.18280/ejee.230607
- **Y. Ayachi Amor**, G. Didier, J. Lévêque, F. Hamoudi, ‘Study on the Alliance between SFCL and Hybrid DC Circuit Breaker for Protecting HVDC Grid’ *Journal of Physics Conference Series* 1559(1) pp:1-8, 2020. https://doi.org/10.1088/1742-6596/1559/1/012102
- A. Slami, **Y. Ayachi Amor**, 'Transmission of Sound via a Perovskite Solar Cell', *INTERNATIONAL JOURNAL OF ENERGY*, Vol. 14, pp.83-87, 2020. http://doi.org/10.46300/91010.2020.14.12
- B. Deffaf, F. Hamoudi, N. Debdouche, **Y. Ayachi Amor**, S. Medjmadj ‘Super-twisting Sliding Mode Control for a Multifunctional Double Stage Grid-connected Photovoltaic System’ *Advances in Electrical and Electronic Engineering*, 20(3) PP:240 – 249, 2022, 10.15598/aeee.v20i3.4454.

Conference papers:

- **Y. Ayachi Amor**, G. Didier, J. Lévêque, F. Hamoudi, ‘Study the Alliance between SFCL and Hybrid DC Breaker for Protecting HVDC Grid’ *14th European Conference on Applied Superconductivity (EUCAS 2019)*, 1st-5th September 2019, SEC, Glasgow, Scotland, UK.
- **Y. Ayachi Amor**, G. Didier, F. Hamoudi, ‘Study the Impact of Superconducting Fault Current Limiter in Multi-terminal DC Grid’ *19th International Symposium on Electromagnetic Fields in Mechatronics, Electrical and Electronic Engineering (ISEF2019)*, Nancy-France, 29-31 August 2019. https://ieeexplore.ieee.org/document/9096968
- **Y. Ayachi Amor**, N. Ayachi Amor, H. Bentarzi, F. Hamoudi, ‘Implementation of a Numerical Overcurrent Relay Using LabVIEW and Acquisition Card’, *3rd International Conference on Electrical Sciences and Technologies in Maghreb (CISTEM 2018)*, 28-31 Oct 2018, Algiers, ALGERIA. https://ieeexplore.ieee.org/document/8613455
- N. Ayachi amor, **Y. Ayachi Amor**, A. Kheldoun, B. Metidji ‘Comprehensive modeling and simulation of grid-tied PV system’ *5th International Conference on Electrical Engineering - Boumerdes (ICEEB),* Boumerdes, Algeria, 2017, pp. 1–6. http://ieeexplore.ieee.org/document/8191994/
- **Y. Ayachi Amor**, N. Ayachi Amor, A. Kheldoun, B. Metidji, ‘Design and Implementation of Three-Level Inverter for Grid-tied PV Systems’ *5th International Conference on Electrical Engineering - Boumerdes (ICEEB)*, Boumerdes, Algeria, 2017, pp. 0–5. http://ieeexplore.ieee.org/document/8191993/

Acknowledgements

In the name of Allah the Most Beneficent and the Most Merciful, we thank Allah for all His blessing and strength that He gives us for completing this modest thesis.

Then, I would like to express my deepest and sincere gratitude to our project Supervisor ***Pr. Farid HAMOUDI*** *and Co-supervisor* ***Dr. Gaëtan DIDIER*** *for their insightful guidance, constant assistance, and fruitful advice that offered during my PhD project until it was completed.*

Also, it is my duty to thank all the people who contributed in any shape of form to this work, I mention here in particular:
My Master's Supervisors ***Pr. Aissa KHELDOUN*** *and* ***Dr. Brahim METIDJI*** *for their help and constant support.*
Mr. Zakaria RABIAI *for his help regarding the PIL test.*

*I would like also to thank my Ph.D mates**: Nourddine AYACHI AMOR, Fares BENCHEIKH, ROUANI Lahcene, Youcef GRAINAT, Zakaria RABIAI, Walid TOUZOUT, Walid SAHRAOUI, Adel OUBELAID, and Matteo SCANZANO*** *for their help and encouragement.*

Finally yet importantly, I would like to acknowledge the help and support of ***my beloved family*** *members for their constant encouragement and moral support with patience and full understanding.*

Yacine AYACHI AMOR

Dedications

I have great pleasure to dedicate this modest work

*To the soul of my sister "**Kawther**" and my Grandfather **“Massoud”**, Allah have mercy on them,*

To my beloved parents,

To my brother “Mohammed”,

To my sisters “Sarah and her son Wassime, Hadjer, and Yassmine”,

To my extended family,

To my best friends,

To all my teachers

To whom I shared a lot throughout my life.

Table of contents

Table of Contents

Chapter 2: Three-Level T-type Inverter Based M-SVPWM for Power Quality Improvement 40

Chapter 3: Control Strategy of Multi-functional Inverter based PI-like Fuzzy Logic Control 71

List of figures

List of tables

List of symbols and abbreviations

List of symbols

$\alpha_{T_{Isc}}, \alpha_{T_{Voc}}$	Temperature coefficient of short-circuit current and open circuit voltage, respectively
I_{PV}	PV cell output current
I_D	Diode current
I_{sh}	Current leak in parallel resistor
I_{ph}	Photo-current
I_s	Reverse saturation or leakage current of the diode
$I_{SC_{ref}}$	PV's short-circuit current at STC
$I_{ph,ref}$	Reference short circuit current
G, G_{ref}	Irradiance and reference irradiance at STC, respectively
K	Boltzman constant $(1.38 * 10^{-23}\ J/K)$
N_{par}	Number of PV strings
N_{ser}	Number of PV modules per string
N_S	Number of PV cells
$V_{OC_{ref}}$	PV's open circuit voltage at STC
V_{PV}	PV cell output voltage
V_{Th}	Thermal voltage of the cell
q	Charge of an electron $(1.6 * 10^{-19}\ C)$
a	Diode ideality factor
$T_c, T_{c,ref}$	Cell operation temperature and cell temperature at STC

h	Harmonic order
V_h	RMS value of the harmonic voltage of order h
I_h	RMS value of the harmonic current of order h
v_h	Instantaneous voltage of the order h harmonic
i_h	Instantaneous current of the order h harmonic
i_h^*	Conjugate of i_h
V_1, I_1	Fundamental RMS values of voltage and current, respectively
V_h^+, V_h^-	RMS values of the direct and reverse sequence components of the harmonic voltage of order h
I_h^+, I_h^-	RMS values of the direct and reverse sequence components of the harmonic current of order h
θ_h	Phase shift of the harmonic voltage of order h
δ_h	Phase shift of the harmonic current of order h
$\emptyset_h$	Phase shift between voltage and current of the harmonic of order h
THD	Total harmonic distortion
IHD	Individual harmonic distortion
THD_v	Voltage total harmonic distortion
THD_i	Current total harmonic distortion
PF	Power factor
P	Active power
Q	Reactive power
S	Apparent power
D	distortion power
pu	Per unit
p, q, and p_0	Instantaneous real, imaginary and zero sequence power

$\bar{p}, \bar{q}$, and $\bar{p}_0$	Average values of instantaneous real, imaginary and zero sequence power
$\tilde{p}, \tilde{q}$, and $\tilde{p}_0$	Oscillating values of instantaneous real, imaginary and zero sequence power
m_a	Modulation index
f_s	Switching frequency
T_s	Switching period
n	Switching interval
T	Time period
t	Time
ωt	Angular frequency
V_{DC}	DC bus voltage
V_{ao}, V_{bo}, V_{co}	Phase to neutral voltages of phases a, b, and c
V_a, V_b, V_c	Phase voltages of phases a, b, and c
V_a^*, V_b^*, V_c^*	Reference of Phase voltages of phases a, b, and c
V_m	Pick value of the voltage
$\overrightarrow{V_{ref}}$	Reference voltage vector
e_a, e_b, e_c	Grid voltages
S_a, S_b, S_c	Switching states of Inverter's legs a, b, and c
v_a, v_b, v_c	Instantaneous phase voltage at PCC
i_{Fa}, i_{Fb}, i_{Fc}	Instantaneous inverter output current
i_{La}, i_{Lb}, i_{Lc}	Instantaneous non-linear load current
i_a, i_b, i_c	Instantaneous grid current
V_{DC}^*	Reference DC voltage corresponds to MPP
v_α, v_β	Projection of PCC voltage in αβ axis
i_α, i_α	Projection of grid current in αβ axis
${I_{MP}}^*$	Reference DC current corresponds to MPP
i_{Fd}, i_{Fq}	Projection of the output inverter current in *dq* axis
${i_{Fd}}^*, {i_{Fq}}^*$	Inverter reference current in *dq* axis
${i_{C\alpha}}^*, {i_{C\beta}}^*$	Compensating reference currents in αβ axis
${i_{Cd}}^*, {i_{Cq}}^*$	Compensating reference currents in *dq* axis
${v_{Fd}}^*, {v_{Fq}}^*$	Modulation reference voltage in *dq* axis
p_L, q_L	Instantaneous active and reactive power of the non-linear load
$\bar{p}_L$, $\bar{q}_L$	Average parts of the load's active and reactive power
$\tilde{p}_L, \tilde{q}_L$	Oscillating parts of the load's active and reactive power
$\hat{\theta}$	Grid voltage phase angle
ω_{ff}	Feedforward frequency
ω_n	Natural frequency
ζ	Damping ration
e	Error
e_k	Error at sample *k*
Δe_k	Change-of-error at sample *k*
e_{VDC}	Error between V_{PV} and V_{DC}^*
e_d	*d* component current error
e_q	*q* component current error
$\mu(x)$	Membership function of element x
u^*	Centre of gravity
u	Control output (PI or PI-FLC)
u_k	Control output at sample *k*
Δu_k	Change-of-control output at sample *k*

F_n	Non-linear function of FLC
$G_e, G_{\Delta e}, G_u$	FLC scaling factors
K_p, K_i	PI gain parameters
T_r, T_s, and $P.O$	Rise time, settling time, and percentage overshoot
C_1, C_2	DC-link capacitors
C_{eq}	Equivalent DC capacitor value
L_f	Interfacing inductance filter
f_g	Grid frequency
Z_{line}	Grid impedance
R_{L1}, R_{L2}, L_L	Passive elements of the non-linear load

List of abbreviations

APF	Active Power Filter
EMI	Electromagnetic interference
FFT	Fast Fourier Transform
IncCond	Incremental Conductance
LPF	Low Pass Filter
MPPT	Maximum Power Point Tracking
M-SVPWM	Modified Space Vector Modulation
PCC	Point of Common Coupling
PI	Proportional-Integral controller
PI-FLC	PI-like Fuzzy Logic Control
PIL	Processor-in-the-Loop
PLL	Phase-locked loop
PV	Photovoltaic
RMS	Root Mean Square
SPWM	Sinusoidal Pulse Width Modulation
STC	Standard Test Condition
SVPWM	Space Vector Pulse Width Modulation
THD%	Total Harmonic Distortion in percentage
VSC	Voltage Source Converter

General Introduction

The consumption of electrical power has been increased significantly nowadays due to the rapid growth of the population and industrial sectors. The total global energy consumption increased by 2.9% in 2018, reaching $26{,}700\,TWh$ $(1TWh = 10^{12}\ Watts.hour)$, where the fossil fuels contributed to almost 75% of the global electricity requirements, leading in this way the increase of greenhouse gas emission (CO_2) [1]. Henceforth, many countries have implemented green energy economies with specific objectives and supportive policies to increase their renewable energy (RE) generation and reduce fossil fuel consumption [2]. In 2011, Algerian Government adopted ambitious plans to develop RE sources over the period of 2011-2030, whose objective is to install $22\ GW$ of RE in two phases by 2030 [3], some have already started with objective to reach 40% of electricity demand by 2030 from solar, hydro and wind [4]. Due to the strategic geographical location of the country, solar energy gaining the highest potential among all other exciting RE sources.

The use of solar photovoltaic (PV) systems is considered promising among the various existing of solar energy technologies with penetration of 10.3% from the total global generation. This PV system can operate either in standalone mode with the storage system or in grid-connected mode [5]. The grid-connected PV system has the advantage being needless of any storage element that has many economical and technical limitations; therefore, it becomes more and more emerging [6]. In turn, this high penetration of the non-conventional power-electronics-based RE sources starts to affect the stability, security, and the quality of the power system bringing new challenges to the distributed generation (DG).

The nature of PV sources necessitates the use of power electronic converters in order to extract, convert, and adapt the energy delivered from the PV panels and inject it into the utility grid. However, these converters are well-known as harmonic pollution sources that can affect the power quality (PQ) as well as the operating system itself. Moreover, harmonics can come from the grid, because of the proliferation of nonlinear loads in industrial and domestic applications that can also affect the renewable energy conversion systems. Therefore, it is essential to ensure perfect compliance of the grid-interactive PV system with the international standards (*IEC-61000*, *IEEE-519*) [7].

The conventional solutions against harmonics pollution are used to be passive and/or active filtering [8][9]. The latter one is however the preferred solution for several reasons such as the possibility to eliminate as much as possible undesired harmonics from the non-linear loads. Although, the active power filter (APF) requires high power converter ratings, consequently high initial cost.

As an alternative solution, the active filtering functionality can be possibly integrated into any kind of grid-interactive converter system (e.g. grid-tied PV systems) as the control strategies of power converters are dramatically developed [10]. Recently, several works have been presented in which renewable energy conversion systems are associated with APF to ensure sufficient PQ level with different topologies and various control strategies.

Typically, the grid-connected PV system's topology that associated with APF consists of two-stages in order to perform the interfacing between the PV array and the utility grid. The first stage is a DC/DC converter used to extract the maximum power from the PV array and boost its voltage above the grid peak voltage. The other stage is a DC/AC converter that is dedicated to perform the power conversion and PQ improvement. It is however, the first stage can be eliminated by ensuring a high input DC voltage; to do so, PV modules are connected in series to achieve the required grid voltage. Consequently, the single-stage topology has a smaller system size, lower cost, and better efficiency; in comparison, the single-stage is $4-10\%$ more efficient than the two-stage topology [11][12].

Furthermore, using a multilevel inverter as an interfacing element between the PV array and the grid Point of Common Coupling (PCC) can further improve the PQ [13]. Compared to the traditional two-level inverter, the multilevel inverter generates AC voltages and currents with a better harmonic spectrum, hence, reducing the electromagnetic compatibility problems [14].

All in all, with the advent of power electronic converters and robust control techniques, renewable energy systems can possibly get massively interconnected with the grid for power feeding. Therefore, the use of more efficient control strategies would not only enhance the performance of these systems, but also improve the PQ in generation, distribution, and utilization of DGs.

The presentation of this thesis is spread over four main chapters:

After general introduction, the first chapter will be devoted firstly to photovoltaic systems, with a macroscopic view of the different configurations and topologies. In addition, the various MPPT methods are also discussed at the end of the first part. The second part will deal with the problems of power quality, specifically to the harmonics pollution, their causes and consequences as well as the standards aimed at reducing their proliferation. We also recall the existing decontamination solutions, both traditional and modern.

The second chapter emphasizes the heart of the system which is the Three-level T-type inverter. Based on the topological structure of the proposed three-level inverter, the switching control principle of the Modified Space Vector Pulse Width Modulation (M-SVPWM) is analyzed in detail. A comparative analysis is performed with the conventional two-level inverter especially in terms of power quality. In the end, the proposed Three-level T-type inverter-based M-SVPWM is validated experimentally using a cost-effective STM32F4 Discovery board.

Chapter three will deal with the overall control strategy for the proposed system to perform the multi-functional objectives. Firstly, a literature review about different control strategies of a multi-functional inverter is highlighted in this chapter. After that, each part of the control system for each specific function will be discussed and analyzed in detail, where the objective of the proposed control system is to harvest the maximum solar PV power and inject it into the grid utility and/or to the nonlinear load, and simultaneously reducing the current harmonics and compensating the reactive power. Lastly, a particular focus will be given to the main contribution of our control part, which is the proposed PI-like fuzzy logic control (PI-FLC), where a new approach of setting the scaling factors which considerably affect the system’s response is proposed. Furthermore, a methodology to properly set the fuzzy rules is suggested.

The fourth and the last chapter is dedicated to evaluate and validate the proposed system through processor-in-the-loop (PIL) test, where the Simulink model is configured to perform the PIL using a cost-effective STM32F4 discovery board, where the control part of the system is replaced with the created PIL block and lunched into the STM32F4 board using the target’s compiler and embedded coder tool. This block enables data exchange between the hosting computer and board through the communication serial link. The obtained results of the proposed system have been presented in detail under steady-state and dynamic conditions. Furthermore, a comparative study has been established over the conventional PI controller and other proposed controllers in order to show the superiority of the proposed PI-FLC controller.

Finally, a general conclusion summarizes the work carried out in this thesis, followed by some perspectives and future research work.

Chapter 1: Photovoltaic System and Harmonic Depollution

1.1 Introduction

In the last decades, the significant increase in the global energy demand in addition to the greenhouse gas emission has necessitated the change in the energy pattern with integrating more climate-friendly energy resources such as hydro, wind, or solar. Among the different types of these energies, and due to the easy implementation, low maintenance and continuously declining prices its cost, solar PV has been considered a suitable replacement for the conventional energy sources. At the same time, the power quality has become the most important issue in the power sector. In recent years, the proliferation of non-linear loads in the power system has increased at an unprecedented rate in addition to the large penetration of renewable energy sources in the power system. As result, drawing a significant amount of harmonic currents from the source, reducing efficiency and power factor.

We will begin this chapter with a brief presentation of the potential of solar energy in Algeria, then an overview of different configurations and topologies of the PV model and PV systems are described, and various existing MPPT control techniques in the literature are discussed in a comprehensive manner. The second part is dedicated to the power quality issue, presenting the main disturbances affecting the quality of the electric signals, in particular the harmonics for which we will be focused on. In addition, it talks about their origins, their effects and the standards in force. Then, it discusses the various solutions considered to overcome the problems of harmonic disturbances, in particular active filtering. At the end, stat of the arte of the PV system associated with active power filtering is tabulated.

1.2 Solar energy potential in Algeria

Algeria country has wide promising renewable energy sources due to its geographical location, such as hydropower, wind, geothermal, biomass, and solar [15][16]. However, being located in the Sunbelt, solar energy gaining the highest potential among of them all. In this context, Algeria receives direct irradiation estimated at $169{,}440\ kW/m^2/year$ with a potential production of $3000\ kWh/year$ [17][18]. Table 1-1 shows the potential for solar energy in Algeria. The country's desert is considered to be one of the areas with high average solar radiation and high global temperature. The insolation duration is around 2000 to 3900 h annually, with horizontal surface radiation from 3 to 5 kWh/m^2. Figure 1-1 (a) and (b) show respectively the irradiation and temperature distribution in the country [19].

Table 1-1 *Solar energy potential in Algeria [20].*

	Location		
	Coastal Area	**Inner Area**	**Desert Area**
Surface (%)	4	10	86
Average of the sunrise (hour/year)	2650	3000	3500
Average energy received (kWh/m²/year)	1700	1900	2650

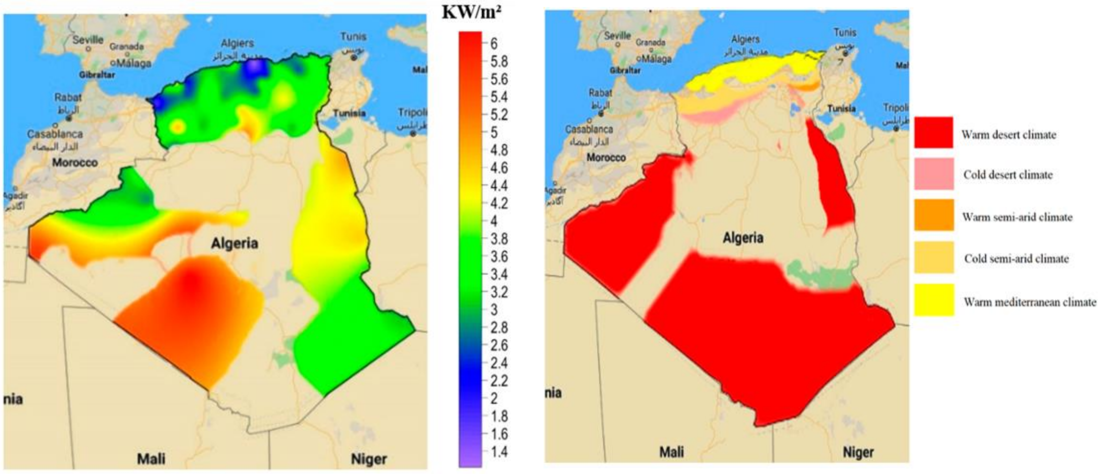

(a) (b)

Figure 1-1 *(a) Solar irradiation in Algeria kW/m² (b) Temperature distribution in Algeria.*

1.2.1 Photovoltaic generation in Algeria

Photovoltaic (PV) system is considered one of the promising solar energy technologies. Figure 1-2 illustrates the potential of the PV generation in the Algerian desert area that covers 2048.297 km^2 of land [21]. This area has the potential to generate $168 * 10^{12}$ $kWh/year$ if we consider the utilization of 50% of the available space factor and an efficiency of 10%.

The master plan for renewable energies in Algeria emphasizes the development of solar energy, with 13.5 GW of PV generation capacity planned for 2030. The renewable energy installed in Algeria based on different technologies (PV, Hydro, Wind, Concentrated solar thermal power (CSP)) are shown in Figure 1-3. Most of the installed Photovoltaic farms in the country aimed to provide electricity to rural places having difficulty in extending the grid utility.

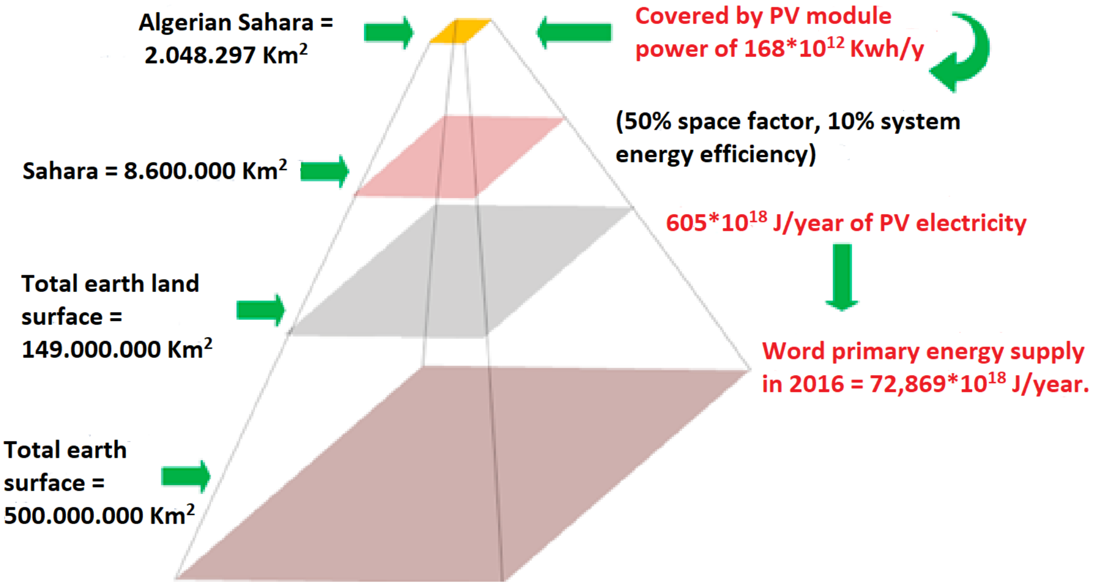

Figure 1-2 *Potential PV generation for the Algerian Sahara Desert.*

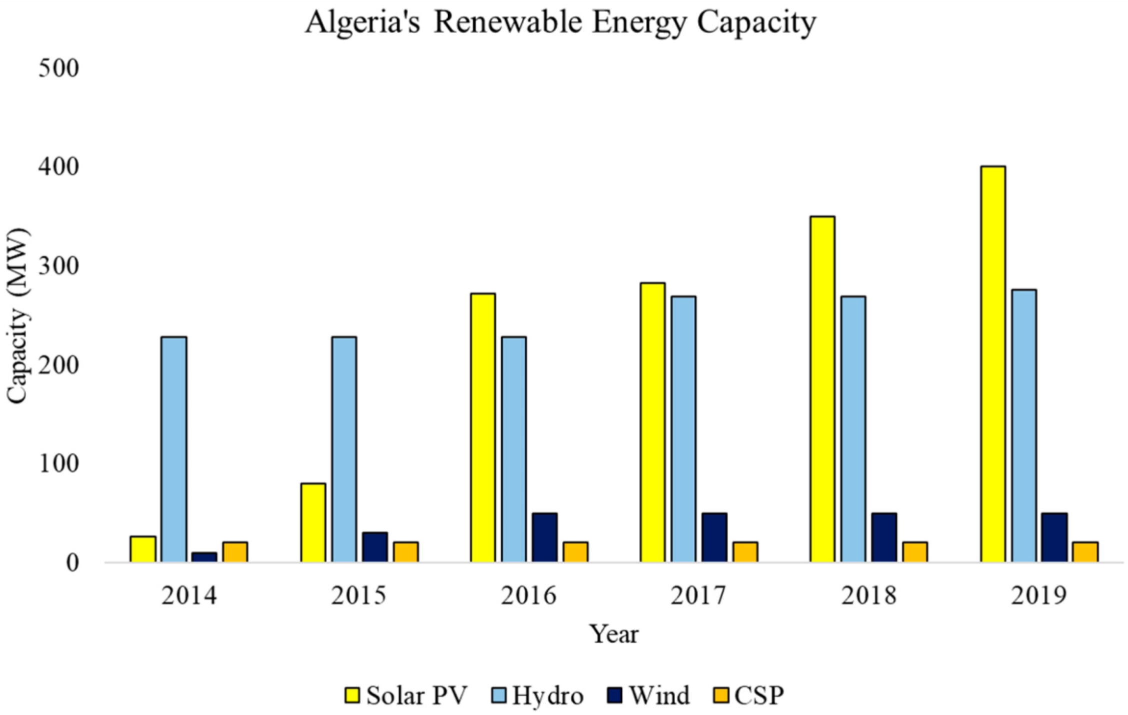

Figure 1-3 *Reneable energy installed capacity in Algeria from 2014 to 2019 [1].*

Figure 1-4 demonstrate the locations of all PV stations in Algeria, and listed in Table 1-2 correspondingly.

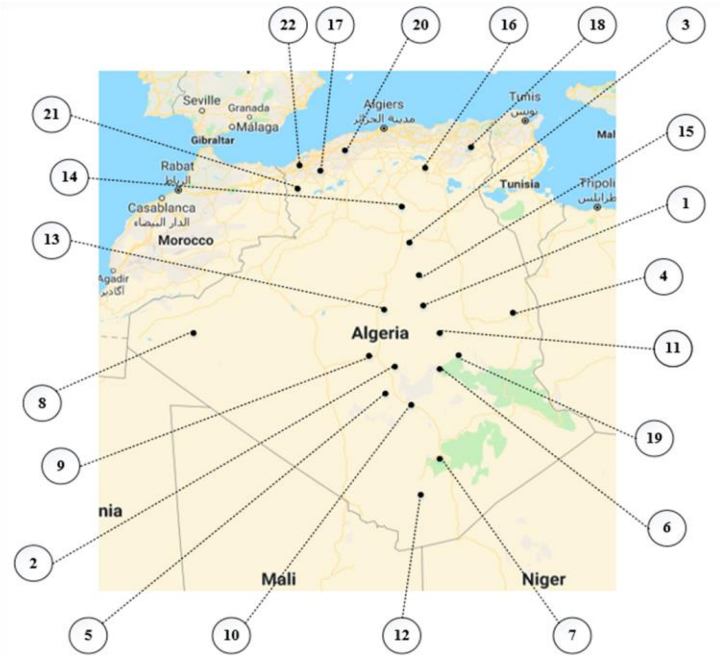

Figure 1-4 Locations of PV stations in Algeria.

Table 1-2 *Installed solar PV generation stations [15].*

Station		Location	Capacity (MW)
1	**SPP1**	Hassi R'mel	25
2	**SPE**	Adrar	10
3	**Ghardaïa**	Ghardaïa	11
4	**Djanet**	Illizi	3
5	**Adrar**	Adrar	20
6	**Kabertene**	Adrar	13
7	**Tamanrasset**	Tamanrasset	13
8	**Tindouf**	Tindouf	9
9	**Z.Kounta**	Adrar	6
10	**Timimoun**	Adrar	9
11	**Reggane**	Adrar	5
12	**In-salah**	Tamanrasset	5
13	**Aoulef**	Adrar	5
14	**Ain EL-Lbel**	Djelfa	20
15	**Khang**	Lghouat	20
16	**Oued EL-Kebrit**	Souk Ahras	15
17	**Sedrate Leghzal**	Naama	20
18	**Ain EL-Melh**	M'sila	20
19	**EL-Hadjira**	Touggourt	10
20	**Ain Shouna**	Saida	30
21	**E.B.S Chikh**	El Bayadh	24
22	**Telga**	Telemcene	12

The first solar power plant in Algeria was installed in 2011, and there were 22 plants available for a total capacity of 423 MW at the end of 2019, which is seven times less than the target of 3000 MW by 2021 [22]. According to the initial target, a total of 60 PV photovoltaic power plant projects were planned for the period 2011 to 2020.

1.3 Power quality in Algeria

The Algerian electrical network as illustrated in Figure 1-5 consists of 15 synchronous machine generators, 114 buses, 16 winding transformers, 175 transmission lines, and 99 load buses. The total real and reactive power demands are 3146.2 MW and 1799.4 $MVAR$ [23][24].

Internationally, the Algerian electrical network connected with the neighbouring country Tunisian and Morocco through two very high voltage transmission lines of 400 kV. The electrical connection with Tunisia by the means of two 90 kV lines, one 220 kV line, one 150 kV line and one 400 kV line; while the electrical connection between Algeria and Morocco is established through two 220 kV lines and one 400 kV line [25].

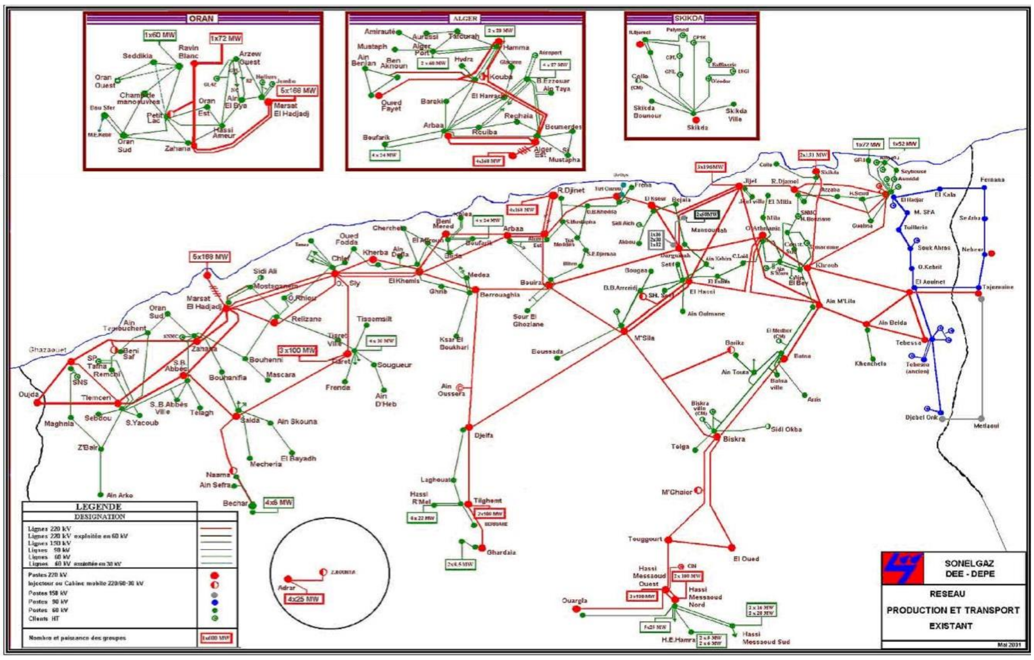

***Figure 1-5** Algerian Electrical power transmission network [24].*

Incorporating large amounts of PV systems into the Algerian grid is expected to grow more and more in the upcoming decade. However, this large penetration of PV systems could have serious consequences on important technical aspects such as voltage and frequency deviations affecting by this way the power quality, power control and utility protection schemes, etc. in addition to the widespread use of non-linear electronic equipment in the industrial sectors. Therefore, it is necessary to upgrade the Algerian power gird in order to cope with this kind of penetration, by adding the protection devices, adapting the power capacity of the transmission and distribution lines, use advent of power electronic converters with robust, efficient, and adaptive control techniques for grid-connected applications, etc. [25][26] [27].

Despite that, many harmonic sources connected to the load buses are known as non-linear load due to the significant increase in the industry sectors that rely on non-linear electronic equipment such as power converters, motors, etc. We take for example the harmonic analysis of four non-linear loads connected at buses 12, 32, 33, and 66; each of them has nine harmonic components as indicated in Table 1-3 [23].

Due to the increase in energy demand each year, SONALGAZ Company planned to implement 34,441 km of transmission lines from 2017 to 2027. Currently, 9930 km transmission lines are under development, with another 24,511 km planned, which includes national and international interconnections and adapted with the recent gird codes and international standards [19].

***Table 1-3** Harmonic spectrum data at some non-linear (NLD) buses.*

Harmonic order	NLD 1 at Bus 12		NLD 2 at Bus 32		NLD 3 at Bus 33		NLD 4 at Bus 66	
	Mag (%)	Ph (°)	Mag (%)	Ph (°)	Mag (%)	Ph (°)	Mag (%)	Ph (°)
1	100	0	100	0	100	0	100	0
5	18.24	-55.68	4.24	-95.68	20	0	23.52	111
7	11.9	-84.11	17.9	-74.11	14.3	0	6.08	109
11	5.73	-143.56	8.3	-113.56	9.1	0	4.57	-158
13	4.01	-175.5	7.01	-194.58	7.7	0	4.2	-178
17	1.93	111.39	1.93	11.39	5.9	0	1.8	-94
19	1.39	68.3	2.39	38.3	5.3	0	1.37	-92
23	0.94	-24.61	0.64	-4.61	4.3	0	0.75	-70
25	0.86	-67.64	0.46	-17.64	4	0	0.56	-70
THD (%)	**23.0**	/	**21.6**	/	**29.1**	/	**25.2**	/

1.4 Photovoltaic operation and modelling

1.4.1 Structure of the PV solar cell

Solar cells are the fundamental components of photovoltaic panels, made from semiconductor materials, mostly silicon, besides other materials. They have the ability to convert electromagnetic radiation into electrical current. Basically, the solar cell is a specially designed $P - N$ junction, made from two different layers of doped silicon. Doping is the process of adding impurity atoms to the semiconductor crystalline. In the case of the n-layer, atoms with one more valence electron, called *donors*, and in the case of the p-layer, atoms with one less valence electron, known as *acceptors*. When the two layers are joined together, an electric field is formed between them, caused by the diffusion of free electrons from n-layer to p-side, and the diffusion of free holes from p-layer to n-side. The diffusion stops, as soon as, the equilibrium is reached and the potential barrier is built. A schematic diagram of the $P - N$ junction at equilibrium state is demonstrated in Figure 1-6**.**

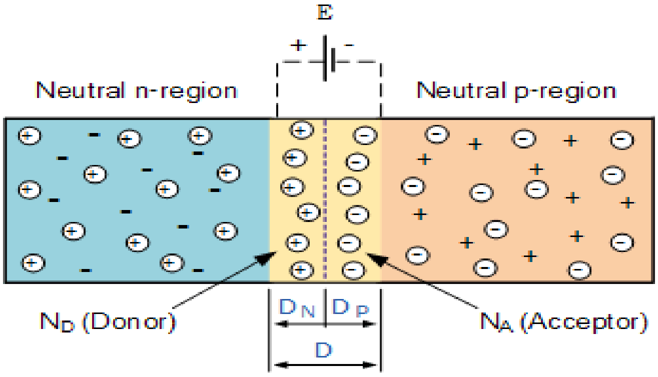

Figure 1-6 *P-N Junction and Potential Barrier Formation.*

To allow the flow of electrons out of this structure, a front and back metallic contacts are installed to the layers, anti-reflective coating is then used as a cover to reduce reflection coefficient of silicon layers. Finally, a piece of glass is applied in the front to protect the solar cell from dust and damage. It is necessary to mention that the layer facing sun light should contain strips for contact purpose in order to allow the radiation to reach the solar cell, called fingers. Figure 1-7 shows the general structure of the solar cell [28].

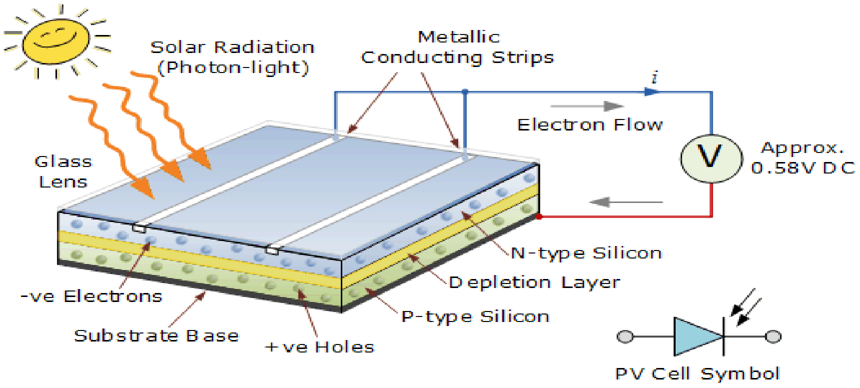

Figure 1-7 *General structure of the photovoltaic cell.*

1.4.2 PV operation principle

Photons of solar radiations strike the cell; some of them are reflected by the top surface and metal fingers. Those which are not reflected penetrate in the substrate, the ones with less energy pass through the cell without causing any effect. Only those with energy level above the band gap of silicon are able to energize electrons and make them free. This fact creates electron-hole pairs where free electrons migrate to the N-region, as well as, holes to the P-region. Due to the effect of the electric field in the $P-N$ junction, electron-hole pairs cannot recombine unless an external path between P and N regions is provided. The motion of electrons through the external path produces electrical current as shown in Figure 1-8. This is known as the light-generated current which is directly proportional to irradiance.

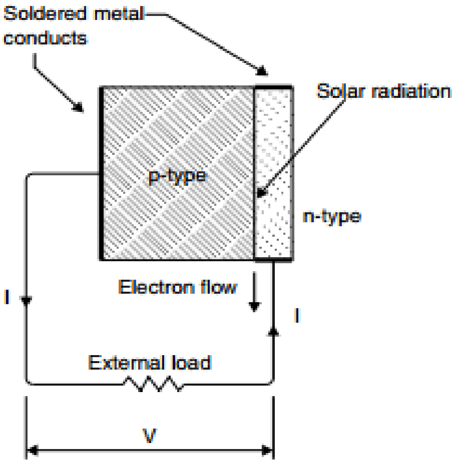

Figure 1-8 *Photovoltaic effect of a PV cell.*

1.4.3 PV generator

Since an individual PV cell produces only about $0.5\ V$, and real life applications requires too much higher voltages, PV cells are pre-wired in series and enclosed in weather-resistant package, known as "*PV Module*". Typical modules comprise 36, 54 or 72 of cells wired in series. An important element in PV system design is deciding how many modules should be connected in series and how many in parallel to deliver whatever energy is needed. Such combinations of modules are referred as a "*PV array*", the complete power generating unit which can be interconnected to produce more power shown in Figure 1-9.

Multiple modules, in turn, can be wired in series to increase voltage and in parallel to increase current as illustrated in Figure 1-10, the product of which is power [29].

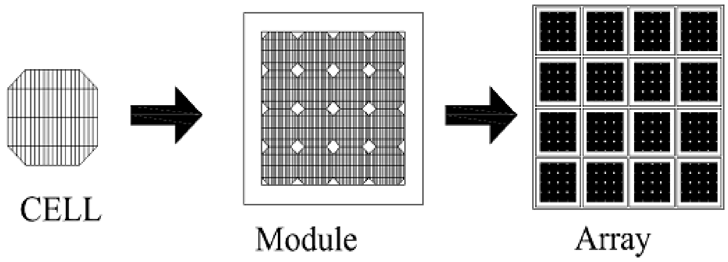

Figure 1-9 *Photovoltaice cells, module, and Array.*

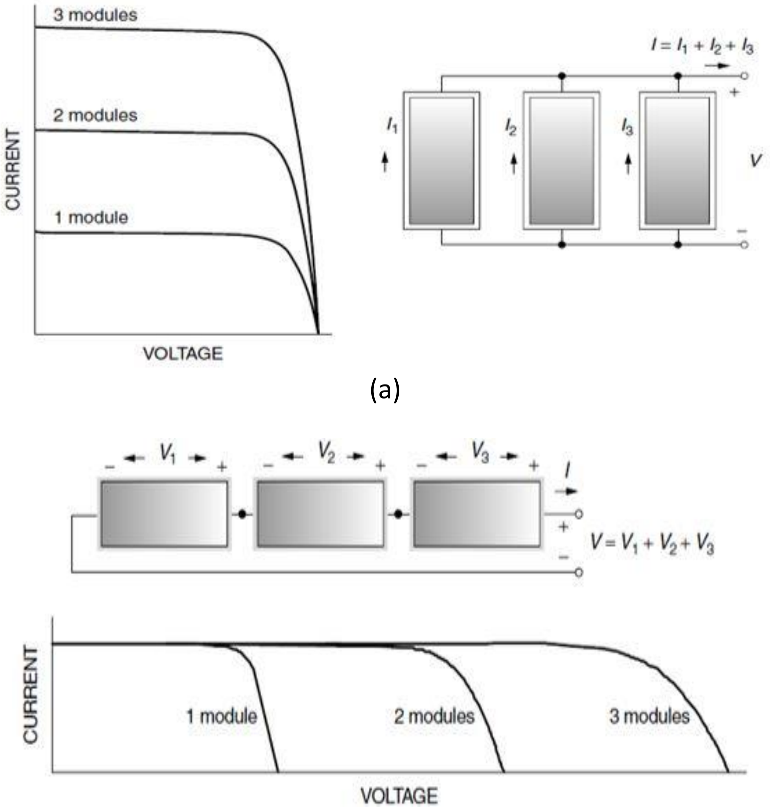

(a)

(b)

Figure 1-10 *Parallel and series connection of two identical solar modules (a) Parallel connection. (b) Series connection.*

1.4.4 PV modelling

Modelling is a basic tool of the real system simulation. For modeling, it is necessary to analyze the influence of different factors on the photovoltaic cells and to take in consideration the characteristics given by the producers. The mathematical models for photovoltaic cells are based on the theoretical equations that describe the operation of the photovoltaic cells and can be developed using the equivalent circuit of the photovoltaic cells [30]. There are many models of PV cell, some of them are illustrated in the following Figure 1-11.

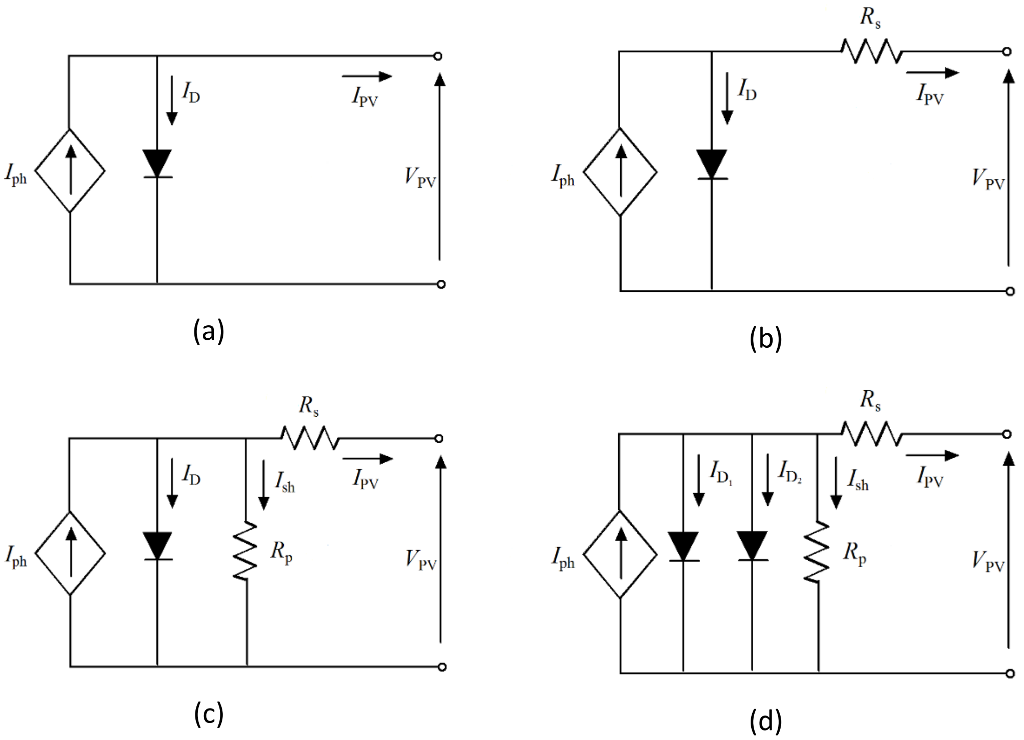

(a) (b)

(c) (d)

Figure 1-11 *(a) Ideal single diode. (b) Single diode with $\boldsymbol{R_s}$ (c) Single diode with $\boldsymbol{R_s}$ and $\boldsymbol{R_{sh}}$ (d) Double diode with $\boldsymbol{R_s}$and $\boldsymbol{R_{sh}}$model equivalent circuits.*

The most common model used to predict the energy production in photovoltaic cells is the single diode lumped circuit model, which is derived from its physical principle the one that referred to Figure 1-11 (c). In this model, the PV cell is usually represented by an equivalent circuit composed of a light-generated current source, a single diode representing the nonlinear impedance of the $P-N$ junction with series/parallel intrinsic resistances (R_p and R_s) accounting for resistive losses [31].

The cell output current can be obtained simply by applying Kirchhoff's law as follows:

$$I_{PV} = I_{ph} - I_D - I_{sh} \tag{1-1}$$

Where: I_{PV} is the photovoltaic output current, I_{ph} is the photocurrent, I_D is the diode current, and I_{sh} is the current leak in parallel resistor.

The $I-V$ characteristics of the PV cell are then described by:

$$I_{PV} = I_{ph} - I_s\left(\exp\left[\frac{V_{PV}+\mathrm{I}_{PV}\mathrm{R_S}}{a.V_{th}}\right] - 1\right) - \frac{V_{PV}+I_{PV}\mathrm{R_S}}{\mathrm{R}_p} \tag{1-2}$$

The photocurrent I_{ph} is a function of irradiance and temperature as given by (1-3)

$$I_{ph} = \frac{\mathrm{G}}{\mathrm{G}_{ref}}\left(I_{ph\_ref} + \alpha_{T\_Isc}.\left(T_c - T_{c,ref}\right)\right) \tag{1-3}$$

While the diode saturation current is given by:

$$I_S = \frac{I_{SC_{ref}} + \alpha_{T_{Isc}} \cdot \left(T_c - T_{c,ref}\right)}{exp\left[\frac{V_{OC_{ref}} + \alpha_{T_{Voc}} \cdot \left(T_c - T_{c,ref}\right)}{a.V_{Th}}\right] - 1} \tag{1-4}$$

Where V_{Th} is the thermal voltage and depends on the PV cell temperature too,

$$V_{Th} = \frac{N_S.K}{q}.T_c \tag{1-5}$$

Simulation of a PV cell/module requires numerical values for I_s, I_{ph}, a, R_s, and R_p. PV manufacturers do not provide these parameters. Different techniques are available which can be replayed to identify these parameters. These techniques can be classified within two groups:

- *Group 1*: Techniques based only on the module identification datasheet parameters.
- *Group 2*: Techniques based on the measured of the parameter extraction of (I, V) data.

The latter one is however better in term of accuracy, but requires test data. In our work, the data of the module are already available in Matlab/Simulink.

The PV source in general is composed of N_{par} parallel strings while each string contains N_{ser} series PV modules. As have been explained, large PV arrays aim to increase output DC voltage and meet the required power demand. The mathematical model of large PV array is similar to that of a PV module with higher photocurrent, and higher diode current. Besides, series and parallel resistances corresponding to Figure 1-11 (c) are modified to Figure 1-12.

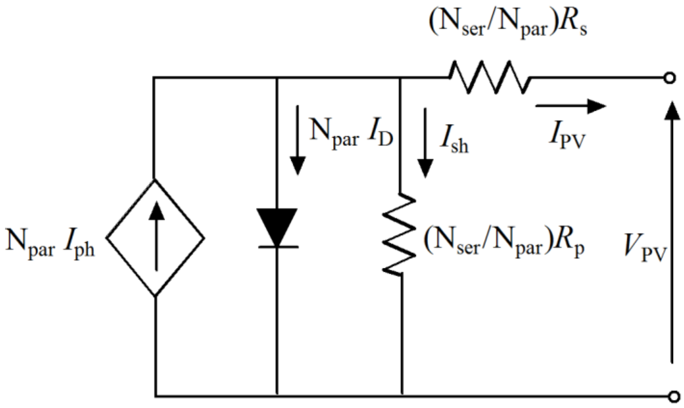

***Figure 1-12** The electrical modeling of the PV array.*

Consequently, the current-voltage relationship of PV module is upgraded as to account for the number of series and parallel PV modules by equation (1-6).

$$I_{PV} = N_{par} I_{ph} - N_{par} I_s \left(\exp\left[\frac{V_{PV} + \mathrm{I}_{PV} \frac{\mathrm{N_{ser}}}{\mathrm{N_{par}}} \mathrm{R_S}}{a.V_{th}.\mathrm{N_{ser}}} \right] - 1 \right) - \frac{V_{PV} + I_{PV} \frac{\mathrm{N_{ser}}}{\mathrm{N_{par}}} \mathrm{R_S}}{\frac{\mathrm{N_{ser}}}{\mathrm{N_{par}}} \mathrm{R}_p} \qquad (1\text{-}6)$$

The PV source delivers a voltage and current to the DC link that are a function of the environment conditions, irradiance and temperature. Subsequently, the PV source's power is variable and maximum extraction can be achieved by varying the voltage across it.

1.5 Photovoltaic systems

Photovoltaic power systems are classified according to their functional and operational requirements, their component configurations, and how the equipment is connected to other power sources and electrical loads. In general, PV systems are classified into two groups: Stand-alone (off-grid) PV systems and grid-connected (on-grid) PV systems:

1.5.1 Stand-alone PV systems

Autonomous systems are generally implemented in rural and remote areas. They are usually supported by storage systems (e.g. batteries) to meet the load when the solar irradiation is not sufficient for the PV to cover all the need. This type is particularly suitable for remote areas that are not easily accessible or have no access to an electric grid. A typical stand-alone system consists of a PV generator, a battery bank for storage and a set of static DC-DC and DC-AC converters. A schematic diagram of a stand-alone system is shown in Figure 1-13. As it can satisfy both DC and AC loads simultaneously.

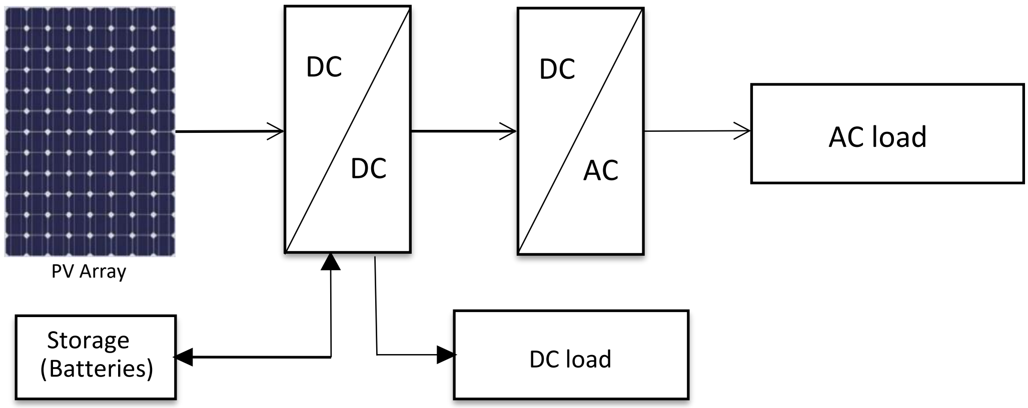

Figure 1-13 *Stand-alone PV system schematic.*

1.5.2 Grid-connected PV Systems

The primary component in grid-connected PV systems is the inverter, or power conditioning unit (PCU). The PCU converts the DC power produced by the PV array into AC power consistent with the voltage and power quality requirements of the utility grid. These systems can be connected directly to the distribution network and/or to the home network (Smart home). At night or during other periods when the electrical loads are greater than the PV system output, the balance of power required by the loads is received from the electric utility. Figure 1-14 presents a diagram of grid-connected PV system.

The grid-connected system has the advantage being needless of any storage element that has many economical and technical limitations. The main issues related to the grid-connected systems are maximum power extraction, power quality, overall efficiency, initial investment costs, etc.

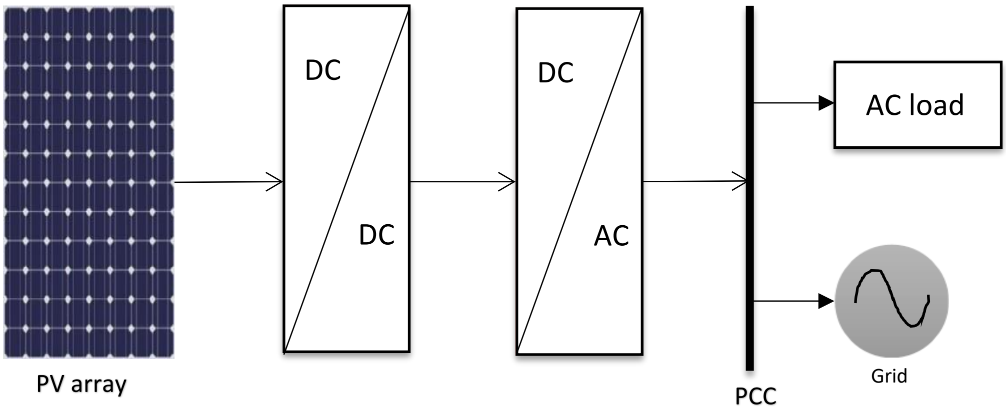

Figure 1-14 *Grid-connected PV system schimatic.*

Typically, the grid-connected PV system's topology consists of two-stages in order to perform the interfacing between the PV array and the utility grid (Figure 1-15 (b)). The first stage is a DC/DC converter used to extract the maximum power from the PV array and boost its voltage above the grid peak voltage. The other stage is a DC/AC converter that is dedicated to perform the power conversion. The first stage can be eliminated by ensuring a high input DC voltage, and for this, PV modules are connected in series to achieve the required grid voltage. The single-stage topology (Figure 1-15 (a)) has a smaller system size, lower cost, and better efficiency; in comparison, the single-stage is $4 - 10\%$ more efficient than the two-stage topology [11][12].

The efficiency being an important criterion in our application, the first topology single-stage grid connected PV system will be adapted in our work.

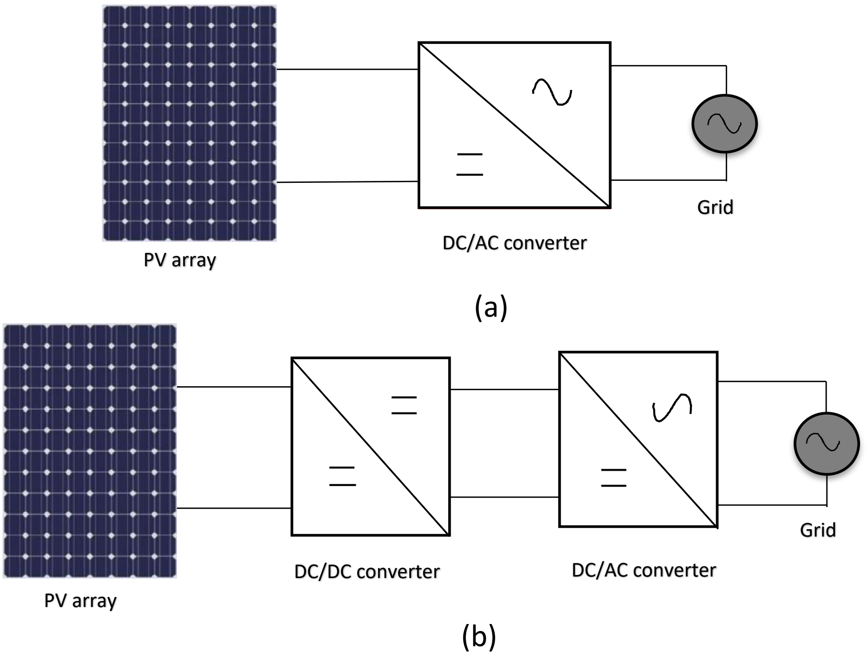

Figure 1-15 *(a) Single-stage grid connected PV system (b) double-stage grid connected PV system.*

1.5.3 Maximum Power Point Tracking algorithms (MPPT)

It is well-known that PV performance is affected by external factors, which mainly include temperature and irradiation. These two parameters are dependent on the geographical area of installation and the different year's seasons. As illustrated in Figure 1-16 (a)(b) the I-V and P-V characteristic and how the irradiance can affect directly the short circuit current (I_{sc}), while Figure 1-16 (c)(d) shows how can the temperature effects directly the open-circuit voltage (V_{oc}).

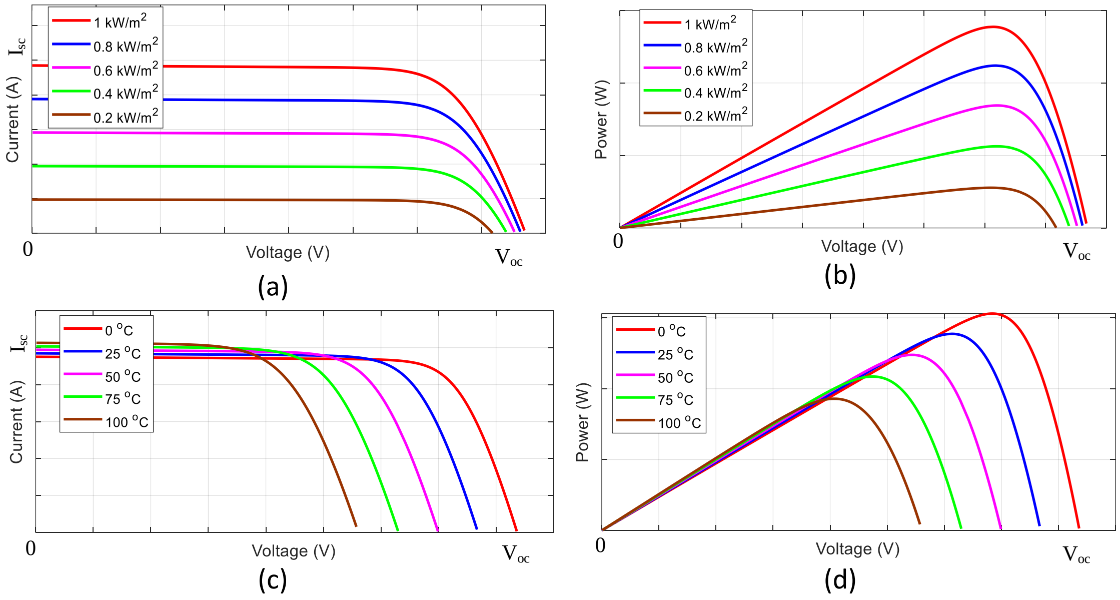

Figure 1-16 *(a) I-V characteristic, and (b) P-V characteristic, under different irradiance level, (c) I-V characteristic, and (d) P-V characteristic, under different temperature.*

It is noticed that for given any climate condition, there is only a single-point at which power delivered is maximum called the *Knee*. Therefore, it is essential to make the PV generator operates continuously at this point whatever the weather or load conditions. To do so, a process called Maximum Power Point Tracking (*MPPT*) technique is used.

In literature, there are several MPPT techniques using $\frac{dP}{dV} = 0$ to obtain the maximum power point output. The algorithms that most frequently used are the so-called classical extremal methods: The incremental conductance (IncCond) method, Hill climbing (HC), and Perturb and Observe (P&O).

Usually a DC-DC converter is introduced at the output of the PV source to test the viability of the MPPT technique, operating in that way as an impedance adapter. The MPPT regulator determines the converter cycle ratio to extract the power required at the point of maximum power. Figure 1-17 illustrates a diagram of such a conversion chain.

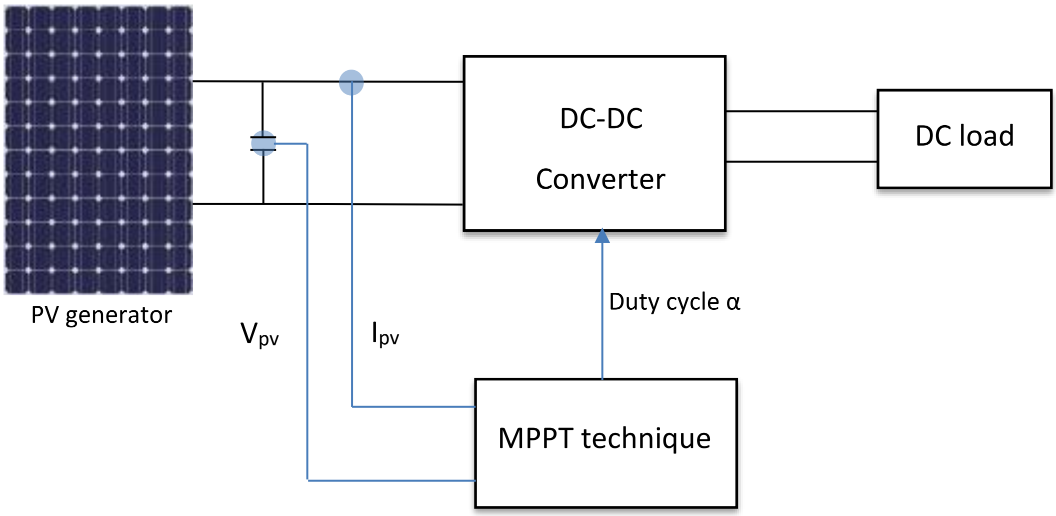

Figure 1-17 *Block diagram of maximum power extraction principle.*

1.5.3.1 Over-view on MPPT techniques

In the literature, several research works have dealt with various techniques of MPPT control. These commands are selected according to their needs (Cost, complexity, precision, speed of convergence). The Perturb and Observe (P&O) [32][33], Incremental Conductance (IncCond) [34][35], and Hill Climbing (HC) [36][37] methods are the most popular because they have the advantage of easy implementation [38]. They are widely used in many applications for: Battery chargers, grid connection...etc. The principle of these methods consists in disturbing the system with a voltage / duty cycle and checking its behaviour. In addition, there are other simpler, so-called indirect methods, such as the short-circuit current [39], open-circuit voltage [40] and ripple correlation control (RCC) methods [41], which are used for low cost applications, such as street lighting. These methods suffer from the remarkable problems under sudden changes in illumination, leading to other intelligent MPPT algorithms being offered as alternatives, in terms of accuracy and speed.

Nowadays, several methods of maximum power point tracking (MPPT) based on artificial intelligence, such as fuzzy logic (FLC) [42], neural networks (ANN) [43], or those inspired by the control theory (by sliding mode,…) [44] are cited. The aforementioned techniques can provide rapid and high performance compared to conventional research methods during random and rapid variations in solar irradiance. In addition, during partial shading, where characteristic I-V presents several knees (Figure 1-18 (b)) (different local points and one global point), other techniques, called global methods, based on genetic algorithms (GA) [45], and its derivatives: with particle swarms optimization (PSO) [46], Ant colonies (ANT) [47], bee colonies (ABC) [48], in which converge towards a global optimal point.

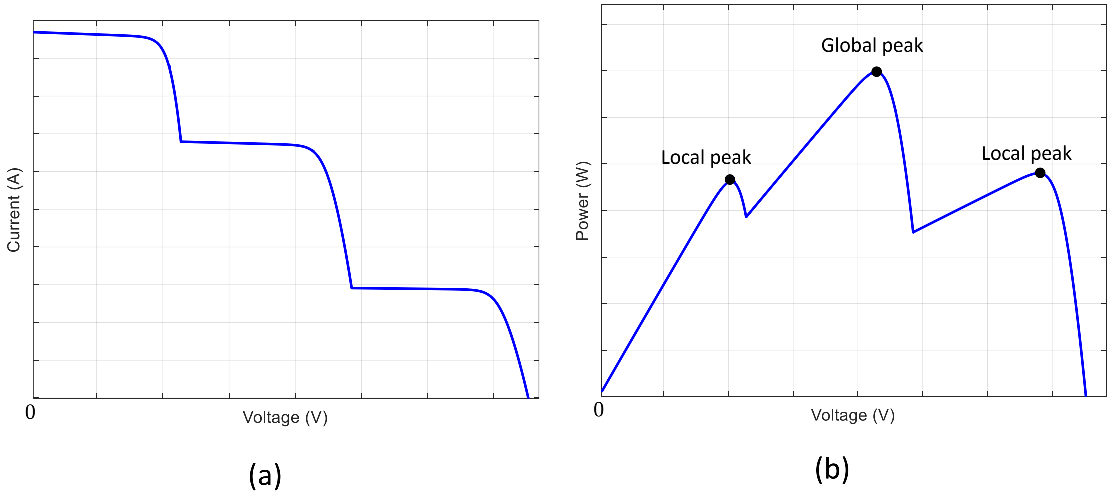

(a) (b)

Figure 1-18 *(a) I-V characteristics and (b) P-V characteristics of photovoltaic string under partial shading phenomena.*

The large number of proposed methods can make it difficult to determine the best technique to adopt when implementing in a photovoltaic system. Methods vary in complexity, number of sensors required, digital or analog implementation, speed of convergence, tracking capability, cost effectiveness…etc.

1.6 Harmonic Distortion

Harmonic distortion is any steady-state deviation from the ideal sinusoidal shape of the voltage or current wave (Figure 1-19).

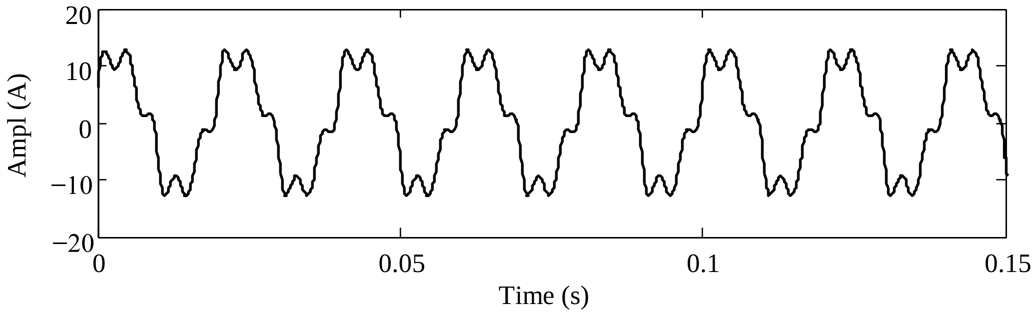

Figure 1-19 *Harmonic distortions.*

1.6.1 Origins of harmonic distortions

Although not the only reason, non-linear loads are the main source of harmonic pollution. A non-linear load is a load whose current is not proportionally variable with the voltage, such as basic power electronics elements (diode, thyristors, ... etc.), non-linear resistors, saturated transformers ... etc.

At the beginning of their appearance, harmonic distortions were rather caused by the saturation of transformers; the magnetizing current absorbed by a transformer operating in the saturation region is non-sinusoidal, and generally contains all odd harmonics, starting with the third. Nevertheless, this magnetization current remains low compared to the current delivered by the transformer under load, which is why the effects of this current (of magnetization) are negligible at full load.

Nowadays, systems based on power electronics are the main cause. These systems are generally power converters (AC-DC, DC-AC, etc.) [49][50][51][52] which use non-controllable (diodes) or controllable (thyristors, transistors) semiconductors. The degree of harmonic pollution generated depends on the type of semiconductor used, which in turn depends on the characteristics of the load. In general, for high power applications, GTO or thyristors are used, while transistors (IGBTs in particular) are used for medium power applications. The latter generally makes it possible to reduce switching harmonics thanks to its high frequency, but thyristors and diodes remain the most polluting semiconductors. These systems based on power electronics fulfil various tasks, and allow a better flexibility and better efficiency of the electro-energy system, which is why nowadays they are found almost everywhere:

- *In energy production*: Excitation and equipment associated with the control of alternators, conversion and integration of renewable energy sources (wind, photovoltaic, etc.) in the distribution network;
- *Energy transmission and distribution*: Direct current transmissions (HVDC), compensation and control of power flows by FACTS elements (STATCOM, SVC, UPFC,… etc.). These systems use high power thyristors which are generally significant sources of harmonics;
- *Power supply for industrial loads*: Virtually all industrial loads are interfaced with power electronics converters; Current converters (AC/DC), frequency converters, variable speed drives, … etc.
- *Power supply for domestic loads:* Today, there are more and more loads for domestic use supplied by power electronics (computer equipment, televisions, etc.). These loads, although their powers are incomparable with those of industrial loads, the harmonic distortions they can be more severe.

1.6.2 Effects of harmonic disturbances

Although the sensibility of different devices is diverse with regard to harmonics, there are essentially two kinds of effects [53].

1.6.2.1 Transient effects

Instant effect the one that appears immediately on the equipments;

- *Electronic and electromechanical systems*: Among the effects, we can cite the disturbance of thyristor switching when the harmonic quantities displace the zero crossing of the voltage, the increase in the margin of error of the measuring devices, or even unwanted tripping of protection relays.
- *Electrodynamic effects*: the presence of harmonics causes vibrations and noises in electromagnetic devices. Parasitic mechanical torques due to harmonic rotating fields, giving rise to vibrations in rotating machines.
- *Telecommunications:* noises in telecommunication networks and damage to the quality of the image (television) and sound.

1.6.2.2 Permanent effects

They appear after exposure to the harmonic disturbance. The most important long-term effect is of a thermal nature, which results in heating that in turns leads to the premature fatigue and downgrading of the equipment and transmission lines.

- *Heating of cables and equipment*: These effects can be medium-term (from a few seconds to a few hours), or long-term (from a few hours to a few years), and concern the cables which may be the source of overheating of the neutral and wound materials, such as transformers or motors.
- *Heating of capacitors*: Heating can be caused by losses due to the phenomenon of hysteresis in the dielectric. Capacitors are therefore sensitive to overloads, whether due to the high applied voltage, or to the presence of harmonics.
- *Overheating due to additional losses of machines and transformers*: Overheating caused by losses in the stators of machines and mainly in their rotor circuits, (cages, dampers, magnetic circuits), due to the large differences in speed between the rotating harmonic inducing fields and the rotor. The harmonics also generate additional losses in the transformers, by Joule effect in the windings, accentuated by the skin effect and losses that caused by hysteresis and eddy currents in the magnetic circuits.

1.6.3 Characterization of harmonic distortions

The Fourier series decomposition of the current absorbed by a nonlinear load can be modelled as an addition of several current sources, (one for each frequency component), placed in parallel as shown schematically in Figure 1-20.

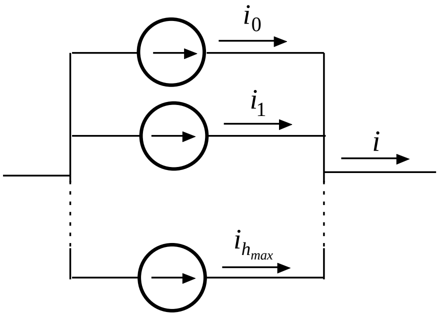

Figure 1-20 *Modeling of a nonlinear load.*

$$i = i_0 + i_1 + \cdots + i_{h_{max}} \tag{1-7}$$

The Harmonic distortion is often characterized by the well-known term *Total Harmonic Distortion (THD)*, and it defined as follows:

$$THD\% = \frac{\sqrt{\sum_{h=2}^{h_{max}} (X)_h^2}}{X_1} * 100\% \tag{1-8}$$

We can also define an *individual harmonic distortion* rate (*IHD*), which takes into account the distortion generated by a given harmonic frequency. This rate is given by:

$$IHD\% = \frac{X_h}{X_1} * 100\% \tag{1-9}$$

Where X represents the magnitude of the current or voltage. h_{max} is usually taken equal to 40 corresponding to the harmonic of frequency $2\ kHz$ if we consider the fundamental frequency of the system equals $50\ Hz$. The spectral distribution generally completes the information on the *THD*.

1.6.4 Power factor and Joule losses

The power factor PF is defined as the ratio between the active power P and the apparent power S:

$$PF = \frac{P}{S} \tag{1-10}$$

In a sinusoidal situation, it is sometimes called *displacement factor*, which is simply equal to the cosine of the shift angle between the voltage v and the current i. However, when the voltage and/or current is non-sinusoidal, the power factor is no longer the cosine of the shift angle between the voltage v and the current i. In this case the true power factor is always given by (1-10) taking into account the contribution of the harmonics to the active power P. Note that the true power factor is often deteriorated relative to the displacement [54]. Suppose a harmonic voltage and a current which can be expressed in Fourier series as follows:

$$v = \sum_{h=1}^{h_{max}} \sqrt{2}V_h \sin(h\omega_1 t + \theta_h), \qquad i = \sum_{h=1}^{h_{max}} \sqrt{2}I_h \sin(h\omega_1 t + \delta_h) \tag{1-11}$$

Then, the RMS values of voltage and current will be:

$$V = \sqrt{\sum_{h=1}^{h_{max}} {V_h}^2}\ , \qquad I = \sqrt{\sum_{h=1}^{h_{max}} {I_h}^2} \tag{1-12}$$

The average power will be given by:

$$P = \frac{1}{T}\int_0^T vi\, dt = \sum_{h=1}^{h_{max}} V_h I_h \sin(\emptyset_h) \qquad \text{where} \quad \emptyset_h = \theta_h - \delta_h \tag{1-13}$$

The *THD* of voltage and current are written according to equation (1-8) as:

$$THD_v\% = \frac{\sqrt{\sum_{h=2}^{h_{max}} (V)_h^2}}{V_1} * 100\% \tag{1-14}$$

$$THD_i\% = \frac{\sqrt{\sum_{h=2}^{h_{max}} (I)_h^2}}{I_1} * 100\% \tag{1-15}$$

Thus, the RMS values can be expressed, taking into account the equations (1-14) and (1-15) as follows:

$$V = V_1\sqrt{1 + (THD_v/100)^2} \tag{1-16}$$

$$I = I_1\sqrt{1 + (THD_i/100)^2} \tag{1-17}$$

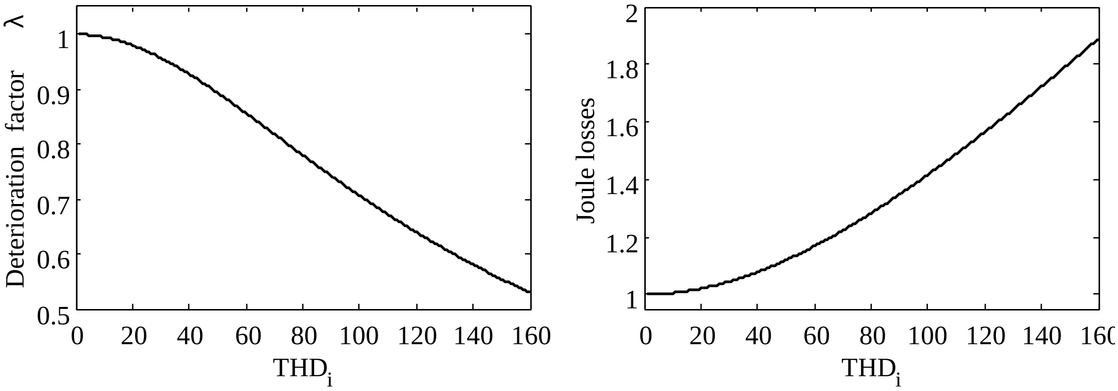

(a) Power factor

(b) Joule effect losses

Figure 1-21 *Effect of Harmonics on Power Factor and Joule Losses.*

The power factor can then be expressed in the following form:

$$PF = \frac{P}{V_1 I_1} * \frac{1}{\sqrt{[1 + (THD_v/100)^2].[1 + (THD_i/100)^2]}} = \frac{P}{V_1 I_1} * \lambda \tag{1-18}$$

Equation (1-18) shows that the power factor in the presence of harmonics is degraded by a coefficient depending on the voltage and current distortion rates. If we assume a sinusoidal voltage, then the active power would be carried only through the fundamentals, then (1-18) can be rewritten as follows:

$$PF = \frac{V_1 I_1 \cos(\emptyset_h)}{V_1 I_1} * \frac{1}{\sqrt{[1 + (THD_i/100)^2]}} = \lambda * \cos(\emptyset_h) \tag{1-19}$$

Admitting a unit displacement factor $\boldsymbol{cos}(\emptyset_{\boldsymbol{h}})$, Figure 1-21 (a) illustrates its degradation by the factor $\boldsymbol{\lambda}$ as a function of the harmonic distortion rate of the current. On the other hand, we can easily verify that the losses by Joule effects can be deduced as follows:

$$p_j = \mathrm{RI}^2 = \mathrm{RI}_1^2(1 + (THD_i/100)^2) \tag{1-20}$$

If we know that the Joule losses due to the fundamental are $\boldsymbol{1pu}$, then the effect of the harmonics is to increase these losses as shown in Figure 1-21(b).

1.7 Analysis of perturbation in electrical systems

The classical theory of electrical energy in electrical systems considered based only on pure sinusoidal signals. However, the electrical signals present on the networks and in particular, the currents, are often disturbed and they are not perfectly sinusoidal.

The analysis of non-sinusoidal signals based on mathematical concept allows the decomposition of disturbed electrical signals (non-sinusoidal) into ideal components and disturbances (Harmonics).

1.7.1 Decomposition into harmonic components

The concept of harmonics was introduced by Joseph Fourier, demonstrating that any non-sinusoidal periodic signal can be represented by a sum or series of sinusoids of discrete frequencies. The zero component is called the DC component, while the first component is called the fundamental component. In the case of grid-connected systems, this is a component at the nominal grid frequency ($50\ Hz$). The rest of the series components are called *harmonics*, and are multiples of the fundamental frequency.

Figure 1-22 illustrates the decomposition of the non-sinusoidal current of Figure 1-19 into fundamental component and harmonic components.

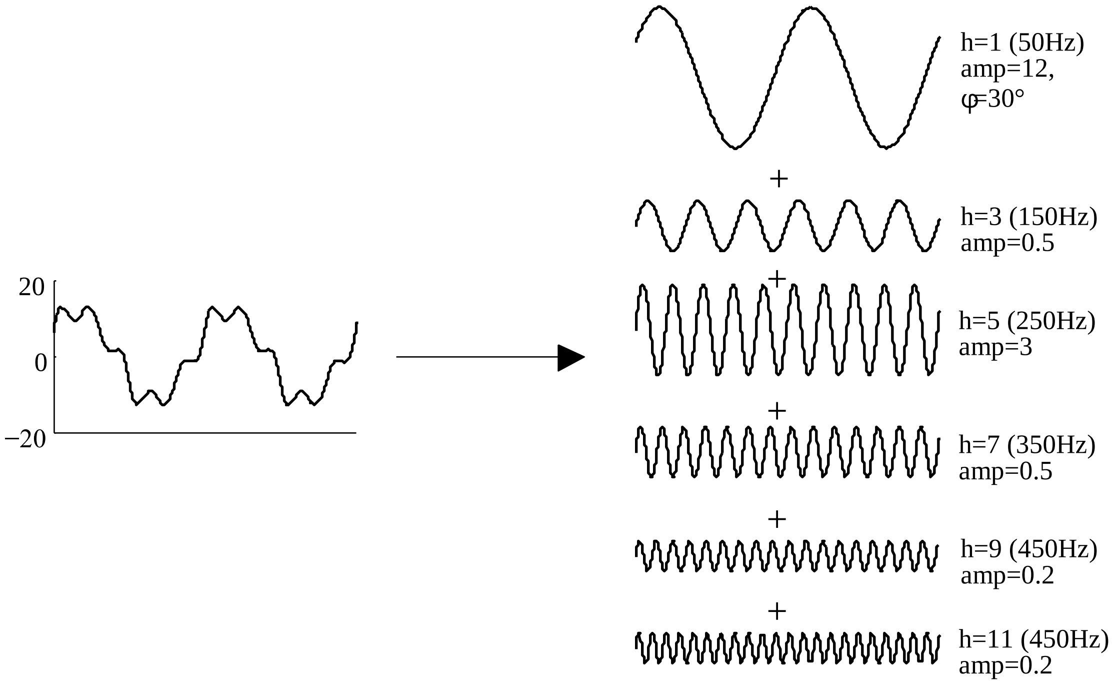

Figure 1-22 *Decomposition into harmonic components.*

1.7.2 Harmonic sequences

A three-phase non-linear load absorbs three-phase currents given by:

$$i_a = I_{a0} + \sum_{h=1}^{h_{max}} \sqrt{2} I_{ah} \sin(h\omega_1 t + \emptyset_{ah}) \tag{1-21}$$

$$i_b = I_{b0} + \sum_{h=1}^{h_{max}} \sqrt{2} I_{bh} \sin\left(h(\omega_1 t - \frac{2\pi}{3}) + \emptyset_{bh}\right) \tag{1-22}$$

$$i_c = I_{c0} + \sum_{h=1}^{h_{max}} \sqrt{2} I_{ch} \sin\left(h(\omega_1 t + \frac{2\pi}{3}) + \emptyset_{ch}\right) \tag{1-23}$$

In fact, it is not difficult to verify that each harmonic order forms a direct, inverse, or zero sequence system. For $h = 1$ the system is direct, (the formed system rotates in the direction *a-b-c*). For $h = 2$, the system is reversed because the direction of rotation is *c-a-b*, and for $h = 3$, the currents are in phase, which forms a homopolar system. In general, if we take into account only odd harmonics, (even harmonics are very rare), then the harmonic sequences can be summarized as follows:

- The ranks given by $6h + 1$, i.e., 1, 7, 13,… form direct systems;
- The ranks given by $6h + 5$, i.e., 5, 11, 17,… form inverse systems;
- The ranks given by $6h + 3$, i.e., 3, 9, 15,… form homopolar systems.

1.7.3 Energy theory

The first attempts to generalize the energy theory under harmonic distortions were introduced by Budeanu [55]. To recall the essentials of this theory, that is to say the harmonic voltage and current of order h given in complex form as follows:

$$v_h = \sqrt{2}V_h e^{j(h\omega_1 t+\theta_h)}, \qquad i_h = \sqrt{2}I_h e^{j(h\omega_1 t+\delta_h)}, \quad where\ \emptyset_h = \theta_h - \delta_h \tag{1-24}$$

The instantaneous real power is defined as follows:

$$p = \sum_{h=1}^{h_{max}} 2\Re\{v_h\}\Re\{i_h\} \tag{1-25}$$

With $\Re$ denotes the real part. By replacing v_h and i_h by their expressions given in (1-24), we find the expression of the instantaneous real power P, whose integration over a period makes it possible to calculate the average value of P, that called by Budeanu (*Active Power*), and it is given by:

$$P = \sum_{h=1}^{h_{max}} V_h I_h \cos(\emptyset_h) \tag{1-26}$$

The imaginary power is defined by Budeanu as the power that is in quadrature with the real power. It is given as:

$$q = \sum_{h=1}^{h_{max}} \sqrt{2}\Re\{v_h\}\sqrt{2}\Im\{i_h^*\} \tag{1-27}$$

With $\Im$ denote the imaginary part, i_h^* is the conjugate of i_h. Like the real power, imaginary power has an average value called (*Reactive Power*), and it is given after expansion and integration over the period of (1-27) as:

$$Q = \sum_{h=1}^{h_{max}} V_h I_h \sin(\emptyset_h) \tag{1-28}$$

Budeanu introduces a new quantity D, called (*distortion power*), given by:

$$D = \sqrt{S^2 - P^2 - Q^2} \tag{1-29}$$

This power is created due to the cross product between the harmonics of different frequencies.

1.7.3.1 Generalized energy theory

Budeanu's definition introduces the notion of distorting power, which has no clear physical meaning. Other analyzes and definitions of electrical power under harmonic distortions exist [56][57][58][59][60]. However, *the generalized energy theory* introduced by *Akagi et al.* [61], which allows a better decomposition of all disturbing phenomena, taking into account both harmonic distortions and imbalances. The author introduces three types of powers:

- *The real power* p, which is the real component of the power transmitted by the rotating components, (forward and reverse) of all harmonics including the fundamental.
- *The imaginary power* q, which is the imaginary component of the power transmitted by the rotating components, (forward and reverse) of all harmonics including the fundamental.
- *The zero-sequence power* p_0, which is the power transmitted by the zero sequence components.

These powers contain *continuous* parts, or average values, and *oscillating* parts with respect to the average values. These powers result from the products between harmonics of various characteristics. In the case of instantaneous real power, the continuous part $\bar{p}$ corresponds to the real part of the sum of the products between harmonics of the same frequencies and the same sequences.

$$\bar{P} = \sum_{h=1}^{h_{max}} 3V_h^+ I_h^+ \cos(\emptyset_h^+) + \sum_{h=1}^{h_{max}} 3V_h^- I_h^- \cos(\emptyset_h^-) \tag{1-30}$$

While the oscillatory part $\tilde{p}$, it corresponds to the real part of the sum of the products between harmonics of different natures, i.e., of different frequencies and/or sequences.

$$\tilde{P} = \begin{cases} \sum_{h=1}^{h_{max}} \left(-3V_h^+ I_h^- \cos(2\omega_h t + \theta_h^+ + \delta_h^-) - 3V_h^- I_h^+ \cos(2\omega_h t + \theta_h^- + \delta_h^+)\right) \\ + \sum_{h=1,k\neq h}^{h_{max}} \left(\sum_{h=1}^{h_{max}} 3V_k^+ I_h^+ \cos\left((\omega_k - \omega_h)t + \theta_k^+ - \delta_h^+\right)\right) \\ + \sum_{h=1,k\neq h}^{h_{max}} \left(\sum_{h=1}^{h_{max}} 3V_k^- I_h^- \cos\left((\omega_k - \omega_h)t + \theta_k^- - \delta_h^-\right)\right) \\ + \sum_{h=1,k\neq h}^{h_{max}} \left(\sum_{h=1}^{h_{max}} -3V_k^+ I_h^- \cos\left((\omega_k - \omega_h)t + \theta_k^+ - \delta_h^-\right)\right) \\ + \sum_{h=1,k\neq h}^{h_{max}} \left(\sum_{h=1}^{h_{max}} -3V_k^- I_h^+ \cos\left((\omega_k - \omega_h)t + \theta_k^- - \delta_h^+\right)\right) \end{cases} \tag{1-31}$$

The same analysis is applicable for the instantaneous imaginary power q. Therefore, its continuous part $\bar{q}$ will be:

$$\bar{q} = \sum_{h=1}^{h_{max}} -3V_h^+ I_h^+ \sin(\emptyset_h^+) + \sum_{h=1}^{h_{max}} 3V_h^- I_h^- \sin(\emptyset_h^-) \tag{1-32}$$

The oscillatory part $\tilde{q}$ will have as an expression:

$$\tilde{q} = \begin{cases} \sum_{h=1}^{h_{max}} (3V_h^+ I_h^- \sin(2\omega_h t + \theta_h^+ + \delta_h^-) - 3V_h^- I_h^+ \sin(2\omega_h t + \theta_h^- + \delta_h^+)) \\ + \sum_{h=1,k\neq h}^{h_{max}} \left(\sum_{h=1}^{h_{max}} -3V_k^+ I_h^+ \sin\left((\omega_k - \omega_h)t + \theta_k^+ - \delta_h^+\right)\right) \\ + \sum_{h=1,k\neq h}^{h_{max}} \left(\sum_{h=1}^{h_{max}} 3V_k^- I_h^- \sin\left((\omega_k - \omega_h)t + \theta_k^- - \delta_h^-\right)\right) \\ + \sum_{h=1,k\neq h}^{h_{max}} \left(\sum_{h=1}^{h_{max}} 3V_k^+ I_h^- \cos\left((\omega_k + \omega_h)t + \theta_k^+ + \delta_h^-\right)\right) \\ + \sum_{h=1,k\neq h}^{h_{max}} \left(\sum_{h=1}^{h_{max}} -3V_k^- I_h^+ \cos\left((\omega_k + \omega_h)t + \theta_k^- + \delta_h^+\right)\right) \end{cases} \tag{1-33}$$

For the zero-sequence power, there is no sequence difference between harmonics, but quite simply a frequency difference. So for the continuous part p_0:

$$\bar{P}_0 = \sum_{h=1}^{h_{max}} 3V_h^0 I_h^0 \cos(\emptyset_h^0) \tag{1-34}$$

And the oscillating part $\tilde{p}_0$:

$$\tilde{P}_0 = \begin{cases} \sum_{h=1}^{h_{max}} -3V_h^0 I_h^0 \cos(2\omega_h t + \theta_h^0 + \delta_h^0) \\ + \sum_{h=1,k\neq h}^{h_{max}} \left(\sum_{h=1}^{h_{max}} 3V_k^0 I_h^0 \cos\left((\omega_k - \omega_h)t + \theta_k^0 - \delta_h^0\right)\right) \\ + \sum_{h=1,k\neq h}^{h_{max}} \left(\sum_{h=1}^{h_{max}} -3V_k^0 I_h^0 \cos\left((\omega_k - \omega_h)t + \theta_k^0 + \delta_h^0\right)\right) \end{cases} \tag{1-35}$$

1.8 International standards

This International Standard limits harmonic distortions, which are intended to reduce their impact on electrical power systems. There are two standardization bodies in this field, the IEEE standard (*Institute of Electrical and Electronics Engineers*), and IEC standard (*International Electro-technical Committee*). The first one defines the quality standards in the publication IEEE-519, *Recommended Practices and Requirements for Harmonic Control in Power Systems* [62], while the second body defines the standards of *Electromagnetic Compatibility* (*EMC)*, grouped in the publication IEC-61000. Appendix A demonstrating the three most important IEC standards concerning harmonic distortions [63][64][65].

1.9 Solutions for harmonic depollution

Improving the quality of energy, and in particular harmonic depollution, aims to minimize their impact on loads and network equipment. There are two main strategies for harmonic depollution: *modification* and *compensation*. Modification

The modification strategy represented in modifying the characteristics of the loads or sources in order to reduce the generation of harmonics and their propagation in the network. The following examples can be cited:

- Replacement of the conventional polluting sources by more sinusoidal sampling topologies, such as PWM rectifiers, multi-level structures [66];
- The reinforcement of the network makes it possible to reduce the total impedance upstream of the polluting load, and thus reducing the impact of harmonic currents on the voltages, consequently, protect the healthy loads;
- The transformer coupling mode can be used to isolate certain harmonics. We can cite two interesting examples illustrated in Figure 1-23. The first can serve as a sinusoidal sampling structure with respect to the network. Indeed the 5^{th} and the 7^{th} harmonics are in general the most persistent especially in regulated training. With this assembly, although they circulate before the bus-bar, they are simply cancelled on the upstream side. The second example in the figure shows the influence of the transformer coupling mode on the flow of zero sequence currents and therefore the neutral current: the $Y-\Delta$ coupling (Δ is the upstream side) is able to contain the zero sequence currents in the Δ side without being able to exit. We can also cite the zigzag transformer widely used for the control of zero sequence currents;
- … etc.

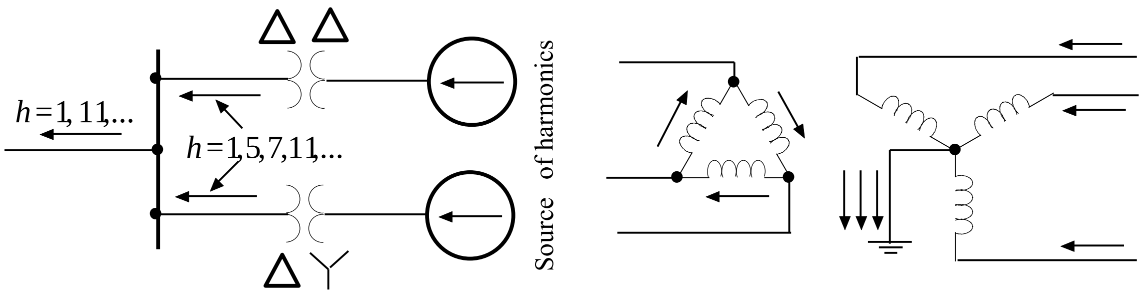

(a) (b)

Figure 1-23 *Isolation of harmonics by special transformer couplings; (a) Isolation of* 5^{th} *and* 7^{th} *harmonics, (b) Isolation of zero sequence harmonics.*

1.9.1 Compensation

This second strategy serves to mitigate or eliminate the undesirable components already generated by the polluting loads. In this strategy, one finds as examples the compensation of the reactive power by the traditional or modern processes, but also is especially the harmonic filtering. The latter is now considered the most suitable solution given the accelerated proliferation of non-linear charges. The traditional solution for this strategy is passive filtering; however it is becoming more and more difficult to adapt this classic solution to evolving loads and requirements, which has given birth to a modern solution which is active filtering.

1.10 Passive filters

This is the classical solution for harmonic filtering. Its principle is to trap unwanted frequencies in passive element systems (RLC), connected in series or in parallel with the network and forming very low impedances with respect to the frequencies to be filtered. A series filter, mainly used for filtering voltage harmonics and acts as an isolator, that is to say it must manifest a high enough impedance against the harmonics in order to prevent them from propagating.

The shunt filter (parallel) is more suitable for filtering harmonic currents. Placed in bypass with the network, it is capable of supplying reactive power at the fundamental frequency. Several passive filters exist [52]:

1.10.1 Resonant filter

The resonant filter exhibits, according to the tuned values of L and C, a resonance at the frequency that intended to be eliminated (Figure 1-24 (a)). In addition to the fact that a filter must be provided for each phase, a filter is also necessary for each frequency to be filtered. Although it is capable of improving the power factor in addition to the harmonic filtering.

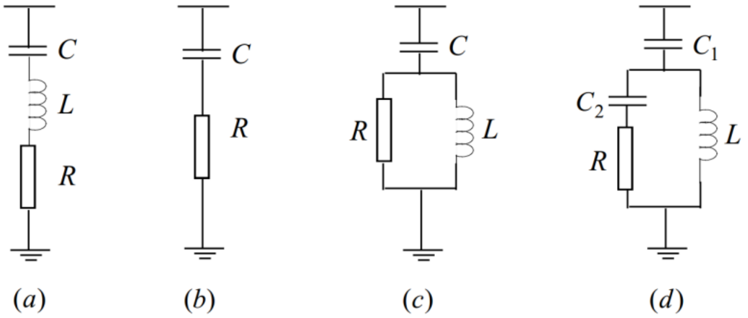

Figure 1-24 *Passive filters: (a) resonant filter, (b)* 1^{st} *order damped filter, (c)* 2^{nd} *order damped filter, (d)* 3^{rd} *order damped filter.*

However, the resonant filter can be the source of unwanted resonance phenomena with the elements of the network, which is why it is highly recommended to predict the behaviour of the passive network-filter in the presence of harmonics.

1.10.2 Damped filter

The damped filter can reduce the risk of unwanted resonance, and can greatly reduce the size of the passive filter, operating over a wide frequency range. There are three types of damped filters; the first-order filter, the second-order filter, and the third-order filter (Figure 1-24 (b)(c)(d)). The first-order filter is used very rarely because it requires a large capacity and causes high power losses. The second and third-order filters are performing much better in this regard.

In practice, it is common to implement resonant filters in parallel with a damped filter as shown in the Figure 1-25. The resonant filters are tuned to eliminate low frequency harmonics like the 5^{th} and 7^{th}, while the damped filter takes care of the higher harmonics.

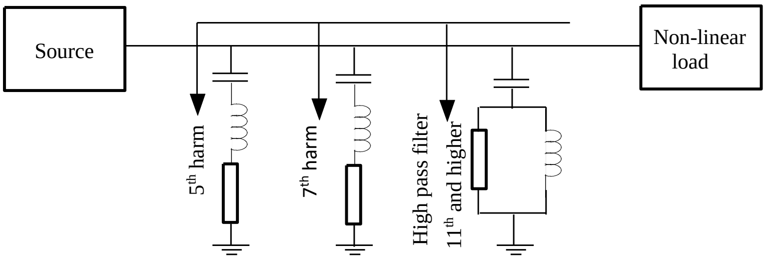

Figure 1-25 *Practical example of a combination of resonant and damped passive filters.*

1.11 Active filters

The aforementioned traditional solutions for power quality improvement, particularly for harmonic depollution, can have more drawbacks than advantages, which is why active filtering is the most desirable solution today, especially for harmonic filtering.

The principle of operation was presented in the early 1970s, and a few years later, an inverter-based prototype using naturally-switched Thyristors have emerged [67][68]. However, this type of semiconductor immediately posed the problem of switching harmonics. This drawback also posed the same problem when implementing a reactive power compensator [69]. It was during the 1980s [70][71], and especially the 1990s [72][9], a great progress was made thanks to the development of semiconductor technology, and in particular to the advent of power switches based *PWM* controlled such as *GTO* and *IGBT*. Today, active power filters have reached unprecedented technological maturity. They are used for compensating harmonic currents and voltages, compensating reactive power and regulating the voltage (voltage sag (dip) and voltage flicker), compensating for unbalances in three-phase systems, etc. Recently, the active filters have been more and more developed so that dedicated to consider as much as possible all the recent power quality requirements and standards [73][74][75][76][77].

1.11.1 Principle of active filter

The power electronics converter is the heart of the active filter, which is generally an inverter connected to the network through passive elements. This current or voltage controlled system is then capable of reproducing and injecting equivalent voltage or current components into the network, but in opposition phase to the undesirable components generated by the polluting loads in order to eliminate them. An active filter can be connected to the Point Common Coupling (PCC) for global or individual compensation.

1.11.2 Classification of active filters

Active filters can be classified according to several criteria, such as its configuration in relation to the network, the type of the inverter that is used, the number of wires…etc. Regarding the configuration in relation to the network, a distinction is made between the *Shunt Active Filter*, the *Series Active Filter*, and the *Universal Filter*.

1.11.2.1 Shunt active filter

The active shunt or parallel filter is the most used configuration, and undoubtedly the most interesting for the pollution control of harmonic currents [78]. Figure 1-26 shows the block diagram of this type of filter, where the inverter is connected to the grid through an inductive filter, and possibly through a transformer. On the DC side, the inverter uses capacitance as the voltage source. The purpose of this configuration is to decouple the disturbances caused by the polluting load of the upstream electrical network. The polluting load represented by a rectifier supplying an *RL* load that absorbs a current i_L which contains, in addition to the fundamental, harmonic components that the active filter must eliminate by injecting them in the opposite direction into the network as a harmonic current i_c, thus the source current i_s remains sinusoidal and possibly in phase with the voltage.

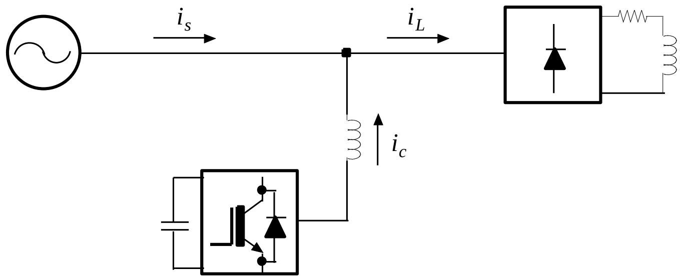

Figure 1-26 *Shunt active filter.*

1.11.2.2 Series active filter

This configuration is used to ensure the quality of the voltage. The block diagram of this type of filter is shown in Figure 1-27, where the voltage inverter this time is connected to the grid through a passive filter of *LC* type and a series transformer. The active filter must inject a certain voltage v_C to the voltage wave v_L, disturbed by harmonic distortions, imbalances, etc [79]. This topology can also play the role of a *Dynamic Voltage Restorer DVR* to protect the load against possible voltage dips or cuts [80].

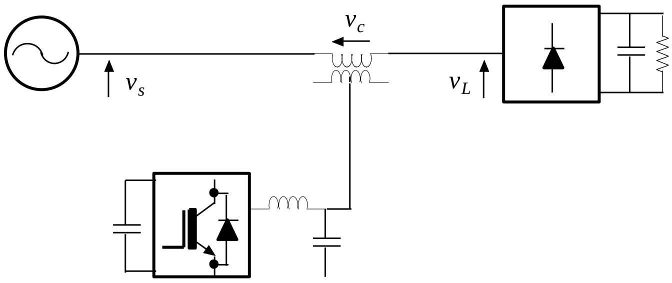

Figure 1-27 *Series active filter.*

1.11.2.3 Universal active filter

This configuration, the block diagram of which is in Figure 1-28, is a combination of a shunt active filter and a series active filter, which is often known as (*Unified Power Quality Conditioner UPQC*) [81]–[84]. This structure makes it possible to search for several functions simultaneously, serving to improve the quality of the voltage (harmonic compensation, reactive power, voltage regulation and stabilization, etc.). The main functions of the series filter are to isolate the harmonics between the source and the polluting load, to compensate for reactive power and unbalanced voltages. While the role of the shunt filter is to absorb the harmonic currents to compensate the reactive power, to compensate the negative sequence currents, and to regulate the capacity of the DC bus between the two active filters.

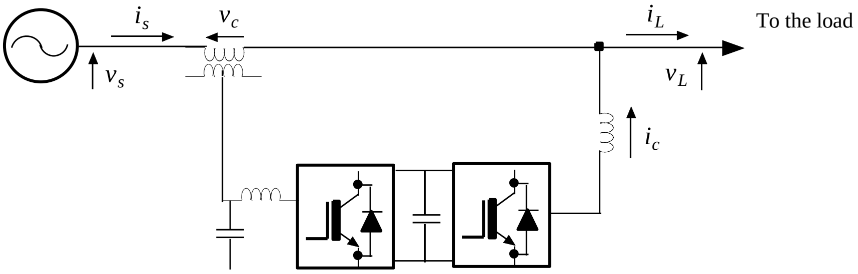

Figure 1-28 *Universal active filter (UPQC).*

1.12 Active power filter associated with RE sources (State-of-art)

Recently, several works have been presented in which the APF is associated with renewable energy conversion systems to provide a clean sustainable energy and ensure sufficient PQ level that can come with different topologies and various control strategies. Figure 1-29 chows the general structure of the system.

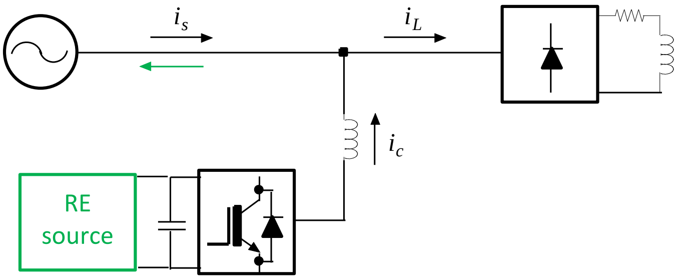

Figure 1-29 *General structure of APF associated with RE source.*

In *Bouzelata Y. et al.* [85] and *Noroozian R. et al.* [86], a double stage structure is used to ensure the conversion from DC to AC, in turn decreases the overall system's efficiency; Moreover, the conventional PI controller is used to regulate the DC voltage, while the inverter is controlled using hysteresis controller with the disadvantage of changing current ripple due to the variation of the switching frequency. In *Sezen S. et al.* [87] and *Singh Y. et al.* [88], a single-stage topology is adopted; However, the voltage and the current regulation are based on PI and hysteresis controllers respectively. This strategy can offer a bad dynamic response and reduce the system stability. In *Fernando M. et al.* [89], PSO algorithm has been used instead of the conventional MPPT, such as P&O, to address the shading problem. The combined operation of the PV array and the APF has been successfully achieved with higher efficiency when the PV array undergoes partial shading; however, the total harmonic distortion (THD) of the injected current is still important. In *Safa A. et al.* [90], an intelligent controller SMC is used to regulate the DC voltage but no MPPT is implemented, also the inverter current is controlled using hysteresis controller despite its disadvantages. In *Demirdelen T. et al.* [91], a DC/DC converter is included to implement the P&O MPPT, reducing by this way the overall efficiency. Moreover, the system topology is based on cascaded inverters, according to *Ref.* [92] this topology solution is 1% less efficient than the central inverter architecture. *Kumar R. et al*. [93] have used ANFIS-based MPPT to harvest maximum power from PV. They have used fuzzy logic-based MPPT controller to obtain the data by training the ANFIS controller. In the same reference, interesting DC-link voltage control has been achieved using a double stage PV-APF structure. Similar MPPT has been used in *Kumar R. et al*. [94] to harvest the maximum power from PV source. The latter is combined with a wind turbine driven PMSG and fuel cell system. The previous three renewable energy sources have been connected through an APF to the grid PCC using again double stage topology where the second stage is always controlled by the conventional hysteresis controller.

Table 1-4 reports other relevant works in terms of system topology, inverter structure, control strategy, and results.

1.13 Conclusion

This chapter has been devoted to the study of the photovoltaic systems on one hand and problems of electric power quality on the other hand. We presented the different classifications and topologies of photovoltaic systems, followed by a reading on techniques for extracting the maximum power from the photovoltaic generator. Then, we discussed the effects, causes and consequences of harmonics on the electrical network. To reduce these effects, different traditional and modern solutions were presented. The use of active filters is presented as a better solution for all types of disturbances that appear in the electrical network. As a further solution, one system will be dedicated to satisfy both the energy demand from PV source and power quality improvement; and what will see in the upcoming chapters.

Table 1-4 *Summery of recent research papers regarding APF associated with PV system.*

Reference	Electrical system part		Control part					Results			
	System topology	**Inverter type**	**MPPT algorithm**	**Switching control**	**DC voltage regulator**	**Inverter control based**	**Harmonic extraction technique**	**Results validation**	**Power rating**	**Grid Voltage**	**THD_i**
M.A.Alalia *et al.* (2021) [97]	SS	3-Ø 2-L	P&O	SPWM	PI	RST-controller	*p-q* theory	Simulation	49.4kW	20kV	1.41%
J. A. Cortajarena *et al.* (2019) [96]	SS	3-Ø 2-L	P&O	SVPWM	SMC	SMC	*p-q* theory	Experiment	2.6kW	380V	4.4%
S. Kumar Prince *et al.* (2019) [95]	DS	3-Ø 2-L	Single Sensor-based MPPT	SPWM	N/A	N/A	Extended Kalman Filter	Experiment	300W	40V	2.26%
R. Kumar *et al.* (2019) [93]	DS	3-Ø 2-L	Adaptive neuro-fuzzy	HB-PWM	Adaptive neuro-fuzzy	HCC	SRF theory	Real-time simulation	28kW	230V	1.98%
Y. Singh *et al.* (2018) [88]	SS	1-Ø 2-L	P&O	HB-PWM	PI	HCC	(SOGI)	Experimental	5.3kW	230V	2.4%
A. Safa *at al.* (2018) [90]	DS	3-Ø 2-L	N/A	HB-PWM	SMC	HCC	*p-q* theory	Experiment	826W	70V	2.5%

Reference	Electrical system part		Control part					Results			
	System topology	Inverter type	MPPT algorithm	Switching control	DC voltage regulator	Inverter control based	Harmonic extraction technique	Results validation	Power rating	Grid Voltage	THD$_i$
T. Vigneysh *et al.* (2017) [100]	DS	3-Ø N/A	N/A	SPWM	adaptive fuzzy PI (AFPI)	AFPI	*d-q theory*	Simulation	27.5 kW	400V	1.16%
T. Demirdelen *et al.* (2017) [91]	DS	3-Ø Modular Cascaded Inverter	P&O	SPWM	PI	N/A	*d-q theory*	Simulation	100kW	6.3kV	1.64%
S. Ouchen *et al.* (2016) [99]	DS	3-Ø 2-L	FLC	DPC-PWM	PI	Direct Predictive Control (DPC)	DPC based	Experiment	350W	N/A	4.71%
B. Boukezata *et al.* (2016) [98]	SS	3-Ø 2-L	P&O	DPC-PWM	PI	DPC	DPC based	Experiment	6kW	80V	1.41%
Y. Bouzelata *et al.* (2015) [85]	DS	3-Ø 2-L	P&O	HB-PWM	PI	HCC	*p-q* theory	Simulation	N/A	230V	1.42%
F.M. de Oliveira *et al.* (2015) [89]	SS	1-Ø 2-L	PSO	SPWM	PI	PI-MR	SRF theory	Experiment	2.4kW	127V	2.0%

* N/A: not available, SS: Single-stage, DS: Double-stage, Ø: Phase, L: level, HCC: Hysteresis Current Controller, HB-PWM: Hysteresis based PWM, Sinusoidal PWM: SPWM, Space Vector PWM: SVPWM.

Chapter 2: Three-Level T-type Inverter Based M-SVPWM for Power Quality Improvement

2.1 Introduction

Recently, multilevel inverters have received more and more attention compared with conventional two-level topology. This is due to many advantages that multilevel inverter can offers especially in terms of power quality which is one of the main focus of our work, like lower electromagnetic interference (EMI), lower switching losses, lower THD value and lower voltage stress.

T-type three-level inverter considered as one of the promising topologies compared with the other inverters family. This converter starts to be common in automotive and photovoltaic (PV) systems to attain high-energy conversion efficiency and better power quality [101]. Many modulation techniques are used to drive such converters, Space vector PWM (SVPWM) is the most promising one. Compared with the former sinusoidal modulation method (SPWM), the proposed technique can offer lower current harmonics, flexible generation of gate driving signals, and higher modulation index of 15% [102][103].

In this chapter, a state and modelling of the T-type three-level inverter is firstly discussed. Secondly, based on the topological structure of the proposed three-level inverter, the switching control principle of the Modified Space Vector Pulse Width Modulation (M-SVPWM) is analysed. The modification here can offer a great reduction of computations compared with the conventional one, which grants an easy digital implementation. At last, the proposed switching control based M-SVPWM is programmed and lunched in a cost-effective STM32F4 Discovery board and tested with three-level T-type inverter implemented in PCBs.

2.2 DC/AC converters (Inverters)

A power electronics device which converts DC power to AC power at required voltage magnitude (V) and frequency (Hz) is known as an *Inverter*. There are two common types of inverters, voltage source inverters (VSI) when the inverter has a DC source with small or negligible impedance and current source inverters (CSI) when the input DC source has a high impedance. VSI is frequently used in PV system application due to its high dynamic performance, and greater degree of controllability compared to the CSI [104][105].

Two categories into which inverters can be classified, two-level inverters and multi-level inverters. Comparatively, the multi-level inverter has many advantages such as better quality output voltage waveform, minimum harmonic distortion of output voltage and current waveforms, higher operating voltage ability with lower voltage semiconductor devices, lower *dv/dt* stress, lower electromagnetic interference, size-reduced of passive filters, lower torque ripple in motor application and possible fault-tolerant operation [106][107]. Which makes it in turn more suitable for low and medium power applications such as PV systems.

Figure 2-1 shows a simple flowchart of the classification of voltage source inverters that are mostly used in power applications. For the multilevel inverter, several topologies have been given in the survey [108]. As the three-level T-type inverter is considered one of the promising topologies for PV system applications, this work will mainly focus on this topology.

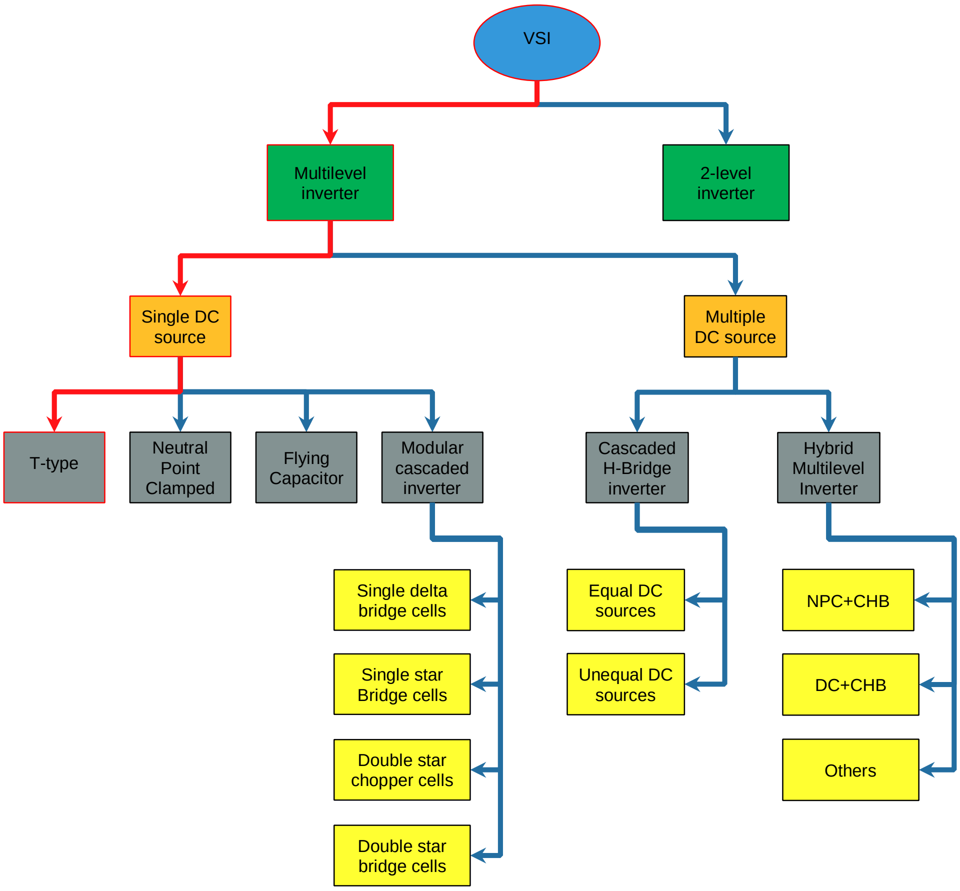

Figure 2-1 *Classification of votage source inverters.*

2.3 Two-level Inverter

The two-level three-phase voltage source inverter consists of three arms. Each arm has two bidirectional switches, which work in a complementary way to avoid short circuit of the DC voltage source at the input of the inverter. The bidirectional switch can be realized by a power switch (usually IGBT or MOSFET) with an antiparallel power diode. The diagram of the inverter is shown in Figure 2-2.

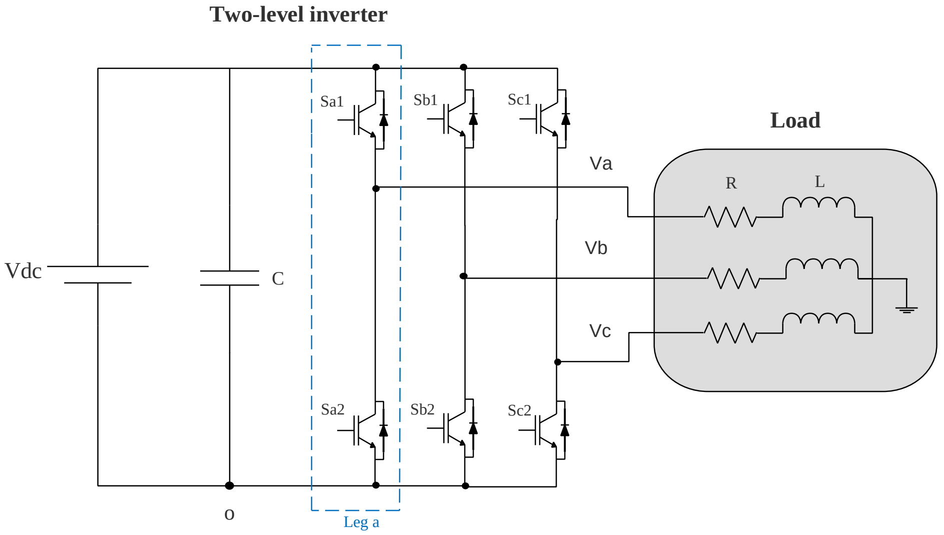

Figure 2-2 *Circuit diagram of two-level inverter.*

The inverter is composed of six switches, where the output voltage for each leg V_a, V_b, V_c, depends solely on V_{dc} and the switch status. The switches in each inverter leg can have two different states $[P]$ and $[O]$, where $[P]$ state is when the upper switch turned ON, and $[O]$ state is when the lower switch turned ON.

The different states for each leg can be seen in Table 2-1. Where x represents the legs (*a*, *b* or *c*).

Table 2-1 *Switching states for a three-phase two-level inverter.*

Switching States	Status of switching devices (x=a,b,c) (1=ON, 0=OFF)		Terminal voltage
	Sx1	**Sx2**	
P	1	0	V_{dc}
O	0	1	0

Two-level three-phase inverters are commonly used in applications due to their simple structure such as ac motor drives. However, at medium and high power levels power quality is an important factor. So, if the harmonics can be reduced by using a different inverter topology, then the filter size can also be reduced hence the cost-effectiveness. Therefore, a lot of effort is being made on multilevel inverters that have three or more levels such as the three-level T-type inverter in which will be discussed and analyzed in the upcoming section.

2.4 Numerical simulation of two-level inverter

Using Matlab/Simulink tool, the association of the two-level inverter controlled by space vector modulation with a $12.5\ kVA$ three-phase RL load at 0.8 power factor lagging is simulated.

To be able to obtain an output voltage of the inverter on the scale of the nominal voltage of the load ($380\ Vrms$), we need to supply the inverter by a DC source of value $Vdc = 670\ V$ if we consider the maximum modulation index m_a is equals to 0.8.

The space vector modulation is characterized by the modulation index rate m_a, and the switching period T_s (or switching frequency f_s), where $f_s = 1/T_s$. The system is simulated for a modulation rate $m_a = 0.8$ and a switching period $T_s = 100 * 10^{-6} s$, which corresponds to a switching frequency $f_s = 1 / T_s = 10kHz$. The period of the output voltages being $T = 0.02\ s$ that corresponds to $50\ Hz$, we deduce that the number of switching interval per period is $n = T/T_s = 0.02/(100 * 10^{-6}) = 100$ intervals.

Figure 2-3 (a), (b) and (c) present the waveform of the voltage between phase and neutral of the source V_{ao}, the voltage between phases V_{ab}, and the voltage between phase and neutral of the load V_a, respectively. As expected, voltage V_{ao} has two voltage levels, V_{ab} has three levels, and V_a has five levels. The voltage V_a envelops the reference V_a^*, so that the fundamental V_a of coincides with V_a^*. Figure 2-4 shows also the trajectory of the reference voltage vector V_a^* for different modulation rates in the αβ plan of the SVM hexagon that formed by the output states of the two-level inverter. Figure 2-5 and Figure 2-6 demonstrate that for the same switching period ($n = 100, T_s = 100 * 10^{-6} s$), the amplitude of the fundamental is proportional to the modulation rate m_a, while the THD is inversely proportional to the modulation rate m_a. Harmonic analysis of the output voltage V_a (Figure 2-7) shows that the harmonics are centred around the multiples of the ratio n. The greater this ratio, the more the harmonics are pushed towards high orders. Figure 2-8 shows that for the same modulation rate ($m_a = 0.8$), the amplitude of the fundamental of the voltage V_a is not affected by the variation of the switching intervals *n*. While the THD -measured from harmonic 2 to harmonic 1000- is inversely proportional to the switching intervals. We can see clearly that the quality of output voltage is better for higher values of *n*. However, the higher switching frequency, the higher switching losses in the inverter. Therefore, the switching frequency must be reasonably set to balance between the quality of output waveforms and the efficiency of the inverter [109].

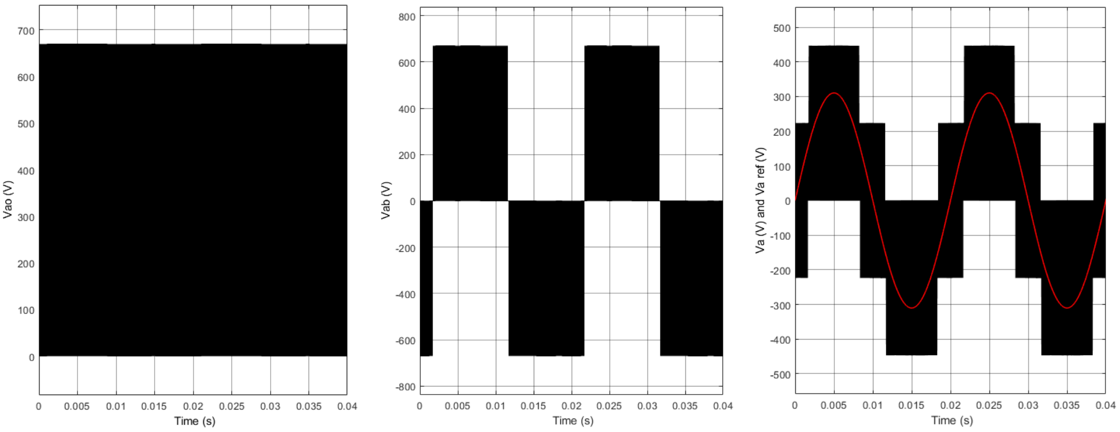

(a) (b) (c)

Figure 2-3 *(a) Phase-neutral source voltage, (b) Phase-to-phase voltage, (c) Phase-to-ground load voltage (*$\boldsymbol{m_a = 0.8, f_s = 10kHz}$*).*

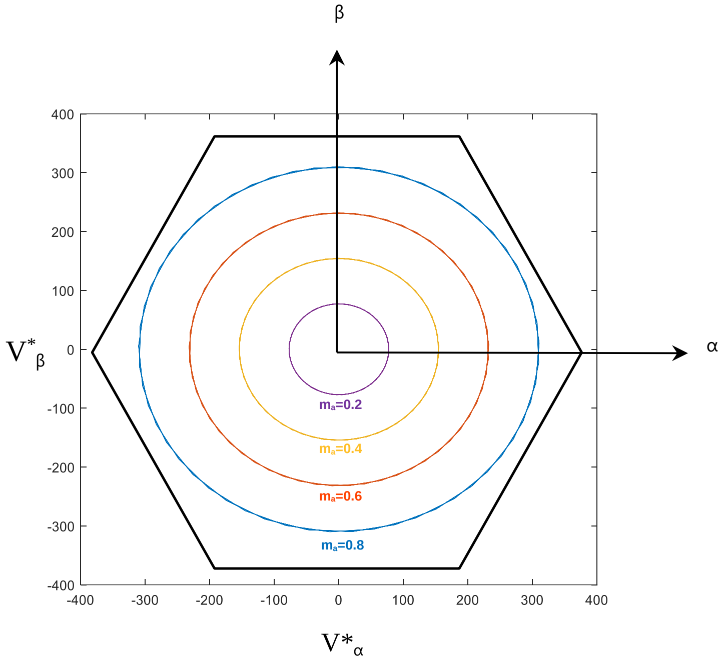

Figure 2-4 *Voltage reference* $\boldsymbol{V_a^*}$ *in αβ plan for different modulation index.*

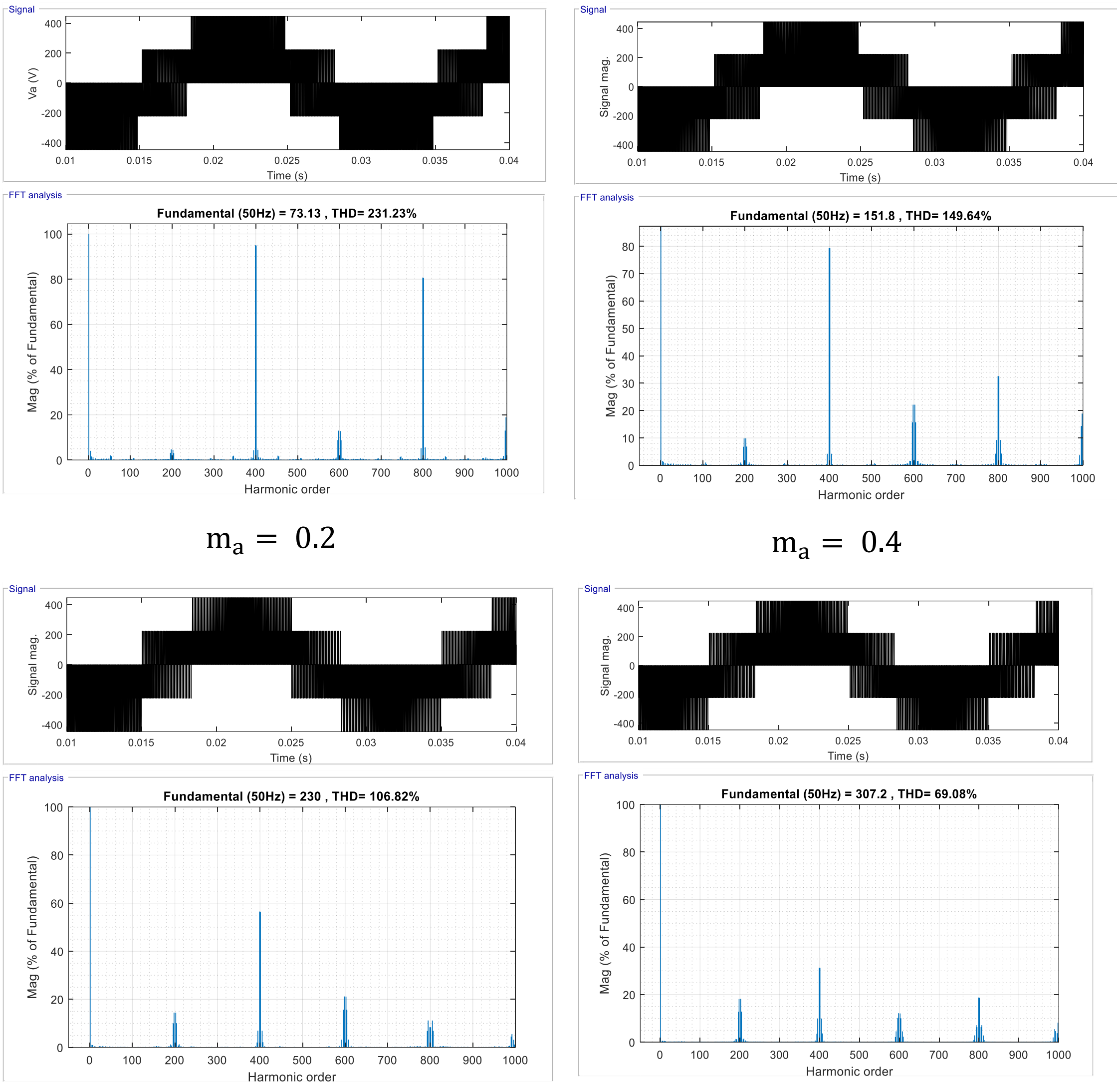

$m_a = 0.2$

$m_a = 0.4$

$m_a = 0.6$

$m_a = 0.8$

Figure 2-5 *Harmonic analysis of the load phase volatge with different modulation index.*

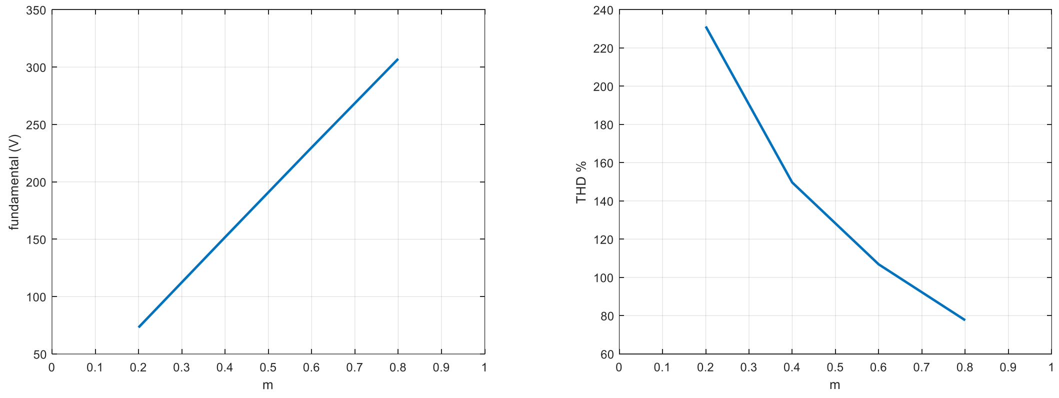

Figure 2-6 *The evolution of the voltage fundamental and THD with respect to the modulation index.*

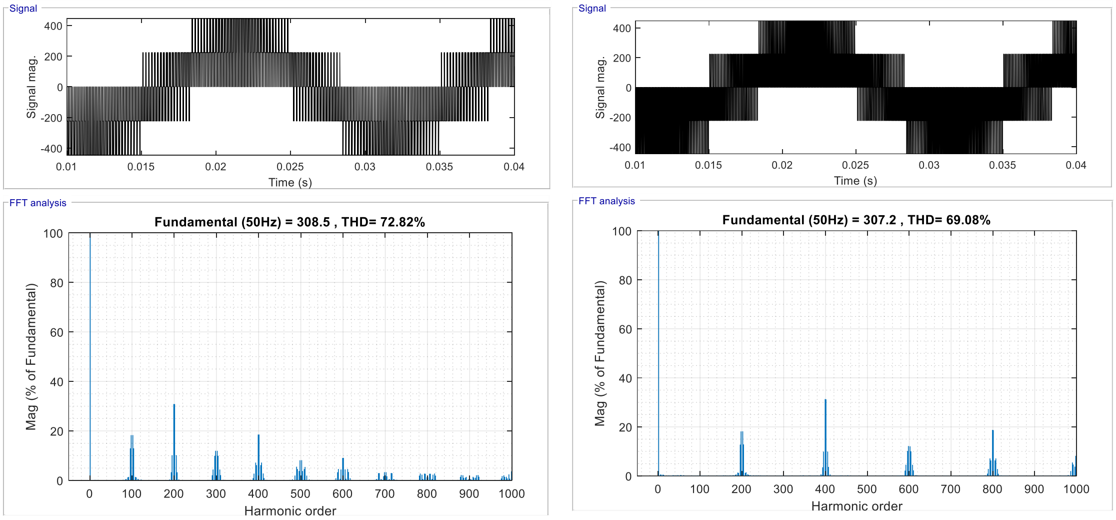

$n = 100\ (5kHz)$ $n = 200\ (10kHz)$

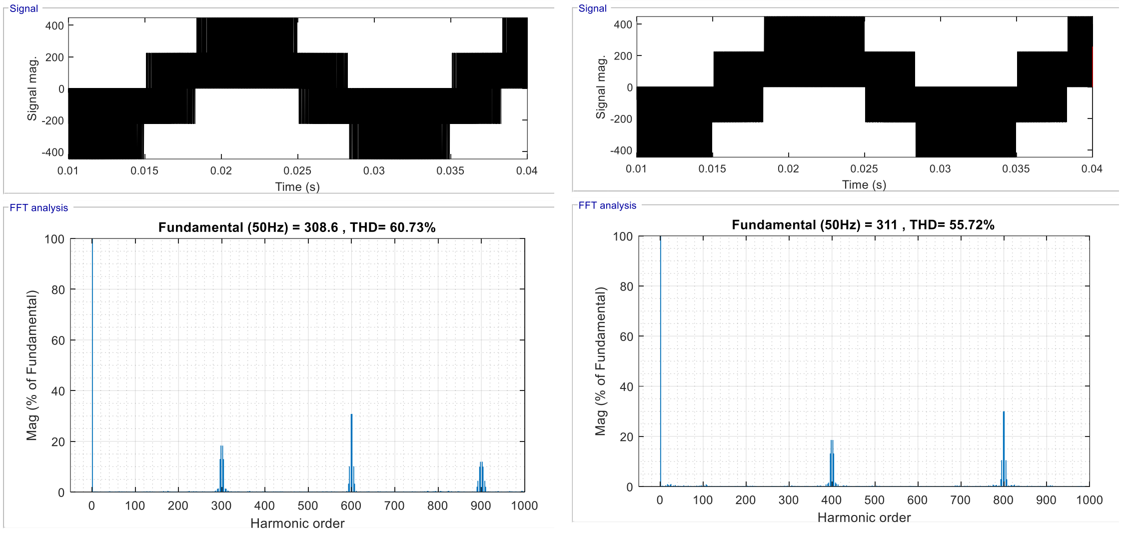

$n = 300\ (15kHz)$ $n = 400\ (20kHz)$

Figure 2-7 *Harmonic analysis of the load phase volatge with different switching frequency.*

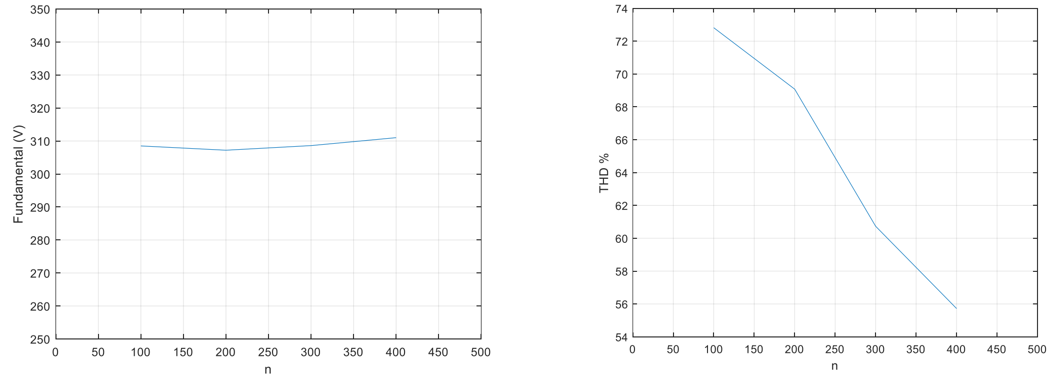

Figure 2-8 *The evolution of the voltage fundamental and THD with respect to the switching interval.*

2.5 Three-level T-type inverter (structure and concept)

The three-level T-type inverter has proven itself as a high-efficiency power converter for PV systems [110]. In comparison with the conventional Neutral Point Clamped (NPC) inverter [111], the T-type inverter utilizes two active bidirectional switches to the DC-link voltage neutral point, which can minimize two clamping diodes per phase leg, thus creating a third output voltage level without the need of clamping diodes [112]. As a result, lower conduction losses and smaller implementation size. Moreover, each bidirectional switch to the DC-link neutral point has to withstand only half of the DC-link voltage, which makes it feasible for the usage of lower voltage power devices [113]. However, during the switching process, both converters (T-type and NPC converter) have just to switch half of the dc-link voltage.

The power circuit diagram of a three-level T-type converter is shown in Figure 2-9. Each leg is composed of four active switches S_1 to S_4 with their antiparallel diodes (freewheeling diodes), shaping the corresponding letter “T”. Capacitors C1 and C2 at the DC side are used to split the DC input into two voltages and provide the neutral point o.

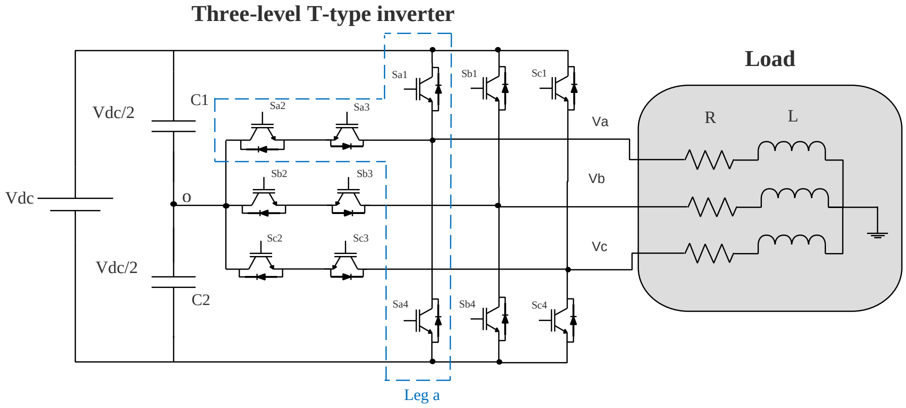

Figure 2-9 *Circuit diagram of three-level T-type inverter.*

Each leg in the T-type inverter can take one of three possible states $[P]$, $[O]$ or $[N]$, Table 2-2 illustrates the switching combinations for obtaining these states, where x represents the legs $(a, b\ or\ c)$.

Table 2-2 *Switching state for three-phase three-level T-type inverter.*

Switching States	**Status of switching devices (x=a,b,c) (1=ON, 0=OFF)**				**Terminal voltage**
	Sx1	Sx2	Sx3	Sx4	
P	1	1	0	0	$V_{dc}/2$
O	0	1	1	0	0
N	0	0	1	1	$-V_{dc}/2$

- $[P]$ State: during which switches Sx1 and Sx2, are ON, while Sx3 and Sx4, are OFF. As a result, the phase voltage is $+V_{dc}/2$.

- [O] state: during which switches Sx1 and Sx4 are OFF while Sx2 and Sx3 are ON. Therefore, the phase output voltage in this state is clamped at zero.

- [N] state: during which switches Sx1 and Sx2 are turned OFF, while Sx3 and Sx4 are in ON-state. Hence, the output phase voltage is $-V_{dc}/2$ in this state.

It can be observed that operations of switching devices in the same leg, such as a pair of Sx1 and Sx3 or a pair of Sx2 and Sx4, are complementary. When one of them in a pair is switched ON, the other in the same pair must be OFF. Both-ON or both-OFF situation of the complementary devices is not allowed.

Moreover, the transition between $[P]$ state and $[N]$ state is prohibited. Therefore, the dynamic voltage sharing problem could be avoided in the three-level inverter.

Furthermore, the magnitude of step changes of the output voltages in the three-level inverter is $V_{dc}/2$, which is only half of that in traditional two-level inverters. As a result, less voltage stress is generated.

2.6 Grid-interactive T-type three-level inverter model

As the output voltage of the three-level T-type inverter depends only on V_{dc} and the switching status, the switching position in Table 2-2 can be rewritten in a function form as follows [114][115]:

$$S_i = \begin{Bmatrix} 1 \rightarrow (V_i = 1/2\, V_{dc} \\ 0 \rightarrow (V_i = 0) \\ -1 \rightarrow (V_i = -1/2\, V_{dc}) \end{Bmatrix} \quad i = a, b, c \tag{2-1}$$

The three-level T-type inverter scheme supplied by a DC source connected to the grid is shown in Figure 2-10.

The three phase voltage expression of the T-type inverter is given in equation (2-2).

$$\begin{aligned} V_a &= Ri_a + L\frac{d}{dt}i_a + e_a \\ V_b &= Ri_b + L\frac{d}{dt}i_b + e_b \\ V_c &= Ri_c + L\frac{d}{dt}i_c + e_c \end{aligned} \tag{2-2}$$

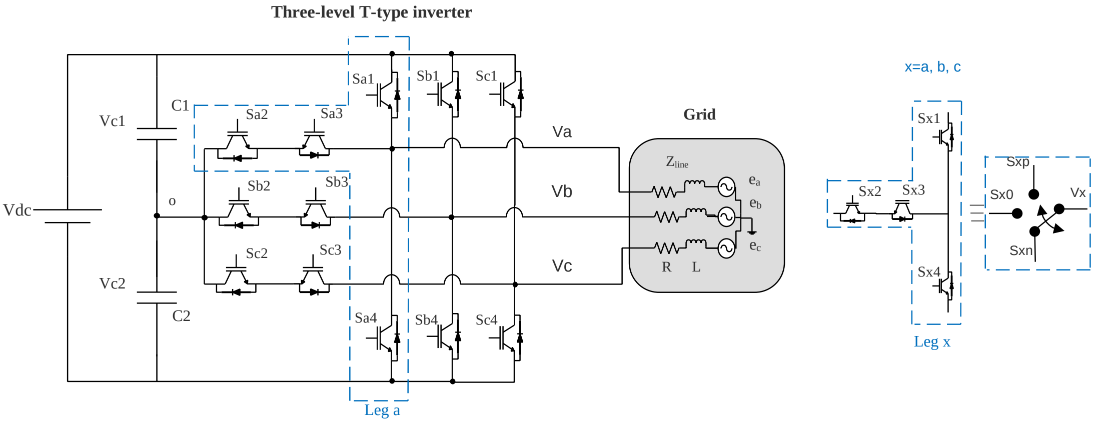

Figure 2-10 *Equivalent circuit model of a grid-interactive T-type inverter.*

Equation (2-2) can be expressed in a matrix form as follows:

$$\begin{bmatrix} V_a \\ V_b \\ V_c \end{bmatrix} = \begin{bmatrix} R & 0 & 0 \\ 0 & R & 0 \\ 0 & 0 & R \end{bmatrix} \begin{bmatrix} i_a \\ i_b \\ i_c \end{bmatrix} + \begin{bmatrix} L & 0 & 0 \\ 0 & L & 0 \\ 0 & 0 & L \end{bmatrix} \begin{bmatrix} \frac{d}{dt} i_a \\ \frac{d}{dt} i_b \\ \frac{d}{dt} i_c \end{bmatrix} + \begin{bmatrix} e_a \\ e_b \\ e_c \end{bmatrix} \tag{2-3}$$

Phase voltages of the three-level inverter according to the switching position are given in the following equation:

$$\begin{bmatrix} V_a \\ V_b \\ V_c \end{bmatrix} = {}^{1}\!/_{6}\, V_{dc} \begin{bmatrix} 2 & -1 & -1 \\ -1 & 2 & -1 \\ -1 & -1 & 2 \end{bmatrix} \begin{bmatrix} S_a \\ S_b \\ S_c \end{bmatrix} \tag{2-4}$$

Where S_a, S_b and S_c are switch status as given in equation (2-2). When equation (2-4) is substituted into equation (2-3), the three-level inverter equivalent model is obtained as:

$$\begin{bmatrix} \frac{d}{dt} i_a \\ \frac{d}{dt} i_b \\ \frac{d}{dt} i_c \end{bmatrix} = \begin{bmatrix} -R/L & 0 & 0 \\ 0 & -R/L & 0 \\ 0 & 0 & -R/L \end{bmatrix} \begin{bmatrix} i_a \\ i_b \\ i_c \end{bmatrix} + \begin{bmatrix} \frac{V_{dc}}{6L}(3S_a - S') - \frac{e_a}{L} \\ \frac{V_{dc}}{6L}(3S_b - S') - \frac{e_b}{L} \\ \frac{V_{dc}}{6L}(3S_c - S') - \frac{e_c}{L} \end{bmatrix} \tag{2-5}$$

Where S' is expressed as:

$$S' = S_a + S_b + S_c \tag{2-6}$$

2.7 Three-level inverter switching control based M-SVPWM

The space vector modulation was originally developed by *Van der Broeck et al. (1988)* [116] as a vector approach to pulse width modulation (PWM) for three-phase VSI. The SVPWM is one of the preferred real-time modulation techniques and is widely used for digital control of rectifiers and inverters. For a given inverter (or rectifier) topology, there are a certain number of switching states. Each switching state produces a defined inverter output voltage, which can be represented by stationary voltage vectors in space. A collection of all the space vectors forms a space vector diagram. A reference voltage vector rotates in space within the space vector diagram. For a given position in space, three nearest stationary vectors can approximate the reference vector on which the gating signals for the switches in the inverter can be generated. Therefore, when the reference vector rotates in space for one revolution, the inverter output voltage changes one fundamental cycle. The magnitude of the inverter fundamental output voltage corresponds to length of the reference vector while its frequency corresponds to the rotating speed of the reference vector and vice versa.

The coming subsections present the general principles of the SVPWM, the way to determine the reference vector in the space vector diagram, dwell time calculation, switching state arrangement, and the simplification of the algorithm.

2.7.1 Basic principle

From Table 2-2 the three switching states $[P]$, $[O]$ and $[N]$ can represent the operation of the SVPWM technique. By taking the three phases into account, the inverter has a total of 27 possible switching states. There are 24 active vectors including 12 short vectors, 6 medium vectors and 6 long vectors, and the remaining are zero vectors (PPP, OOO, NNN), which lie at the center of the hexagon. The area of the hexagon is divided into six sectors (A to F) and each sector is divided to four regions (1 to 4) [117]. This result of total 24 regions can be sketched in the αβ plane as shown in Figure 2-11.

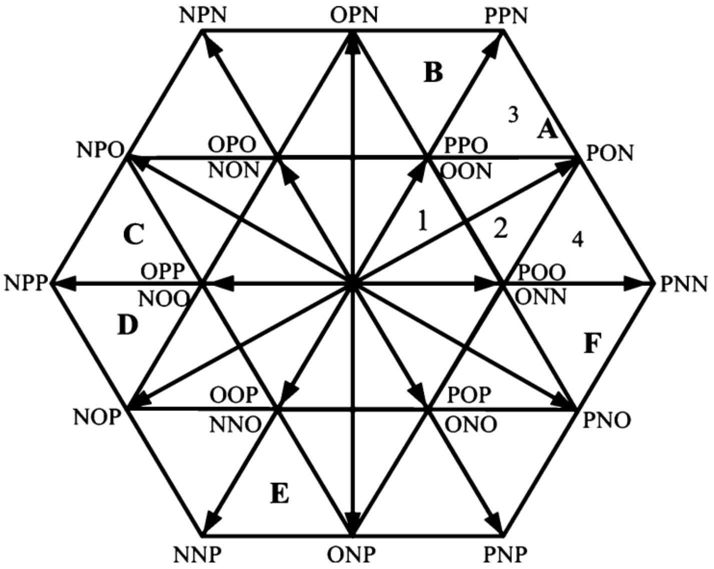

Figure 2-11 *Space-vector diagram of the three-level converter.*

The voltage vector can belongs to one of the following groups:

I. Zero vector $\overrightarrow{V_0}$, representing three switching states $[PPP]$, $[OOO]$ and $[NNN]$. The magnitude of $\overrightarrow{V_0}$is Zero.

II. Small vector ($\overrightarrow{V_1}$to $\overrightarrow{V_6}$), all having a magnitude of $Vdc/3$. Each small sector has two switching states called (redundant switches).

III. Medium vectors ($\overrightarrow{V_7}$ to $\overrightarrow{V_{12}}$), whose magnitude is $Vdc * (\frac{\sqrt{3}}{3})$.

IV. Large vectors ($\overrightarrow{V_{13}}$ to $\overrightarrow{V_{18}}$), all having a magnitude of $Vdc * (\frac{2}{3})$.

The following table summarizes all the switching states according to the relevant space vector:

Table 2-3 *The 27 switching states with their vector magnitude.*

Space Vector	Switching State	Vector Classification	Vector Magnitude
$\overrightarrow{V_0}$	[PPP], [OOO], [NNN]	Zero Vector	0
$\overrightarrow{V_1}$	[ONN], [POO]	Small Vector	$Vdc/3$
$\overrightarrow{V_2}$	[OON], [PPO]		
$\overrightarrow{V_3}$	[NON], [OPO]		
$\overrightarrow{V_4}$	[NOO], [OPP]		
$\overrightarrow{V_5}$	[NNO], [OOP]		
$\overrightarrow{V_6}$	[ONO], [POP]		

$\overrightarrow{\boldsymbol{V_7}}$	[PON]	Medium Vector	$Vdc*(\frac{\sqrt{3}}{3})$
$\overrightarrow{\boldsymbol{V_8}}$	[OPN]		
$\overrightarrow{\boldsymbol{V_9}}$	[NPO]		
$\overrightarrow{\boldsymbol{V_{10}}}$	[NOP]		
$\overrightarrow{\boldsymbol{V_{11}}}$	[ONP]		
$\overrightarrow{\boldsymbol{V_{12}}}$	[PNO]		
$\overrightarrow{\boldsymbol{V_{13}}}$	[PNN]	Large Vector	$Vdc*(\frac{2}{3})$
$\overrightarrow{\boldsymbol{V_{14}}}$	[PPN]		
$\overrightarrow{\boldsymbol{V_{15}}}$	[NPN]		
$\overrightarrow{\boldsymbol{V_{16}}}$	[NPP]		
$\overrightarrow{\boldsymbol{V_{17}}}$	[NNP]		
$\overrightarrow{\boldsymbol{V_{18}}}$	[PNP]		

Assuming the instantaneous voltage value of three-phase sine wave is expressed by:

$$\begin{aligned} V_a &= V_m * \sin(\omega t) \\ V_b &= V_m * \sin(\omega t - 2\pi/3) \\ V_c &= V_m * \sin(\omega t + 2\pi/3) \end{aligned} \tag{2-7}$$

The rotating vector can be expressed in αβ frame where its magnitude and angle are calculated using Clark's Transformation as follows:

$$\begin{bmatrix} V_\alpha \\ V_\beta \end{bmatrix} = 2/3 \begin{bmatrix} 1 & -1/2 & -1/2 \\ 0 & \sqrt{3}/2 & -\sqrt{3}/2 \end{bmatrix} \begin{bmatrix} V_a \\ V_b \\ V_c \end{bmatrix} \tag{2-8}$$

Hence:

$$\overrightarrow{V_{ref}} = V_\alpha + jV_\beta = {}^2\!/_3\,(V_a + aV_b + a^2 V_c) \tag{2-9}$$

Where $a = e^{j2\pi/3}$

$$\left|\overrightarrow{V_{ref}}\right| = \sqrt{{V_\alpha}^2 + {V_\beta}^2} \quad , \quad \theta = \tan^{-1}(V_\beta / V_\alpha) \tag{2-10}$$

2.7.2 Reference space-vector locating

The second stage in SVPWM technique is identifying sector and region in which the reference vector is laying. This can be done according to some sequential tests as explained below:

2.7.2.1 Sector identification

From equation (2-10), θ can be used to identify the sector to which V_{ref} belongs, hence:

If θ is between $0° \leq \theta < 60°$, then V_{ref} locates in Sector A.

If θ is between $60° \leq \theta < 120°$, then V_{ref} locates in Sector B.

If θ is between $120° \leq \theta < 180°$, then V_{ref} locates in Sector C.

If θ is between $180° \leq \theta < 240°$, then V_{ref} locates in Sector D.

If θ is between $240° \leq \theta < 300°$, then V_{ref} locates in Sector E.

If θ is between $300° \leq \theta < 360°$, then V_{ref} locates in Sector F.

2.7.2.2 Region identification

After sector allocating, another test should be done in order to identify precisely in which region the vector reference is located.

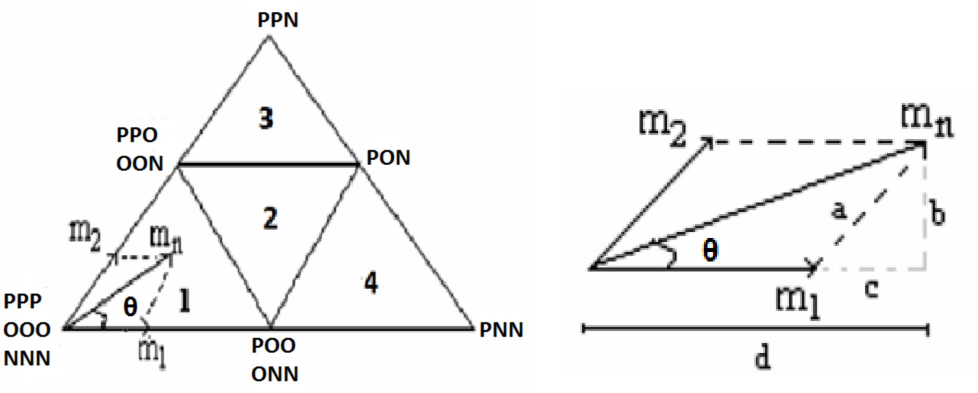

Figure 2-12 *Space vector diagram for m_1 and m_2 in Sector A.*

This sub-algorithm based on two parameters m_1 and m_2 as illustrated in Figure 2-12. These parameters are calculated as follows [118]:

$$a = m_2 = \frac{b}{\sin(\frac{\pi}{3})} = \frac{2}{\sqrt{3}}b = \frac{2}{\sqrt{3}}m_n \sin\theta \tag{2-11}$$

$$m_1 = m_n \cos\theta - (\frac{2}{\sqrt{3}}m_n \sin\theta)\cos(\pi/3) \tag{2-12}$$

$$m_1 = m_n(\cos\theta - \frac{\sin\theta}{\sqrt{3}}) \tag{2-13}$$

The concerned regions are located as follows:

If m_1, m_2 and $(m_1 + m_2) < 0.5$, then V_{ref} is in Region 1.

If $m_1 > 0.5$, then V_{ref} is in Region 4.

If $m_2 > 0.5$, then V_{ref} is in Region 3.

If m_1 and $m_2 < 0.5$ and $(m_1 + m_2) > 0.5$, then V_{ref} is in Region 2.

2.7.3 Dwell Times calculation

Sector A has been chosen to be our example for On-time calculation.

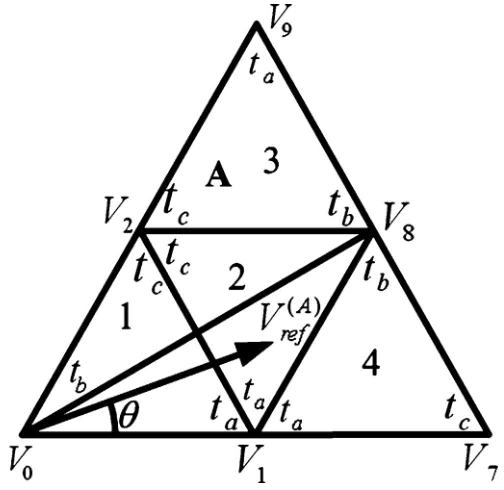

Figure 2-13 *Vector combination in sector A.*

Assuming V_{ref} is laying in region 2, at this moment V_{ref} can be represented by the three nearest vectors V_1, V_2 and V_8 as illustrated in Figure 2-13. During a sampling period T_s the equations of the on-time for voltage vectors can be expressed as:

$$\begin{cases} \vec{V}_{ref} T_s = \vec{V}_1 t_a + \vec{V}_8 t_b + \vec{V}_2 t_c \\ T_s = t_a + t_b + t_c \end{cases} \tag{2-14}$$

Therefor,

$$\begin{cases} t_a = T_s - 2K\sin(\theta) \\ t_b = 2K\sin(\frac{\pi}{3} + \theta) - T_s \\ t_c = T_s - 2K\sin(\frac{\pi}{3} - \theta) \end{cases} \tag{2-15}$$

Where: $K = (8/3)\, m_a\, T_s$

While, m_a is the modulation index and can be given by:

$$m_a = \sqrt{3}\frac{V_{ref}}{V_{dc}}, \quad \text{where } 0 \le m_a \le 1$$

Using the same procedure, the dwelling time in other regions in the same sector A can be calculated as shown in Table 2-4.

Table 2-4 *On-time in sector A.*

On time Region	t_a	t_b	t_c
1	$2\text{K}\sin(\frac{\pi}{3}-\theta)$	$\text{Ts}-2\text{K}\sin(\frac{\pi}{3}+\theta)$	$2\text{K}\sin(\theta)$
2	$\text{Ts}-2\text{K}\sin(\theta)$	$2\text{K}\sin(\frac{\pi}{3}+\theta)-Ts$	$\text{Ts}-2\text{K}\sin(\frac{\pi}{3}-\theta)$
3	$2\text{K}\sin(\theta)-Ts$	$2\text{K}\sin(\frac{\pi}{3}-\theta)$	$2\ \text{Ts}-2\text{K}\sin(\frac{\pi}{3}+\theta)$
4	$2\ \text{Ts}-2\text{K}\sin(\frac{\pi}{3}+\theta)$	$2\text{K}\sin(\theta)$	$2\text{K}\sin\left(\frac{\pi}{3}-\theta\right)-Ts$

2.7.4 Switching Sequence Arrangement

After calculating the On-time, the switching sequence has to be determined. Generally, two design criteria have to be satisfied during the switching sequence design in order to achieve the minimum device switching frequency:

1. The transition from one switching state to the next should involve only two switches, one being turned OFF and the other being turned ON.
2. The transition from one triangular region to the next should involve minimum number of switching.

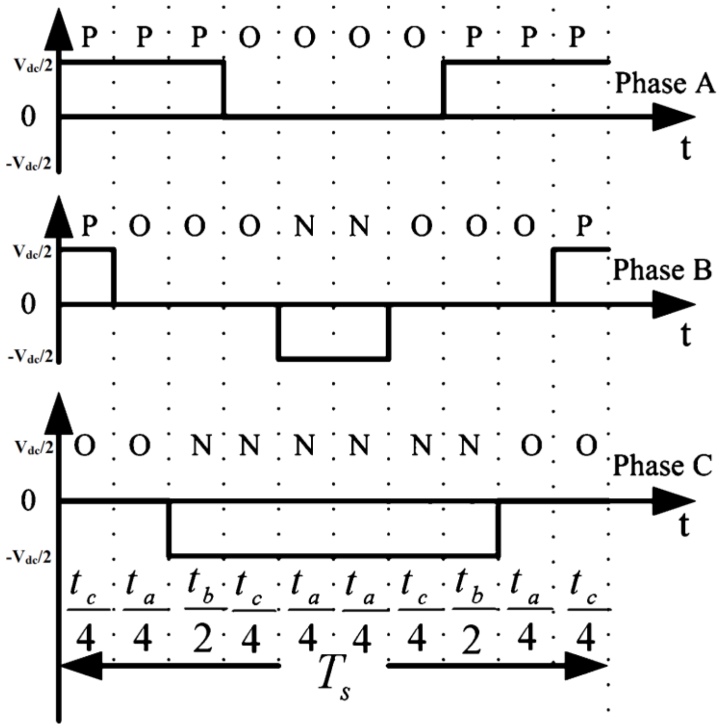

Figure 2-14 *Switching sequence arranged in a symmetrical pattern.*

As the inverter has some redundant switching states, the switching sequence are coordinated in order to fulfil low THD and ensure balanced DC-link voltages.

The switching sequences in the regions of sector A are arranged as follows:

Region 1: $PPO - POO - OOO - OON - ONN$ then return.
Region 2: $PPO - POO - PON - OON - ONN$ then return.
Region 3: $PPO - PPN - PON - OON$ then return.
Region 4: $POO - PON - PNN - ONN$ then return.

According to switching sequences arranged in symmetrical pattern, the PWM firing time setting for each switch in sector A can be achieved as given in Table 2-5.

Table 2-5 *PWM firing time setting for each switch of upper arms in sector A.*

Region / Time	1	2	3	4
PWM_S1a	$\frac{Tc}{4}+\frac{Ta}{4}$	$\frac{Tc}{4}+\frac{Ta}{4}+\frac{Tb}{2}$	$\frac{Ts}{2}-\frac{Tc}{4}$	$\frac{Ts}{2}-\frac{Ta}{4}$
PWM_S2a	$\frac{Ts}{2}$	$\frac{Ts}{2}$	$\frac{Ts}{2}$	$\frac{Ts}{2}$
PWM_S1b	$\frac{Tc}{4}$	$\frac{Tc}{4}$	$\frac{Tc}{4}+\frac{Ta}{2}$	0
PWM_S2b	$\frac{Ts}{2}-\frac{Ta}{4}$	$\frac{Ts}{2}-\frac{Ta}{4}$	$\frac{Ts}{2}$	$\frac{Ta}{4}+\frac{Tb}{2}$
PWM_S1c	0	0	0	0
PWM_S2c	$\frac{Ts}{2}-\frac{Ta}{4}-\frac{Tc}{4}$	$\frac{Tc}{4}+\frac{Ta}{4}$	$\frac{Tc}{4}$	$\frac{Ta}{4}$

2.7.5 Modified SVPWM algorithm

The main idea of the modified algorithm is exploiting the symmetrical geometry of the space vector diagram that is divided into six identical sectors as shown in Figure 2-11. Based on that fact, there is a close relationships for the On-time calculations and the switching in each phase, therefore, we can calculate the On-time for the switches in certain sector and then map the On-time in specific sector into the corresponding On-time in other sectors through this relationship. Figure 2-15 illustrates the deference of calculation flow between the conventional and the simplified algorithm for the three-level SVPWM.

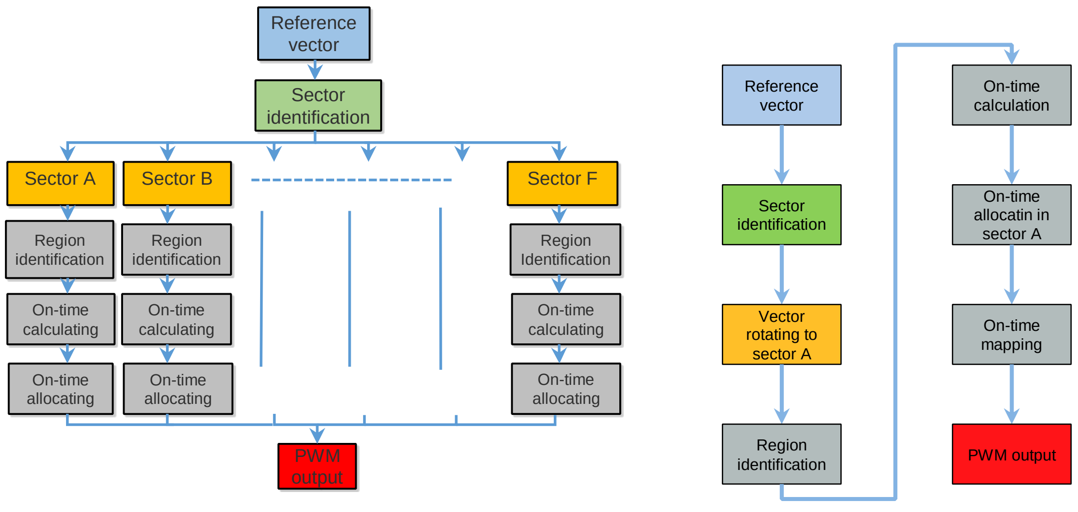

(a) (b)

Figure 2-15 *Computation flow for the three-level SVPWM (a) Conventional calculation (b) Simplified calculation.*

Assuming the reference vector $V_{ref}^{(A)}$ lays in region 2 of sector A, while reference vector $V_{ref}^{(B)}$ is obtained by rotating vector $V_{ref}^{(A)}$ counterclockwise by 60˚ as shown in Figure 2-16. As demonstrated in sub-section *2.7.3*, the reference vector $V_{ref}^{(A)}$ can be composed by vectors V_1, V_2 and V_8, whose On-times are computed using expression (2-14). Similarly, the reference vector $V_{ref}^{(B)}$ can be composed by vectors V_{10}, V_3 and V_2. By multiplying the rotating factor $e^{\frac{j\pi}{3}}$ at both sides of the dwell time for $V_{ref}^{(B)}$, the equation always can be referred to sector A. Consequently, whenever the reference vector lies is in the other sectors, it will be rotated to sector A by multiplication of $n\pi/3$ where $(n = 1, 2, 3, 4, 5)$.

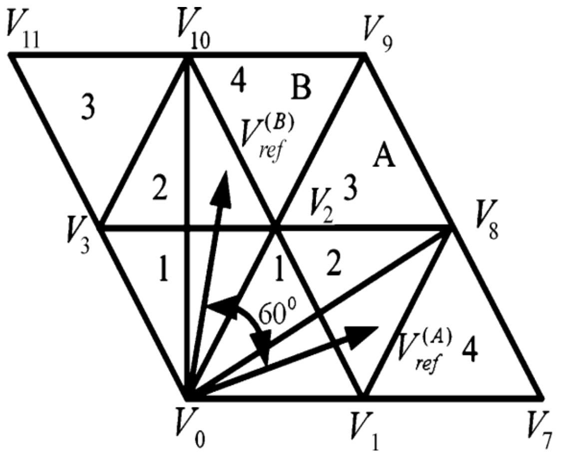

Figure 2-16 *Two vectors with 60º shifting in the sector A and B.*

Remembering from equation (2-9) the reference vector $V_{ref}^{(A)}$ is expressed as a combination of phase voltages V_a, V_b and V_c. Then, the reference vector $V_{ref}^{(B)}$ can be as follow:

$$\overrightarrow{V_{ref}^{(B)}} = \overrightarrow{V_{ref}^{(A)}} * e^{\frac{j\pi}{3}} = 2/3(-V_b + (-V_c)e^{\frac{j2\pi}{3}} + (-V_a)e^{\frac{-j2\pi}{3}}) \qquad (2\text{-}16)$$

Using the same way, the corresponding reference vector in other sectors can be structured as given in Table 2-6.

Table 2-6 *Relationships of voltages constructing the reference vectors in six sectors.*

Sectors	Phase voltage A	Phase voltage B	Phase voltage C
A	V_a	V_b	V_c
B	$-V_b$	$-V_c$	$-V_a$
C	V_c	V_a	V_b
D	$-V_a$	$-V_b$	$-V_c$
E	V_b	V_c	V_a
F	$-V_c$	$-V_a$	$-V_b$

2.8 Numerical simulation of three-level T-type inverter

The electrical power circuit of the three-level T-type inverter that corresponds to Figure 2-9 is carried out using Matlab/Simulink as shown in Figure 2-17. The proposed M-SVPWM algorithm is coded using M-File blocks whose code is written in Appendix A.

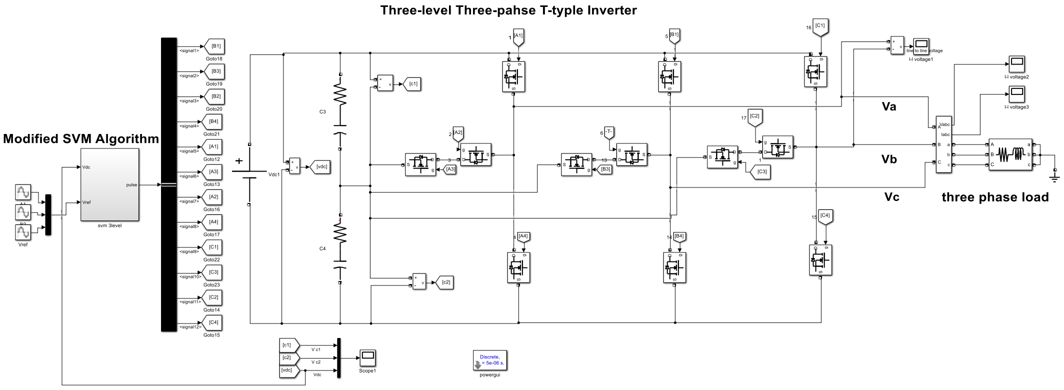

Figure 2-17 *Simulink diagram of the T-type inverter M-SVPWM control.*

With the same load and the same voltage rating as for the two-level inverter (12.5 kVA 380 $Vrms$ three-phase RL load at 0.8 power factor lagging) the comparison will take place.

The system is simulated for a modulation rate $m_a = 0.8$ and a switching period $T_s = 100 * 10^{-6}s$, which corresponds to a switching frequency $f_s = 1 / T_s = 10kHz$ and switching interval per period $n = 100$ intervals.

Figure 2-18 (a), (b) and (c) present the waveform of the voltage between phase and neutral of the source V_{ao}, the voltage between phases V_{ab}, and the voltage between phase and neutral of the load V_a, respectively. It is noticed that the voltage V_{ao} has three voltage levels, V_{ab} has five levels, and V_a has nine levels. The voltage V_a envelops the reference V_a^*, so that the fundamental V_a of coincides with V_a^*.

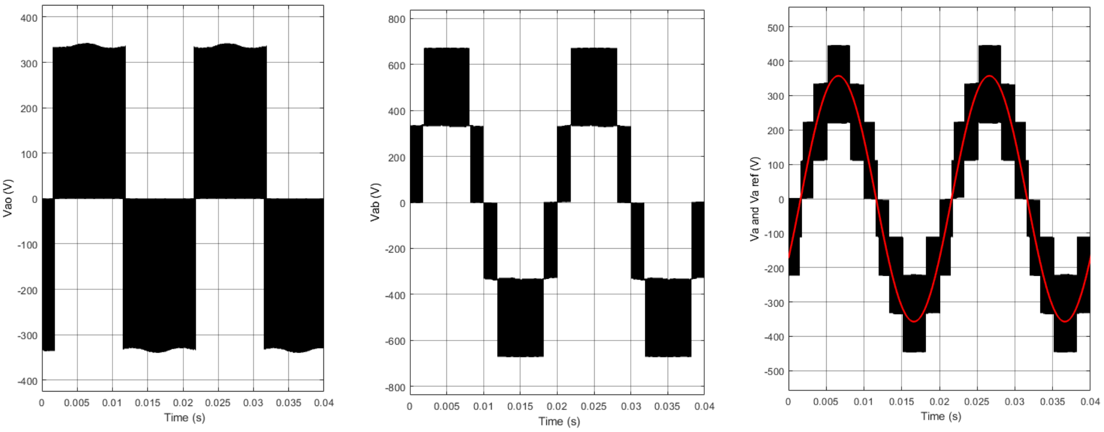

(a) (b) (c)

Figure 2-18 *(a) Phase-neutral source voltage, (b) Phase-to-phase voltage, (c) Phase-to-ground load voltage (*$\boldsymbol{m_a = 0.8}$*,* $\boldsymbol{f_s = 10kHz}$*).*

Figure 2-19 shows also the trajectory of the reference voltage vector V_a^* for different modulation rates in the αβ plan of the SVM hexagon that formed by the output states of the three-level inverter. It is clearly shown that for $m_a = 0.8$ and $m_a = 0.6$, the locus of the reference vector is located in the external hexagonal sector of the vector diagram. For $m_a = 0.4$ and $m_a = 0.2$, the locus of this reference vector is located in the internal hexagonal sector of the vector diagram. In the latter cases, the three-level inverter plays the two-level inverter.

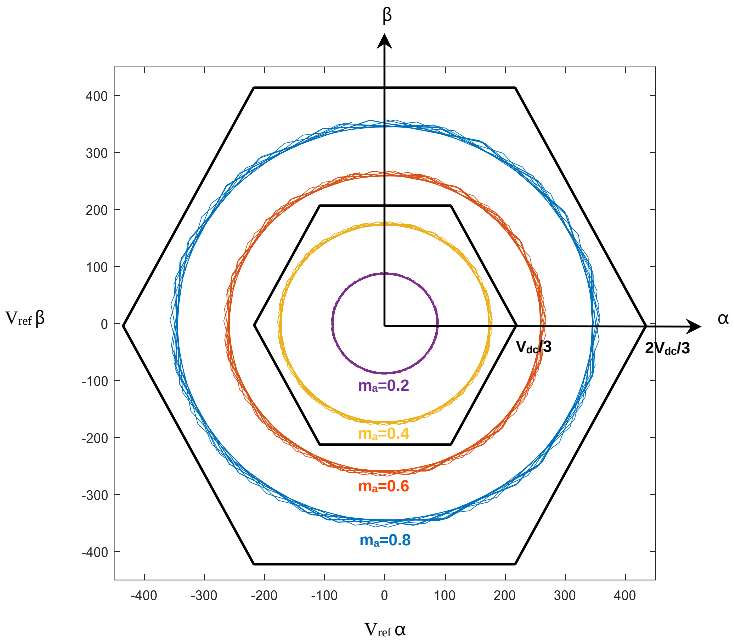

Figure 2-19 *Voltage reference $\boldsymbol{V_a^*}$ in αβ plan for different modulation index.*

Figure 2-20 (A), (B) demonstrates respectively the sectors and regions where the voltage vector reference is located during On-time calculation process, while the normalized On-times for switches S_{a1}, S_{b1}, and S_{c1} with modulation index ($m_a = 0.8$) are exported to the same graph axes as given in Figure 2-20 (C). To generate gating signal for driving output voltage of the inverter, the three phase shifted On-time reference waves are compared with one triangular wave having a carrier frequency ($f_s = 10kHz$).

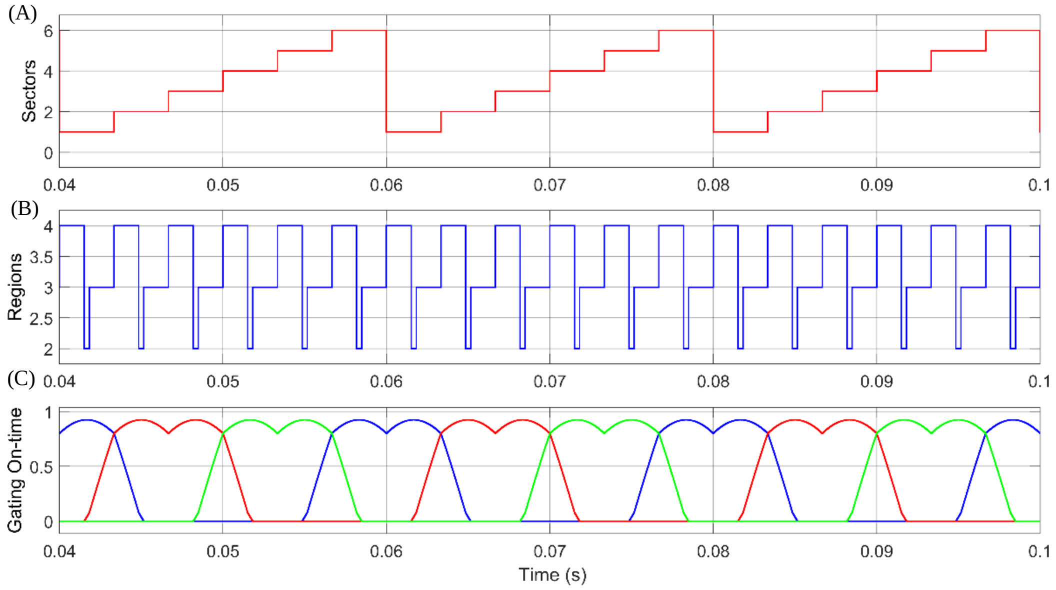

Figure 2-20 *(A) Selected sector according to V_{ref} location; (B) selected region in each sector; (C) normalized on-time for switches $\boldsymbol{S_{a1}}$, $\boldsymbol{S_{b1}}$, and $\boldsymbol{S_{c1}}$ in the upper arms of phases a, b, and c, respectively, with ($\boldsymbol{m_a = 0.8}$).*

Figure 2-21 shows the output voltage and its harmonic spectrum for different values of the modulation index. It can be seen that the harmonics are centred around the multiples of the sampling frequency. Figure 2-22 shows the variation of the amplitude of the fundamental and the THD as a function of the modulation. Note that the THD is inversely proportional, while the amplitude of the fundamental is proportional with the modulation index. Figure 2-23 shows the output voltage and its spectrum of harmonics for different values of the switching frequency, while Figure 2-24 shows the evolution of the amplitude of the fundamental of the output, and of its harmonic rate with respect to the switching interval. The amplitude of the fundamental is practically insensitive to the variation of the switching frequency, while the THD decreases with the increase of this frequency. By comparing with the case of the two-level inverter, it can be seen that for the same modulation index rate or the switching frequency, the THD of the output of the three-level inverter is much lower.

Furthermore, a comparative analysis is highlighted, always in terms of THD, but this time between the conventional SPWM and the proposed M-SVPWM. Both modulation techniques are tested in the same inverter (T-type three-level inverter) and for the same modulation index and switching frequency ($m_a = 0.8, f_s = 10\ kHz$). FFT analysis of the output line voltage of the both techniques are shown in Figure 2-25.

The THD value of the output voltage of the inverter which is controlled by SPWM is 37.05%, while for the M-SVPWM is 28.05%. In addition, the highest possible peak phase fundamental is very less in sine triangle PWM when compared with space vector PWM.

Therefore, SVPWM technique has been found to be a more efficient switching method especially in terms of power quality.

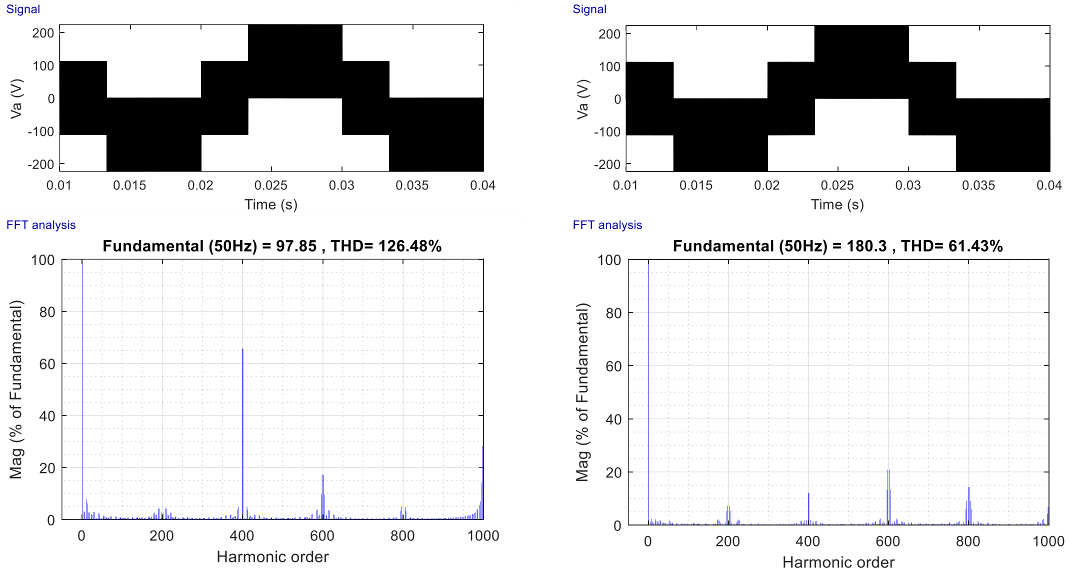

$m_a = 0.2$ $m_a = 0.4$

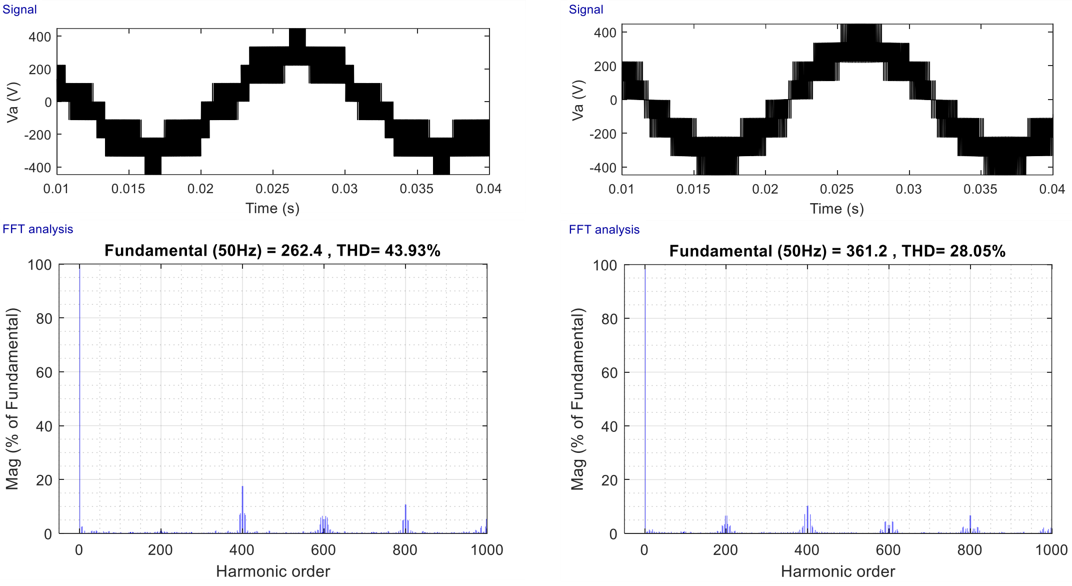

$m_a = 0.6$ $m_a = 0.8$

Figure 2-21 *Harmonic analysis of the load phase volatge with different modulation index.*

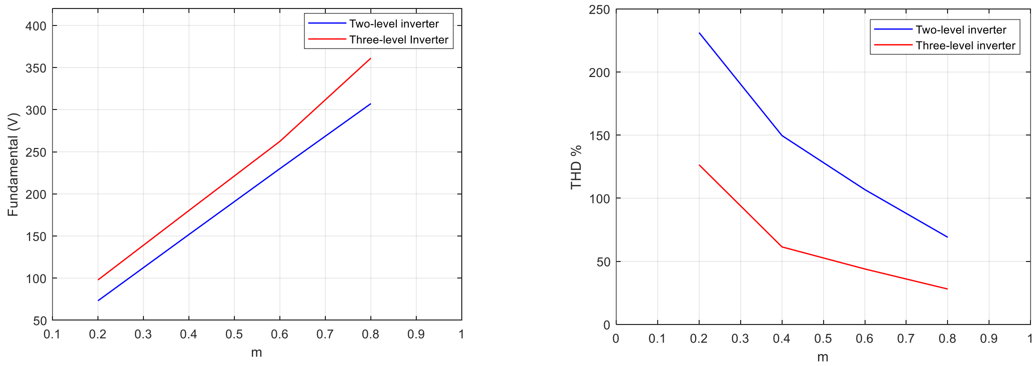

Figure 2-22 *The evolution of the voltage fundamental and THD with respect to the modulation index.*

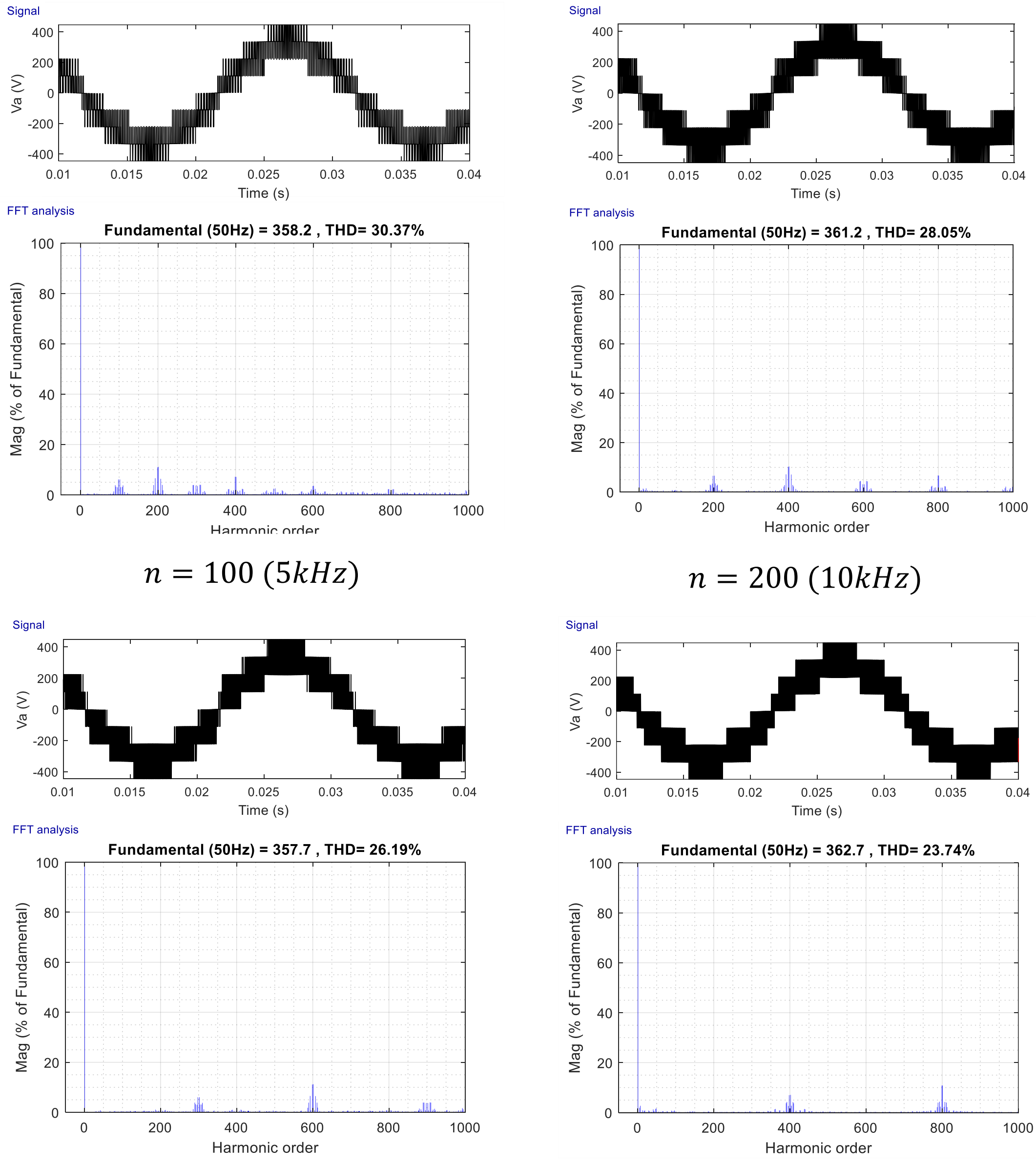

$n = 100\ (5kHz)$ $n = 200\ (10kHz)$

$n = 300\ (15kHz)$ $n = 400\ (20kHz)$

Figure 2-23 *Harmonic analysis of the load phase volatge with different switching frequency.*

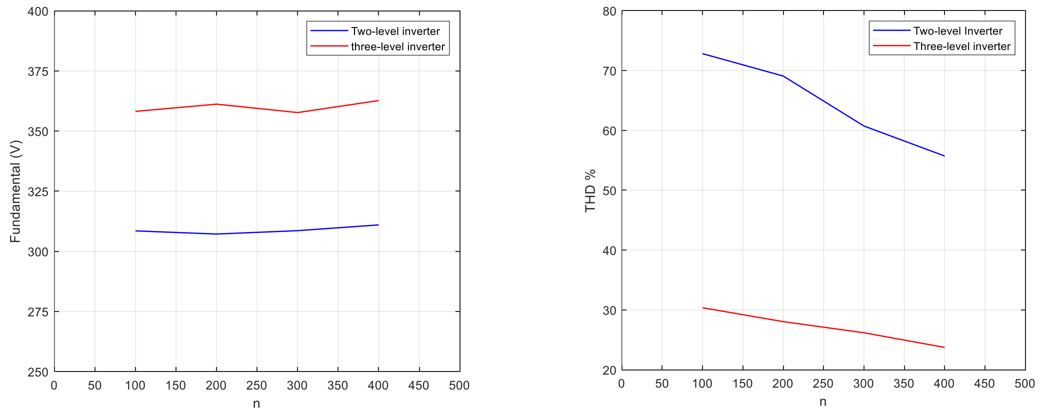

Figure 2-24 *The evolution of the voltage fundamental and THD with respect to the switching interval.*

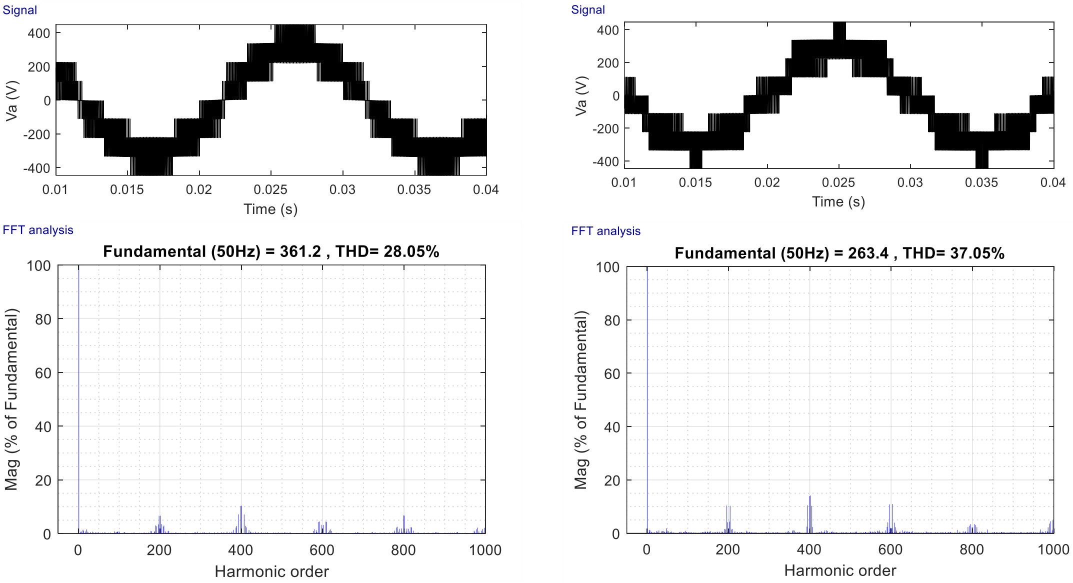

(a)

(b)

Figure 2-25 *FFT analysis of the output voltage waveform of the three-level T-type inverter (a) with M-SVPWM switch control (b) with SPWM switch control.*

2.9 Experimental validation using cost-effective STM32F4 board

In practice, generally the switching control for a three-level inverter is implemented using software based on DSP card [119]or Dspace platform [120][121] that are fast processors. However, they increase the overall system's cost. As an alternative proposition, our work investigates a very economic microcontroller whose computation capabilities are almost similar to those expensive boards. This low-cost Microcontroller, *STM32F407*, is based on the high-performance *ARM Cortex-M4 32-bit RISC* core operating at a *210 DMIPS*. The *Cortex-M4* core features a *Floating Point Unit (FPU)* single precision that supports all *ARM* single precision data-processing instructions and data types. It implements a full set of DSP instructions and a memory protection unit (*MPU*). Moreover, it incorporates high-speed embedded memories and an extensive range of enhanced I/Os and peripherals. Some of the latter are dedicated to power electronics converters and electrical machines control such as *ADCs, DACs, PWMs* outputs and Encoders inputs [122].

2.9.1 Introduction to STM32F407 Discovery board

The *STM32F4 DISCOVERY* board (Figure 2-26) is a low-cost and easy-to-use development kit to quickly evaluate and start a development with an *STM32F407VG* high-performance microcontroller. The *STM32F4* Discovery kit allows users to easily develop applications with the *STM32F407VG* high performance microcontroller with the *ARM® Cortex®-M4 32-bit core*. Based on *STM32F407VG*, it includes an *ST-LINK/V2* or *ST-LINK/V2-A* embedded debug tool, two *ST-MEMS* digital accelerometers, a digital microphone, one audio *DAC* with integrated class *D* speaker driver, *LEDs*, push buttons and a *USB OTG micro-AB* connector. To expand the functionality of the *STM32F4* Discovery kit with the Ethernet connectivity, *LCD* display and more.

The *STM32F4* Discovery kit comes with the *STM32* comprehensive free software libraries and examples available with the *STM32Cube package* [123].

Figure 2-26 *STM32F407 DISCOVERY board.*

2.9.1.1 Interfacing STM32F4 Board with MATLAB

Using the embedded coder target for *STM32F4* and other functioning tools together with the Keil, real time implementation of the sophisticated Simulink model can be developed and easily uploaded into the board processor.

Design a Simulink model includes an embedded target blocks as per requirements of application and availability. The main directory path is located properly in command window of MATLAB before structuring any Simulink model file. The Support package for *STMicroelectronics STM32F4* discovery board allows the user to create and run Simulink models on a discovery kit. Support package includes a library of Simulink blocks for configuring and accessing board peripherals.

Thanks to the *Waijung software* that represents the third-party interface for *STM32F4* blocks along with MATLAB [124]. In order to complete *Waijung* block installation process, user has to install STM link utility driver and select the parameter setting for target setup as per requirement.

2.9.2 M-SVPWM pulses generation

The experimental results can be obtained starting by uploading the proposed M-SVPWM method in the STM32F4 board. The source code of the proposed algorithm has been coded in MATLAB Function blocks Figure 2-27. The code was compiled and uploaded on the card to get the desired switching patterns at the output pins. It generates three $50\ Hz$ sinusoidal references with 120^o phase shift, selects the voltage sector and computes all switching duty cycles based on the proposed algorithm, then it configures six PWM generators to work at $10\ kHz$.

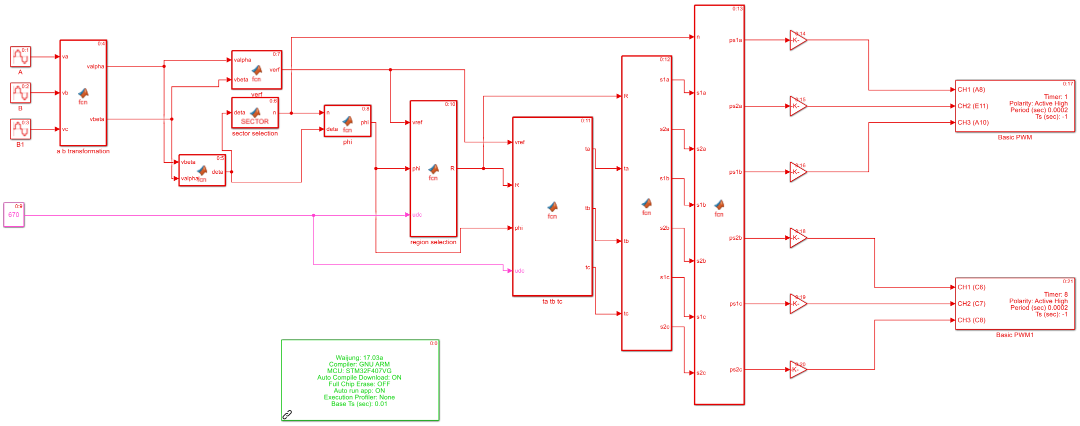

Figure 2-27 *Embedded simulated model of M-SVPWM Technique using Waijung Software.*

Due to the high switching frequency the simultaneous conduction of the four switches may occur, hence short circuit. In order to avoid this problem a delay time or (dead-time) should be implemented. STM32F4 board provide the complimentary switches with flexibility of choosing the appropriate dead time through "*Advanced PWM*" block. Figure 2-28 demonstrates the dead time between the two complementary signals, in the first leg for the switches S_{a1} and S_{a3}. In this case, a $3\mu s$ has been set for the dead time.

Figure 2-29 (a) channel 2 (red signal) illustrates the gate signal generated from the digital output pin *A8* that drives the first power switch of the first leg (S_{a1}), whereas channel 1 (blue signal) shows the fundamental component of the signals after passing through a low pass filter with $R = 3.3\ k\Omega$ in parallel with $100\ nF$. It is clear that the fundamental component is a positive sine wave that has an injected triple harmonic that proves the SVPWM operation.

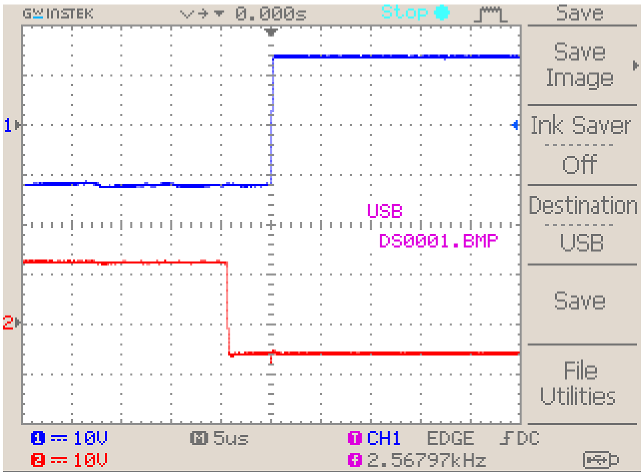

Figure 2-28 *Generating dead time between the two switches S_{a1} and S_{a3}.*

In order to show the control phase displacement between the first leg (a) and second leg (b), the switching signals for the first power switch of the first leg (S_{a1}) and first power switch of the second leg (S_{b1}) are filtered and compared as displayed in Figure 2-29 (b).

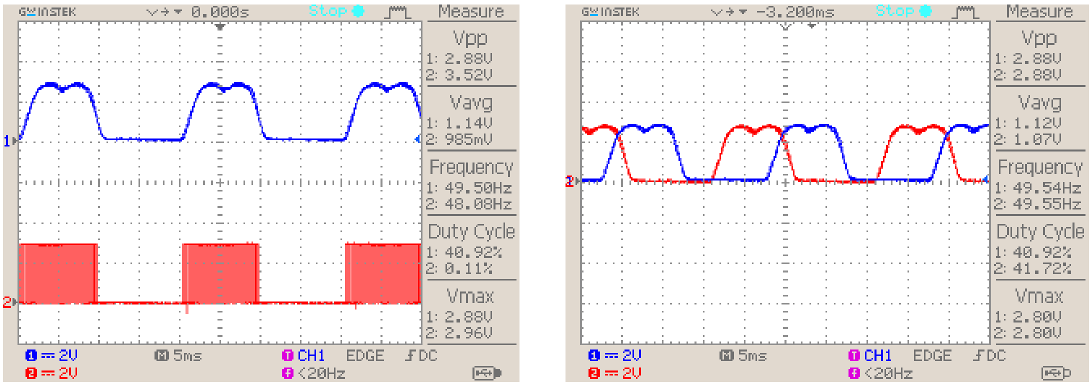

(a) (b)

Figure 2-29 *(a) 10 kHz gate signal generated by a TMS320F4 board using the M-SVM technique, without filtering (CH2, below) using Low Pass Filter (CH1, above). (b) The difference between two gate signals (S_{a1}) and (S_{b1}) with phase shift of 120^o.*

2.9.3 Hardware implementation and results

In order to investigate the validity of the proposed M-SVPWM algorithm, a complete prototype of three-phase three-level T-type is built from scratch. As the first step, only one leg of the inverter was implemented in a breadboard to perform the test (Figure 2-30 (a)) [125]. After the validation, the three legs were printed in PCBs and connected in T-type inverter form (Figure 2-30 (b)) [126].

As the signal obtained from the STM32F4 board is weak in amplitude, a Gate Switching Circuit should be implemented as interface between the low power circuit and the high power circuit. This circuit is basically made up of Buffers and Optocouplers. The main role of this circuit is to isolate the drive circuit from the power circuit and amplify the control signals. The bill of material to implement the inverter is stated in Appendix E.

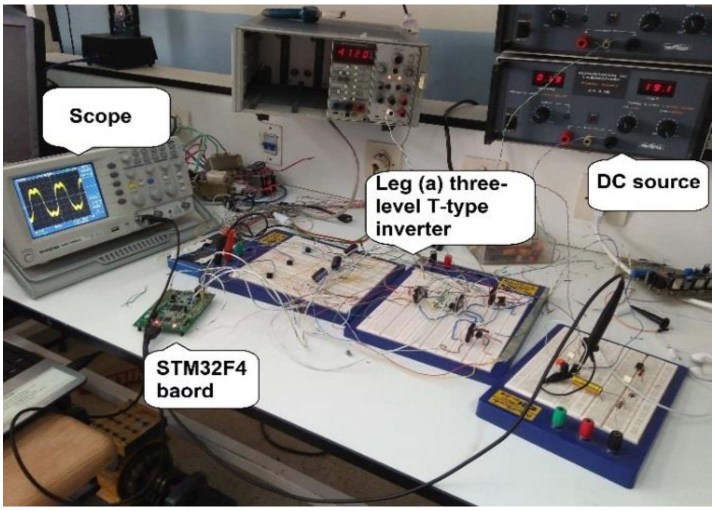

(a)

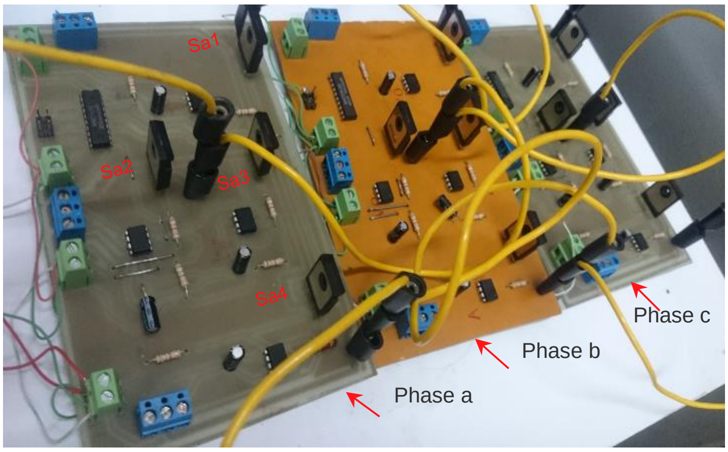

(b)

Figure 2-30 *The experimental power circuit of three-level T-type inverter (a) Prototype test of one leg three-level T-type inverter (b) the complete three-phase PCB designed three-level T-type inverter.*

Figure 2-31 (a) and (b) demonstrate respectively the phase-to-neutral (V_{ao}) and phase-to-phase (V_{ab}) output voltages. The results reflect the three-level nature of this inverter, where the phase to neutral voltage has two levels $V_{dc}/2$ and 0, while phase-to-phase voltage has three levels 0, $V_{dc}/2$ and V_{dc}, as explained previously.

In order to see the fundamental component of the voltage signals, a low pass filter is implemented in the output of the inverter with $R = 30\ k\Omega$ in parallel with capacitor of $100\ nF$. The fundamental of the phase-to-neutral (V_{ao}) and phase-to-phase (V_{ab})

waveforms are shown in Figure 2-31 (c) and (d) respectively. It can be noticed from the figure (c) that the fundamental component of the phase-to-neutral voltage is not uniform sine wave but has injected triple harmonic due to SVPWM operation without affecting on the phase-to-phase output voltage.

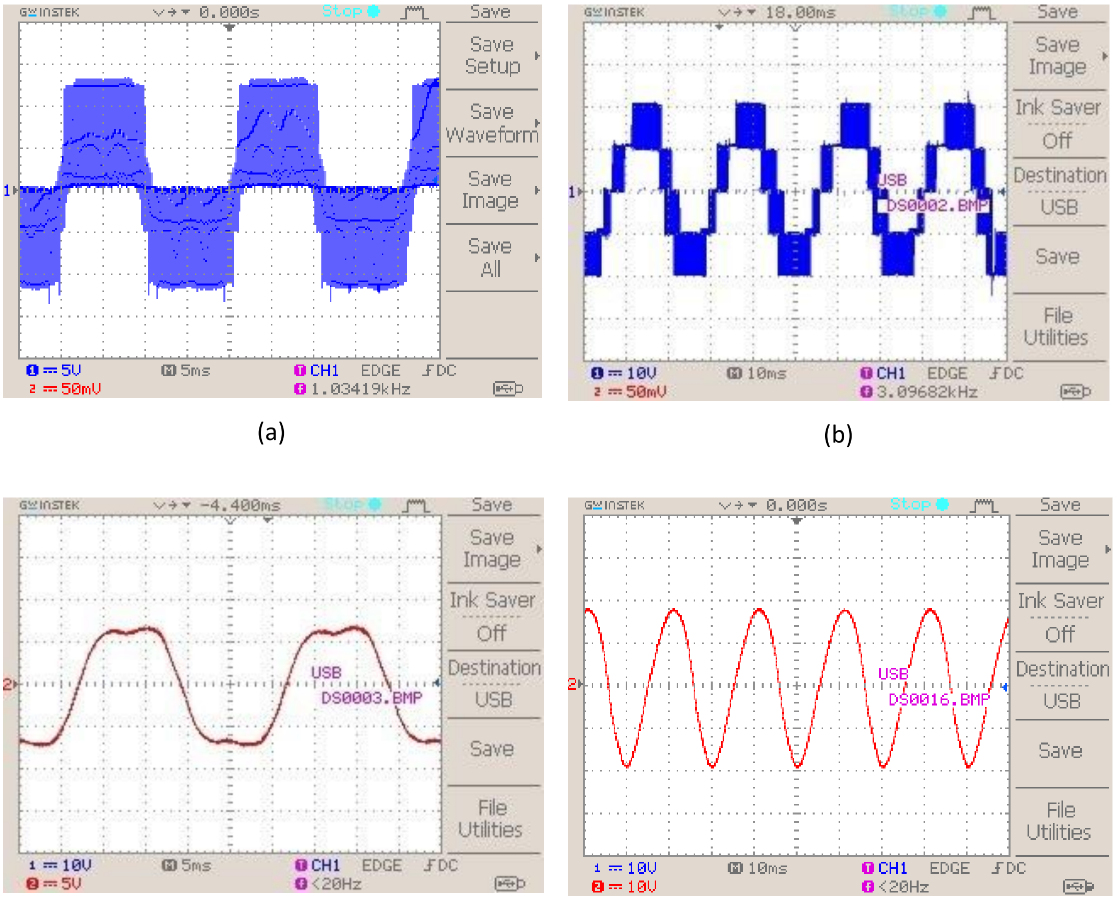

(a) (b)

(c) (d)

Figure 2-31 *(a) Phase-to-neutral voltage ($\boldsymbol{V_{ao}}$) (b) phase-to-phase voltage ($\boldsymbol{V_{ab}}$) (c) fundamental waveform of the phase-to-neutral voltage (d) fundamental waveform of the phase-to-phase voltage.*

2.10 Conclusion

This chapter provides a comprehensive analysis on the three-level T-type inverter M-SVPWM controlled. A number of issues were investigated, including the inverter configuration, operating principle, Modified Space Vector Modulation (M-SVM) technique, and comparative analysis with conventional two-level inverter. The use of three-level inverters reduces the harmonic components of the output voltage compared with the two-level inverter at the same switching frequency and the same modulation index, which make it the more suitable for high-voltage power systems offering a better power quality.

At the end of this chapter, the experimental validation of the proposed three-phase three-level T-type voltage source inverter M-SVPWM controlled has been provided. In addition, some key design considerations are given to improve the flexibility of usage. In the hardware implementation, embedded MATLAB simulation of SVPWM technique is carried out and interfacing embedded MATLAB Simulink model with STM320F4 board has been done using Waijung software, then it is successfully tested with the proposed inverter. This board can serve as a processor to minimize cost of the computational intensive task in comparison with advanced processors such as Dspace or DSP. The obtained results show the effectiveness and capability of using STM32F4 board in controlling such as an advanced converter like T-type three-level inverter.

Chapter 3: Control Strategy of Multi-functional Inverter based PI-like Fuzzy Logic Control

3.1 Introduction

In recent years, significant research has been carried out on control strategies for three-phase VSC-PWM converters. Most applications of VSC-PWM have a control structure comprising an internal *current feedback loop*. Thus, the performance of the converter system depends directly on the performance of the applied current control strategy. Therefore, the current control of VSC-PWM is one of the hottest topics of modern power electronics. The main task of the current control VSC-PWM scheme is to force the output three-phase ac currents of the converter to follow the reference signals. In our work, the reference current is generated to satisfy the multi-functional inverter application. The multi-functionality here will be represented in the following tasks: Power conversion, maximum power extraction from PV source, harmonic mitigation, and reactive power compensation. Therefore, the control system must be hierarchical and subsequently composed of subsystems (MPPT controller, Harmonics current identification, and synchronous current controller-based PI-Like Fuzzy Logic Control).

In this chapter, a literature review about different control strategies of a multi-functional inverter is firstly highlighted, and then each part of the control system will be discussed and analyzed in detail. Lastly, a particular focus will be given to the main contribution of our control part, which is the proposed PI-like FLC, where a new approach of setting the scaling factors which considerably affect the system's response is proposed. Furthermore, a methodology to properly set the fuzzy rules is suggested.

3.2 Control strategies for Multi-functional inverter (State-of-art)

An inverter control system aims to maintain the AC output current and its frequency at a desired level with minimum THD [127]. This role is played by the controller using an appropriate control strategy that maintains the current at a specific reference input or set-point. With proper control strategy design, the harmonic content of the output voltage and current can be reduced [128]. The duty cycle of switching power devices is one of the control parameters of power converters. The duty cycle is controlled to allow the inverter output current to follow the reference current signal. Tracking accuracy generally depends on the capability of the controller in the control system. Figure 3-1 depicts the general concept of an inverter closed-loop control system.

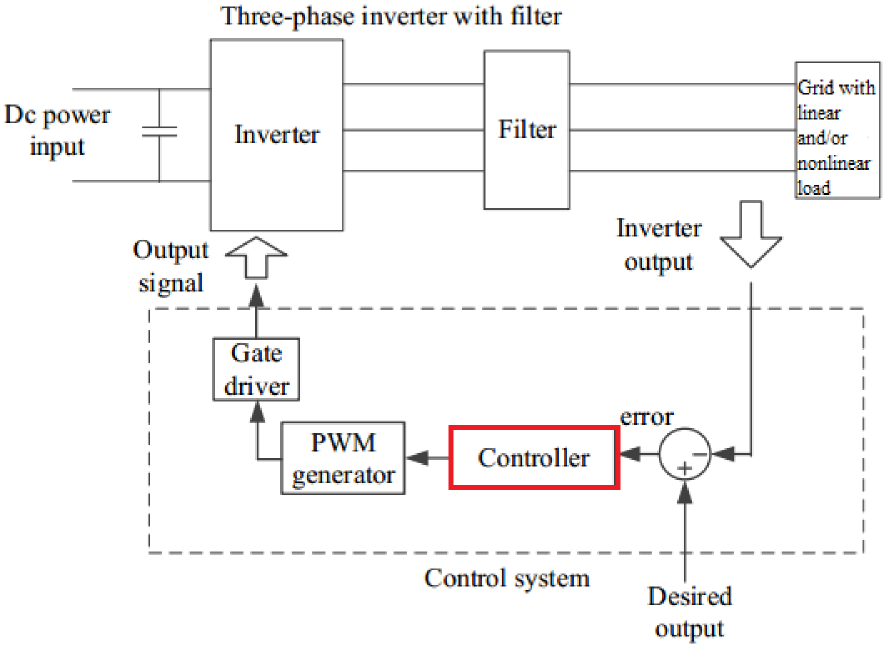

Figure 3-1 *Geneal schematic of closed-loop control system of grid-connected inverter.*

Based on the concept of the control system, both the inverter and the output filter are the main components to be controlled where the feedback control-loop always taken from the output of the filter. As we are controlling the output current, the output waveform of the filter is transmitted to the input of the control system by a sensors. Depending on the input requirement (measured signal) of the control system, different types of sensors (e.g, voltage sensors and current sensors) are used. The control algorithm is designed based on the property of the control system input signal so that the plant output matches the desired reference. The generated error between the reference signal and the measured one will be processed using an appropriate controller. An output control signal is then sent to the actuator (e.g. PWM), to determine adequate pulsation of the inverter's power switches.

Different conventional controller techniques such as proportional-integral-derivative (PID), proportional-integral (PI) [129][130], proportional resonant (PR) [131], and hysteresis are mostly used specially in the real-world for the sake of simplicity and their ease of implementation. However, those control techniques suffer from many drawbacks. The conventional PI/PID controllers with the fixed gains have to be set with a high bandwidth in order to guarantee a correct tracking of the reference variations, this will push the system to its stability limits [132]. In addition, the controllers offer a poor transient response when the system is subjected to any kind of variation. The PR controller can offer a zero steady-state error and provide high gain at the resonant frequency compared to the PI/PID controllers. However, its performance is constrained by the system's bandwidth. Likewise, the hysteresis controller has some advantages such as simplicity and robustness. Nevertheless, due to its non-constant switching frequency, it generates high current ripples and causes a high switching loss; consequently, bulky output filter is required [133].

Due to the increase of system's complexity and large integration of non-linear elements, the non-adaptive conventional controllers lead the researchers to change the pattern of the controllers with evolutionary intelligent techniques such as fuzzy logic, neuro-fuzzy, neural network, genetic algorithm, etc. [134]. Compared to the conventional linear controllers, these intelligent controller design doesn't require the exact mathematical model of the system, along with their ability to handle the nonlinearities.

Fuzzy logic control (FLC) is considered as one of the simplest intelligent and adaptive control techniques for controlling a grid-interactive multi-functional inverter as it can show a better performance in terms of response time, settling time, and robustness against parameter uncertainties and load variations [135].

In *Hasanien H. M. et al.* [136] used a fuzzy logic control to improve the power injection of VSC interfaced disribution generation (DG). Two fuzzy controllers of Mamdani type have been used to control the active and reactive power of the converter. A time-domain simulation in conjunction with a black-box optimization tool have been used to set only the parameters of the fuzzy sets. The remaining FLC parameters have been selected using the Trial-and-error method. However, the obtained results showed that the overshoot of the power and voltage of fuzzy control are slightly better than those obtained by conventional controllers. References like [137] and [138] present the development of fuzzy-based inverter controller for grid-connection photovoltaic application. others like [76] and [75] the fuzzy logic control is incorporated to regulate the DC-linke voltage and balance the voltage across the capacitors in active power filter (APF) application. In *Vigneysh T. et al.*[100] used a fuzzy system to adapt the conventional PI controllers' parameters of grid-connected APF in order to improve the system performance. The obtained results showed that the overshoot of the power and current responses are smoother in comparison with conventional controllers. However, multi-functional of the grid-connected converter has not been shown.

The findings indicate that FLC have attracted attention in the field of power control engineering, particularly in the design of inverter controllers for PV applications and generation. The FLC is also auditable for completeness, redundancy, and consistency. However, finding the bounderies of membership functions, scaling factors, and FLC rules requires manual tuning, long computation time and considerable effort.

In our work, a new analogy based on the conventional *PI* controller is used to define easily the fuzzy controller gains (Scaling Facotrs), resulting therefore in a simple and preferment FLC controller. Furthermore, in order to refine the fuzzy output decision, the rule base is inspired by the phase plane trajectory of a closed-loop system. The proposed PI-FLC will be used to design both the DC-voltage regulation and the current controllers in this study.

3.3 Multi-functional inverter for single-stage grid-tied PV system configuration

Figure 3-2 shows the circuit diagram of the proposed system that represents a single-stage three-phase three-level T-type inverter for the grid-connection PV system with APF capability. The PV array consists of 126 panels of *Solar World SW220* being connected as 21 series modules in 6 parallel strings. Subsequently, the array can provide up to $27.72\ kW$. This maximum power is generated at $613\ V$ of nominal DC voltage and DC current of $45.18\ A$ which correspond to *Standard Test Condition* STC (irradiation of $1\ kW/m^2$ and temperature of $25\ C^0$). The PV array is connected to the grid through DC-link capacitors, inverter, and finally an inductor. The DC link capacitors are used to reduce the DC voltage fluctuations while inductors allow smoothing AC current ripples; selection of their values mainly depends on the desired voltage and current ripples. The computation methodology of these two parameters is reported in Appendix C. The heart of the system that is a T-type three-level inverter is dedicated to extract the maximum power from the PV array, convert it to a three-phase AC power, and act simultaneously as an active filter to eliminate harmonic injection into and/or from the grid. To prove the effectiveness of the last task, a non-linear load is connected to the *PCC*.

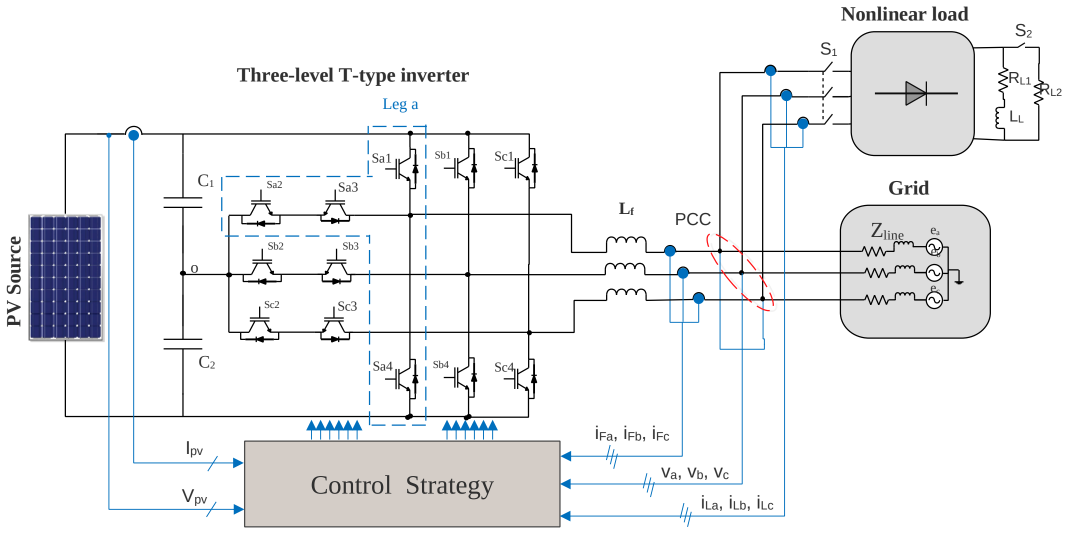

Figure 3-2 *Power circuit diagram for multi-functional inverter for single-stage grid-tied PV system.*

3.4 The proposed control strategy

As mentioned in the previous section, in a single-stage architecture, there is only one devise that must be controlled that is the multi-functional inverter. The control signals to this inverter must fulfil the requirements of all the functions: power converting, maximum power tracking, DC-link voltage regulation, active and reactive power control, harmonic elimination, and reactive power compensation. Therefore, the control system must be hierarchical and subsequently composed of subsystems as depicted in Figure 3-3, each subsystem of the proposed control will be analysed in details in the coming sub-sections.

In order to perform the multi-functional requirements, the inverter control requires as inputs: the PV array voltage and current (V_{pv}, I_{pv}), *PCC* voltages (v_a, v_b, v_c), AC side inverter currents (i_{Fa}, i_{Fb}, i_{Fc}), and the nonlinear load currents (i_{La}, i_{Lb}, i_{Lc}). While the output of the control block represents the switching signals whose duty cycles are calculated using the modified SVPWM technique.

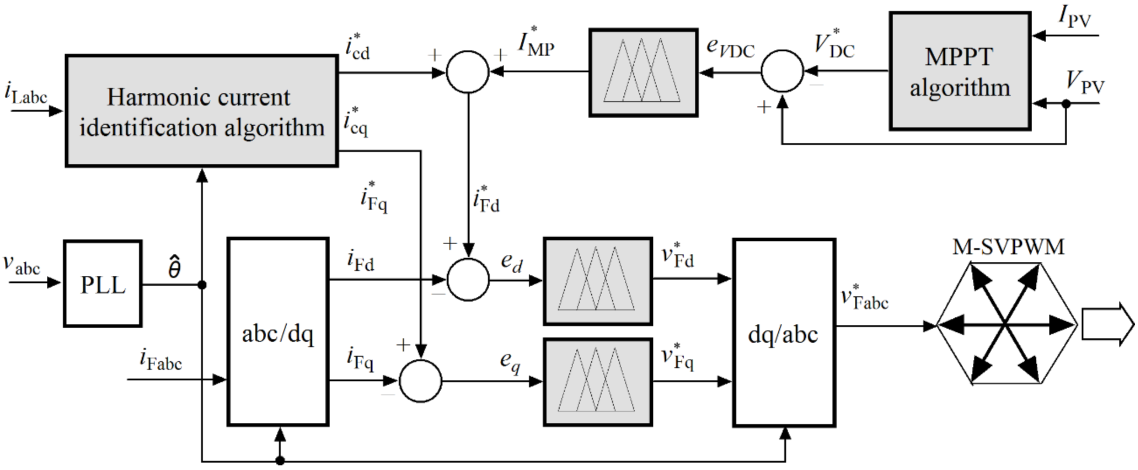

Figure 3-3 Control block diagram of the proposed Multi-functional inverter.

3.5 Incremental conductance MPPT Controller

In our study, the incremental conductance (IncCond) method is selected to harvest the maximum power from the PV generator. The IncCond can provide a fast tracking under changing in the climate conditions with higher accuracy than the conventional P&O [139].

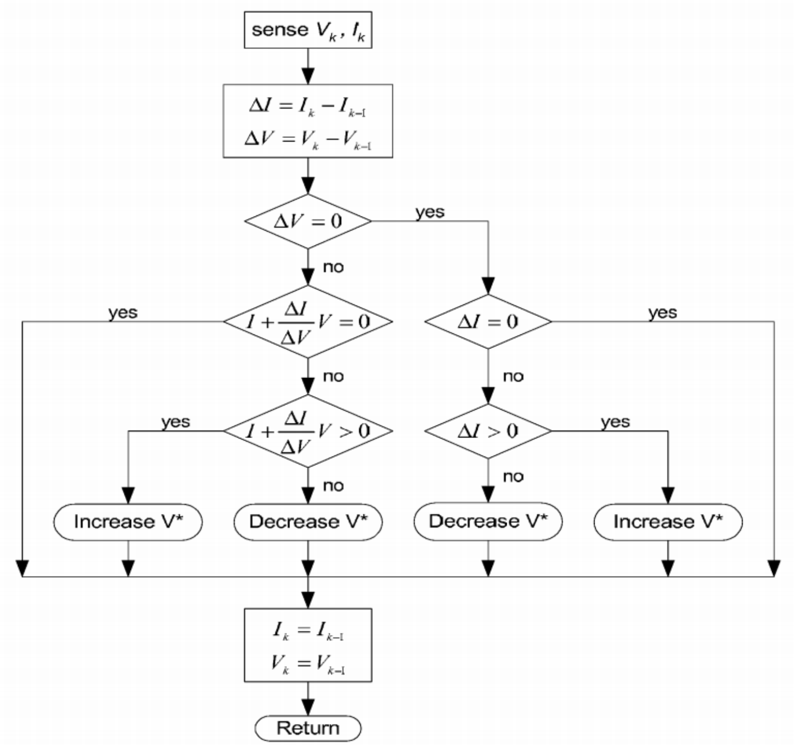

Figure 3-4 Flowchart of the incremental conductance for MPPT algorithm.

The flowchart of the IncCond algorithm is shown in Figure 3-4, where V_k and I_k are the actual voltage and current of the PV generator while V_{k-1}, I_{k-1} are the previous sampled voltage and current, respectively. Assuming the target variable is the output voltage of the PV array.

According to the P-V curve characteristic of the PV array, we find:

$$\begin{gathered}\frac{dP}{dV}=0 \rightarrow at\ MPP\ , \\ \frac{dP}{dV}>0 \rightarrow left\ side\ of\ MPP\ , \\ \frac{dP}{dV}<0 \rightarrow right\ side\ of\ MPP\ . \end{gathered} \tag{3-1}$$

We have:

$$\frac{dP}{dV}=\frac{d(IV)}{dV}=I+V\frac{dI}{dV}\cong I+V\frac{\Delta I}{\Delta V} \tag{3-2}$$

From equations (3-1) and (3-2) we can obtain the following:

$$\begin{gathered}\frac{\Delta I}{\Delta V}=-\frac{I}{V} \rightarrow at\ MPP, \\ \frac{\Delta I}{\Delta V}>-\frac{I}{V} \rightarrow left\ side\ of\ MPP\ , \\ \frac{\Delta I}{\Delta V}<-\frac{I}{V} \rightarrow right\ side\ of\ MPP. \end{gathered} \tag{3-3}$$

Henceforth, the MPPT algorithm modulates the reference voltage V_{DC}^{*} according to the environmental condition in order to keep the operating point of the PV panels as close as possible to the real MPP.

In order to regulate the DC voltage to the rated value, the error $(e_{VDC}=V_{PV}-V_{DC}^{*})$ is processed by the proposed *PI-FLC*. The latter sets the reference for the d-axis current ${I_{MP}}^{*}$ that corresponds to the maximum PV power as shown in Figure 3-3.

Knowing that in order to guarantee the controllability of the inverter as an active power filter, it is required that the MPP DC voltage must be kept higher than the peak value of the PCC voltage plus the voltage drop in the inductances. If the PV source is incapable of providing the required reference voltage because of the ambient conditions (e.g. absence of irradiance), then the active power filter will get the energy from the grid to maintain the voltage level at the desired reference, behaving in this way as a traditional active power filter.

3.6 Active power filtering control based instantaneous power theory *p-q*

To satisfy the active filtering functionality, instantaneous power theory so-called *p-q theory* is proposed to generate the current reference signals for the harmonics' and reactive power's compensation [140].

Historically, the *p-q* theory in its first version was published in the Japanese language in July 1982 in a local conference and later in the journal *Transactions of the IEE-Japan* [141]. With a slight time lag, it was published in an international conference in 1983 [142], and in the *IEEE Transactions on Industry Applications* in 1984 [143].

The main motivation behind using *p-q* instantaneous power theory is due to its clear and intuitive concept in determining the different undesired power, and proved itself in terms of efficiency and flexibility in the control design for power conditioners based on power electronics devices.

3.6.1 Principal of the *p-q* theory

The principle of the instantaneous power theory consists in transforming the alternating electric quantities (voltages, currents) given in the reference abc to a fixed reference using the $\alpha\beta$ transformation or what is called *Clarke transformation* [144]; in a three-phase three-wire system we have:

$$\begin{bmatrix} v_\alpha \\ v_\beta \end{bmatrix} = C_{\alpha\beta} \begin{bmatrix} v_a \\ v_b \\ v_c \end{bmatrix}, \qquad \begin{bmatrix} i_\alpha \\ i_\beta \end{bmatrix} = C_{\alpha\beta} \begin{bmatrix} i_a \\ i_b \\ i_c \end{bmatrix} \tag{3-4}$$

Where,

$$C_{\alpha\beta} = \sqrt{\frac{2}{3}} \begin{bmatrix} 1 & -1/2 & -1/2 \\ 0 & \sqrt{3}/2 & -\sqrt{3}/2 \end{bmatrix}, \qquad C_{\alpha\beta}^{-1} = \sqrt{\frac{2}{3}} \begin{bmatrix} 1 & 0 \\ -1/2 & \sqrt{3}/2 \\ -1/2 & -\sqrt{3}/2 \end{bmatrix} \tag{3-5}$$

The instantaneous three-phase power in the abc system is given by:

$$p_{3\varphi} = v_a i_a + v_b i_b + v_c i_c \tag{3-6}$$

Using the transformations given in (3-4), this power will be defined in the $\alpha\beta0$ system by:

$$p_{3\varphi} = v_\alpha i_\alpha + v_\beta i_\beta \tag{3-7}$$

The graphic representation of this transformation without zero sequence component is illustrated in Figure 3-5. The voltage and current vectors are given by:

$$\begin{aligned} \vec{v} &= v_\alpha + jv_\beta \\ \vec{i} &= i_\alpha + ji_\beta \end{aligned} \tag{3-8}$$

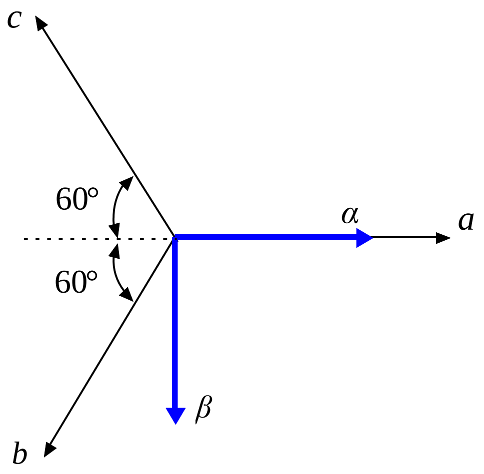

Figure 3-5 *Graphical representation of the abc-$\alpha\beta$ transformation.*

The instantaneous complex power (s) is defined by the product of the *PCC* voltage vector (v) and the conjugate of current (i^*) is calculated as follows:

$$\begin{aligned} s = v * i^* &= (v_\alpha + jv_\beta) * (i_\alpha - ji_\beta) \\ &= (v_\alpha * i_\alpha + v_\beta * i_\beta) * j(v_\beta * i_\alpha - v_\alpha i_\beta) = p + jq \end{aligned} \tag{3-9}$$

From equation (3-9) the instantaneous active p and reactive power q can be written in matrix form as follows:

$$\begin{bmatrix} p \\ q \end{bmatrix} = \begin{bmatrix} v_\alpha & v_\beta \\ -v_\beta & v_\alpha \end{bmatrix} * \begin{bmatrix} i_\alpha \\ i_\beta \end{bmatrix} \tag{3-10}$$

In other hand, the currents i_α, i_β can be obtained by inverting (3-10) as follows:

$$\begin{bmatrix} i_\alpha \\ i_\beta \end{bmatrix} = \frac{1}{v_\alpha^2 + v_\beta^2} \begin{bmatrix} v_\alpha & -v_\beta \\ v_\beta & v_\alpha \end{bmatrix} * \begin{bmatrix} p \\ q \end{bmatrix} \tag{3-11}$$

In order to illustrate the active and reactive currents on the $\alpha\beta$ axes, the following equation can be developed:

$$\begin{aligned} \begin{bmatrix} i_\alpha \\ i_\beta \end{bmatrix} &= \frac{1}{v_\alpha^2 + v_\beta^2} \begin{bmatrix} v_\alpha & -v_\beta \\ v_\beta & v_\alpha \end{bmatrix} * \begin{bmatrix} p \\ 0 \end{bmatrix} + \frac{1}{v_\alpha^2 + v_\beta^2} \begin{bmatrix} v_\alpha & -v_\beta \\ v_\beta & v_\alpha \end{bmatrix} * \begin{bmatrix} 0 \\ q \end{bmatrix} \\ &= \begin{bmatrix} i_{\alpha p} \\ i_{\beta p} \end{bmatrix} + \begin{bmatrix} i_{\alpha q} \\ i_{\beta q} \end{bmatrix} \end{aligned} \tag{3-12}$$

With $i_{\alpha p}$ and $i_{\beta p}$, the instantaneous active currents on the $\alpha\beta$ axes, can be given respectively by:

$$i_{\alpha p} = \frac{-v_\beta}{v_\alpha^2 + v_\beta^2} p, \qquad i_{\beta p} = \frac{v_\beta}{v_\alpha^2 + v_\beta^2} p \tag{3-13}$$

Moreover, $i_{\alpha q}$ and $i_{\beta q}$, the instantaneous reactive currents on the $\alpha\beta$ axes, can be given respectively by:

$$i_{\alpha q} = \frac{-v_\beta}{v_\alpha^2 + v_\beta^2} q, \qquad i_{\beta q} = \frac{v_\beta}{v_\alpha^2 + v_\beta^2} q \tag{3-14}$$

Replacing the currents i_α, i_β by their active and reactive components above in equation (3-7), the equation can be rewritten as:

$$\begin{aligned} p_{3\varphi} &= v_\alpha i_{\alpha p} + v_\beta i_{\beta p} + v_\alpha i_{\alpha q} + v_\beta i_{\beta q} \\ &= \frac{v_\alpha^2}{v_\alpha^2 + v_\beta^2} p + \frac{v_\beta^2}{v_\alpha^2 + v_\beta^2} p + \frac{-v_\alpha v_\beta}{v_\alpha^2 + v_\beta^2} q + \frac{v_\alpha v_\beta}{v_\alpha^2 + v_\beta^2} q, \\ & where\ \frac{-v_\alpha v_\beta}{v_\alpha^2 + v_\beta^2} q + \frac{v_\alpha v_\beta}{v_\alpha^2 + v_\beta^2} q \equiv 0 \end{aligned} \tag{3-15}$$

Note that the last two terms cancel each other out, this brings us to an important conclusion of this theory: The energy transfer between the source and the charge is only carried out through the active components on the $\alpha\beta$ axes, that is, the real power p. The imaginary power q is an energy per unit of time exchanged between the wires of the three-phase system as demonstrated in Figure 3-6.

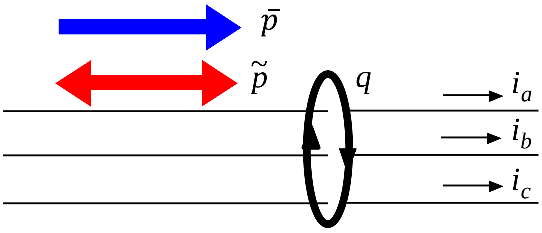

Figure 3-6 *Flow of instantaneous powers in a three-phase system.*

3.6.2 The application of *p-q* theory on the multi-functional inverter as an active power filter

Besides the maximum power tracking and power conversion capabilities, the proposed inverter can act as an active power filter simultaneously. Consequently, the p-q theory is applied in the proposed system that corresponds to the Figure 3-2 in order to perform the active filtering capability. The nonlinear load connected to PCC absorbs harmonic currents (i_{La}, i_{Lb}, i_{Lc}) under three-phase balanced voltage source (v_a, v_b, v_c). Then according to the previous section, the p_L is the instantaneous active power absorbed by the nonlinear load that is supplied by the grid (and/or the PV source in our case), and q_L

is the instantaneous reactive power that is defined as the energy exchanged between the wires of the three-phase system, (v_α, v_β) and $(i_{L\alpha}, i_{L\beta})$ are the Clarke's transformation of the PCC three phase voltages and the nonlinear load currents respectively.

The calculated active and reactive powers p_L and q_L of the nonlinear load can be separated into their average parts ($\bar{p}_L$, $\bar{q}_L$) and oscillating parts ($\tilde{p}_L$, $\tilde{q}_L$), and they can be expressed as follows:

$$\begin{bmatrix} p_L \\ q_L \end{bmatrix} = \begin{bmatrix} \bar{p}_L + \tilde{p}_L \\ \bar{q}_L + \tilde{q}_L \end{bmatrix} \tag{3-16}$$

For the separation of $\bar{p}_L$ and $\tilde{p}_L$ from p_L, a Butterworth low pass filter (LPF) is used. Since the efficiency of the identification strongly depends on it, the parameters thereof are adjusted in order to ensure a satisfactory static response and error. For this purpose, we opted for a fourth-order filter with a cut-off frequency of $20\ Hz$, and for which the frequency response as well as the time response are given in Figure 3-7.

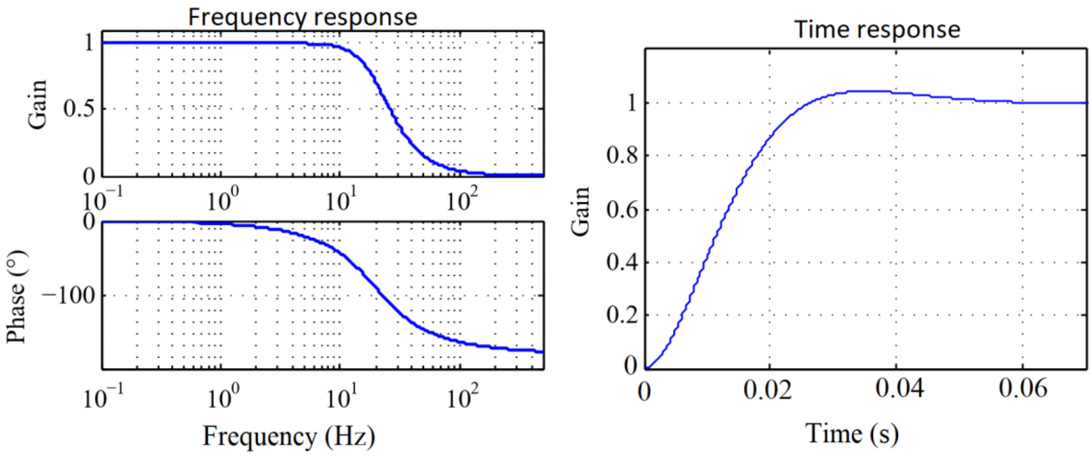

Figure 3-7 *Frequency and time response of the low pass filter (LPF).*

The generated reference currents of the active power filter control corresponding to the powers that to be compensated are obtained as,

$$\begin{bmatrix} i_{C\alpha}{}^{*} \\ i_{C\beta}{}^{*} \end{bmatrix} = \frac{1}{{v_\alpha}^2 + {v_\beta}^2} \begin{bmatrix} v_\alpha & v_\beta \\ v_\beta & -v_\alpha \end{bmatrix} * \begin{bmatrix} -\tilde{p}_L \\ -q_L \end{bmatrix} \tag{3-17}$$

Note that the total reactive power $-q_L$ that is being compensated in (3-17) is taken in order to obtain the unity power factor in the grid. The reason for negating the compensating powers is to affirm that the active power filter algorithm generates a compensating current that produces exactly the inverse of the undesirable powers drawn by the nonlinear load. Finally, the generated compensating currents in $\alpha\beta$ frame to transformed to dq synchronous frame at the grid angular frequency ($\hat{\theta}$) using Park transformation Eq. (3-18) to be in line with the Synchronous Current Control for the inverter control. The angular frequency ($\hat{\theta}$) is generated using the *phase-locked loop* (PLL) which will be described hereafter.

$$\begin{bmatrix} i_{Cd}{}^* \\ i_{Cq}{}^* \end{bmatrix} = \begin{bmatrix} \cos(\hat{\theta}) & \sin(\hat{\theta}) \\ -\sin(\hat{\theta}) & \cos(\hat{\theta}) \end{bmatrix} * \begin{bmatrix} i_{C\alpha}{}^* \\ i_{C\beta}{}^* \end{bmatrix} \tag{3-18}$$

The following diagram of the *p-q theory* shown in Figure 3-8 represents the harmonic current identification algorithm block in Figure 3-3.

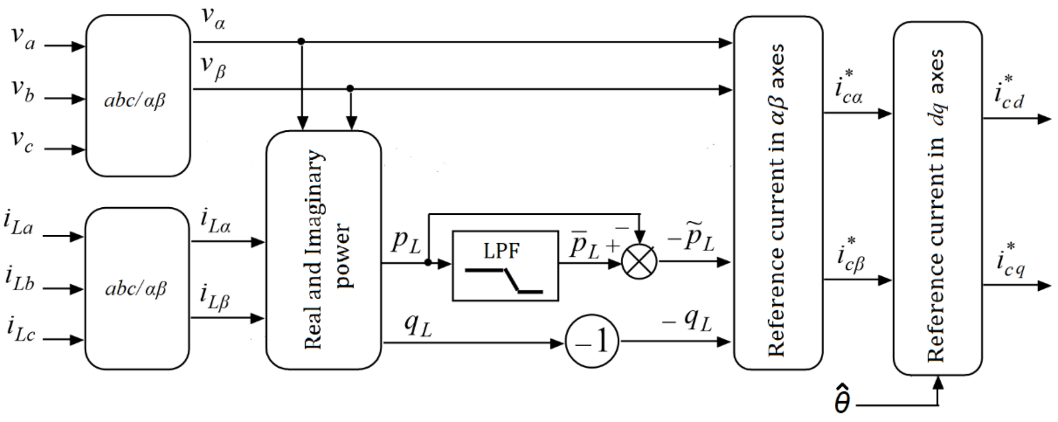

Figure 3-8 *Harmonic current identification algorithm based p-q theory.*

3.6.3 Illustrative example

To evaluate the active filtering functionality using the pq theory an illustrative simulation result will be demonstrated here. However, for this simulation example, the additional current from PV generator is not taken into account. This is just an illustration of the separation of the harmonics from the current is considered, in other words, it is an *identification of the harmonic currents and not for the reference currents*.

A three-phase current with harmonics ranks of 1, 5, 7, 11, 13 …etc. is considered under healthy balanced three-phase voltages as shown in Figure 3-9. The three-phase currents after filtering in Figure 3-9 (C) shows a very satisfactory filtering.

Moreover, Figure 3-10 effectively shows that the instantaneous real power is constant, and that the imaginary power is zero after filtering. Figure 3-11 demonstrates the generated reference current from harmonic current identification algorithm based on the pq theory, to testify the proper operation of the algorithm, the α transformation of the input current ($i_{L\alpha}$) subtracted from the generated compensating reference current by the algorithm ($i_{C\alpha}{}^{*}$), the result should be a pure sine wave without unwanted harmonics. Figure 3-12 shows the FFT analyses of the current with and without filtering.

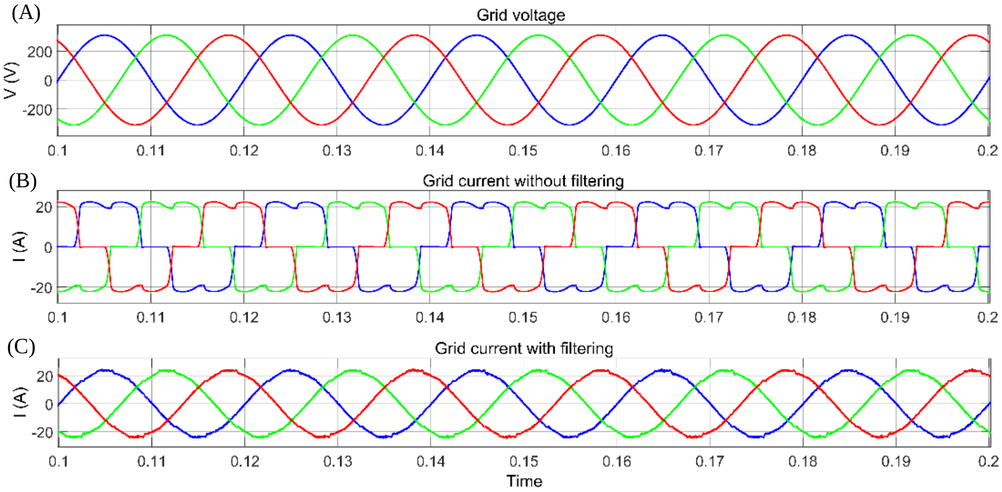

Figure 3-9 *(A) Grid voltage, (B) grid current without filtring, (C) grid current with filtering.*

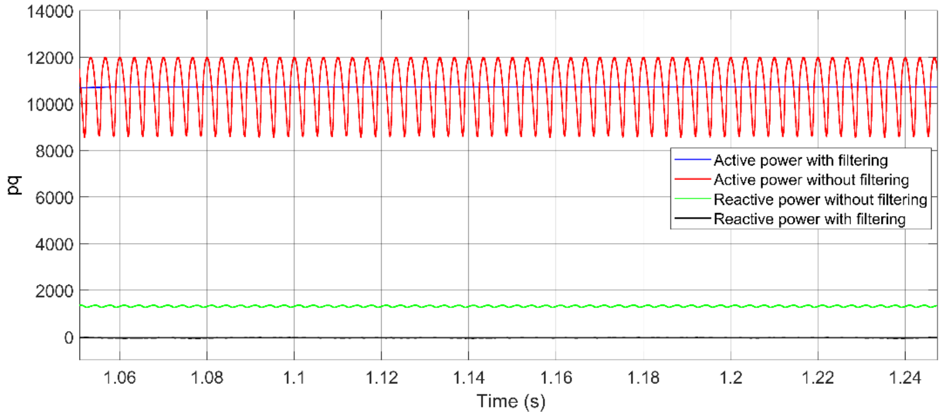

Figure 3-10 *The instantaneous power with and without filtering.*

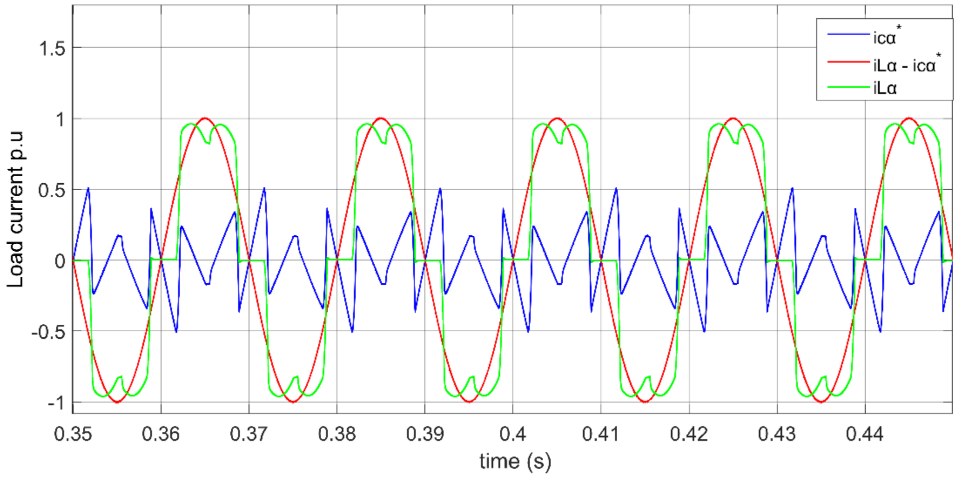

Figure 3-11 *The generated reference current using pq theory.*

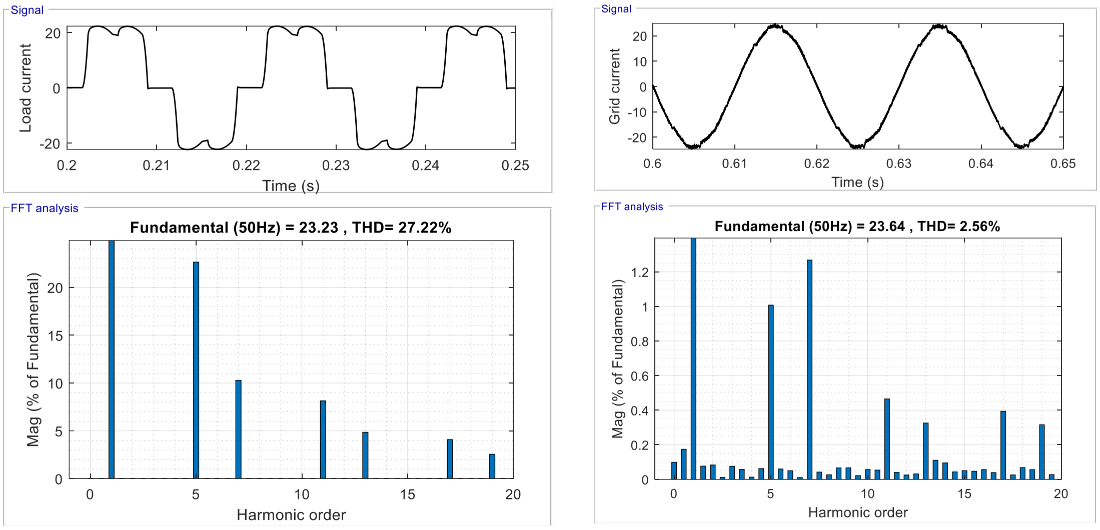

(a) (b)

Figure 3-12 *FFT analysis of (a) grid current without filtring, (b) grid current with filtering.*

3.7 Inverter Synchronous Current Control for grid connection PV system

The synchronous current controller scheme is based on converting the currents from abc or $\alpha\beta$ stationary reference frame to dq synchronous frame at the grid angular frequency ($\hat{\theta}$). Usually, this type of control scheme needs *PI* controllers to reduce the errors of the fundamental component to zero. In this work, the conventional regulators (Voltage and currents) are replaced by the proposed FLC to track the reference correctly and provide better robustness.

The dq components of the reference current that aimed to be tracked is as follows,

$$\begin{cases} i_{Fd}{}^{*} = i_{Cd}{}^{*} + I_{MP}{}^{*} \\ i_{Fq}{}^{*} = i_{Cq}{}^{*} \end{cases} \tag{3-19}$$

Where $i_{Cd}{}^{*}$ and $i_{Cq}{}^{*}$are the Park's transformation of the generated reference currents $i_{C\alpha}{}^{*}$and $i_{C\beta}{}^{*}$ from equation (3-18) and $I_{MP}{}^{*}$ is the reference current that corresponds the injected PV maximum power.

These references $i_{Fd}{}^{*}$ and $i_{Fq}{}^{*}$ are compared with the measured inverter currents in dq reference frame (i_{Fd} and i_{Fq}), and the error is processed using the proposed fuzzy controller to generate the corresponding voltage reference (v_{Fd}^{*} and v_{Fq}^{*}).

$$\begin{cases} e_d = i_{Fd}{}^{*} - i_{Fd} \\ e_q = i_{Fq}{}^{*} - i_{Fq} \end{cases} \tag{3-20}$$

v_{Fd}^{*} and v_{Fq}^{*} are transformed back to the abc coordinates using the inverse Park's transformation in order to get the three-phase reference voltage v_{Fabc}^{*} for the SVPWM. This latter will be responsible for generating the adequate pulsation of the inverter's power switches.

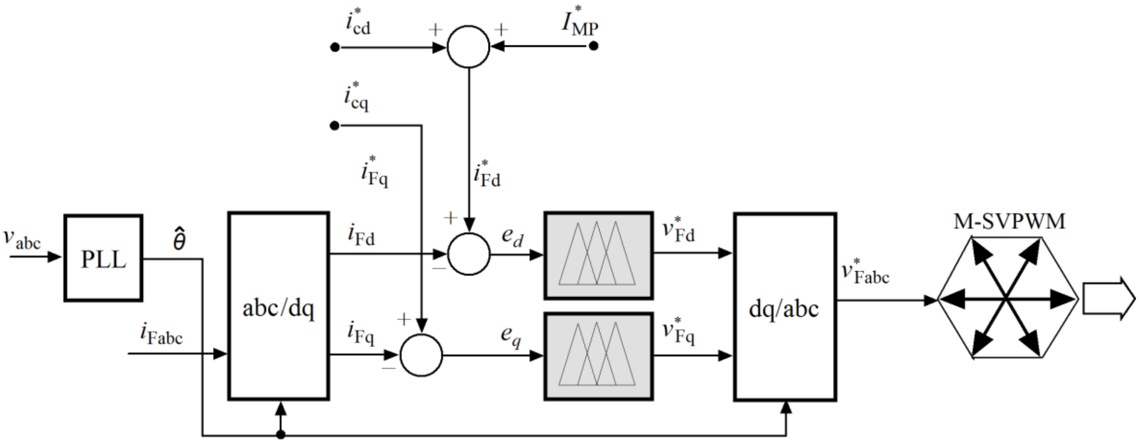

Figure 3-13 *Synchronous Current Control part for grid-connection PV system.*

3.7.1 Phased-locked-loop (PLL)

In the grid-interactive inverter control, the knowledge of the amplitude and/or phase, and frequency of voltages measured at the connection point (PCC) is often imperative. The most well-known algorithm for grid voltage phase angle ($\hat{\theta}$) identification is illustrated in Figure 3-14, and commonly referred as Phase Locked Loop (PLL). The PLL is constantly working in order to keep the output voltage from the inverters synchronized with the grid. The voltages measured at the connection point (v_a, v_b, v_c) are transformed in the fixed dq frame using Park's transformation, and the phase locking is achieved only by regulating the voltage v_q to zero by means of *PI* controller, this is why the reference ${v_q}^{*}$ must be set to zero [144].

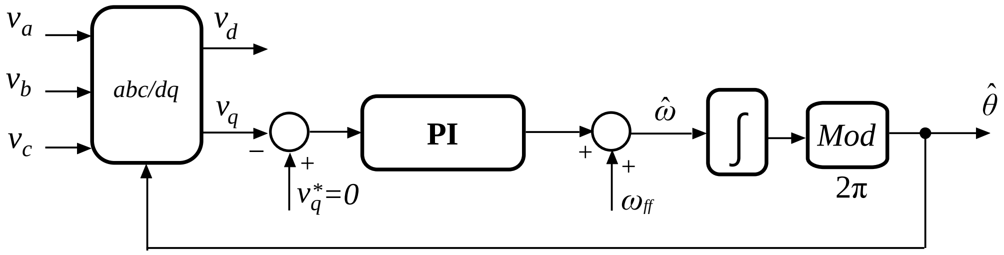

Figure 3-14 *PLL block diagram.*

Recalling that the input voltages are:

$$\begin{aligned} v_a &= V_m * \sin(\omega t) \\ v_b &= V_m * \sin(\omega t - 2\pi/3) \\ v_c &= V_m * \sin(\omega t + 2\pi/3) \end{aligned} \tag{3-21}$$

Using Park's transformation, the abc to dq transformation is defined as below:

$$\begin{bmatrix} v_d \\ v_q \end{bmatrix} = 2/3 \begin{bmatrix} \cos(\hat{\theta}) & \cos(\hat{\theta} - 2\pi/3) & \cos(\hat{\theta} + 2\pi/3) \\ -\sin(\hat{\theta}) & -\sin(\hat{\theta} - 2\pi/3) & -\sin(\hat{\theta} + 2\pi/3) \end{bmatrix} * \begin{bmatrix} v_a \\ v_b \\ v_c \end{bmatrix} \tag{3-22}$$

As mentioned before, the controller is designed to drive the q component to zero, thus aligning the phase $\hat{\theta}$ with the peak of the phase a voltage.

The *PI* controller can be formulated as follows:

$$G_c(s) = \frac{k_p s + k_i}{s} \tag{3-23}$$

The output of the controller is the actuation signal and it is added to the feedforward frequency ω_{ff}. The output of the sum block is the frequency in radians and is integrated to obtain the angle $\hat{\theta}$.

The purpose of the feedforward frequency is to have the *PI-regulator* control for an output signal that goes to zero. In our case the feedforward frequency will be $2\pi f = 100\pi$. In the ideal case when the grid frequency is exactly 50Hz once the regulator has tracked the phase, the output of the regulator is zero.

The output of the integrator is passed to a modulo operation with a constant of 2π, so that the mod block properly wraps the angle $\hat{\theta}$ and maintains it between 0 and 2π.

The open loop transfer function of the PLL system is:

$$G_{OL}(s) = V_m \frac{k_p s + k_i}{s} \frac{1}{s} \tag{3-24}$$

Going from open loop to the closed loop system the transfer function becomes:

$$G_{CL}(s) = \frac{G_{OL}(s)}{1 + G_{OL}(s)} = \frac{V_m(k_p s + k_i)}{s^2 + V_m k_p s + V_m k_i} \tag{3-25}$$

Where the natural frequency is:

$$\omega_n = \sqrt{V_m k_i} \tag{3-26}$$

And the damping ration is:

$$\zeta = \frac{V_m k_p}{2\sqrt{V_m k_i}} \tag{3-27}$$

At the point for grid connection of our system the grid voltage level is $380V$. This value is the root mean square value of the line-to-line voltage. The amplitude voltage level V_m is then calculated according to $V_m = \sqrt{2}\,(380/\sqrt{3}) = 310.27V$.

For a damping ration of $\zeta = 0.7$ and natural frequency of $100Hz$, according to equations (3-26) and (3-27) the *PI* parameters are:

$$k_p = 2.84 \quad and \quad k_i = 1272.39 \tag{3-28}$$

In the Figure 3-15 (A) and (B) show the *d* and *q* components of the grid voltage in the PLL system, we can see clearly that the *q* component is regulated to zero all along the simulation in order to achieve the phase locking. Figure 3-15 (C) and (D) show respectively the grid voltage phase angle ($\hat{\theta}$) and the three-phase voltage at the PCC.

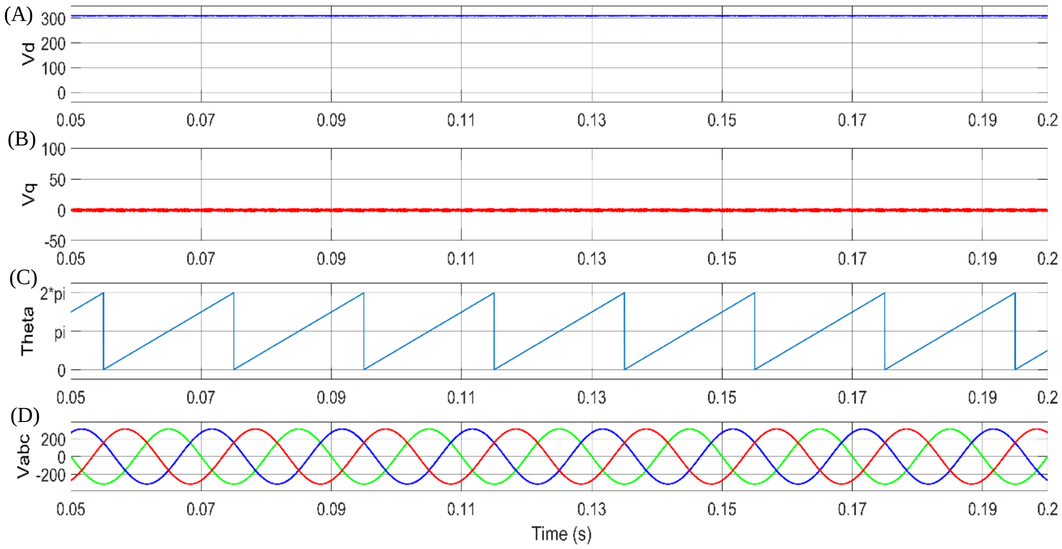

Figure 3-15 *(A) d component of grid voltage, (B) q component of grid voltage, (C) grid voltage phase angle ($\hat{\boldsymbol{\theta}}$), (D) Three-phase grid voltage.*

Using the values of equation (3-28) in equation (3-24) and (3-25) that give the TFs for the open-loop ($G_{OL}(s)$) and the closed-loop ($G_{OL}(s)$) systems and from these TFs the bode plot of the system is illustrated in Figure 3-16. We can see from the bode plot that the closed-loop system confirms the low pass filter behaviour of the system; also it is crossing the zero *dB* gain at about $100Hz$ which represent our bandwidth.

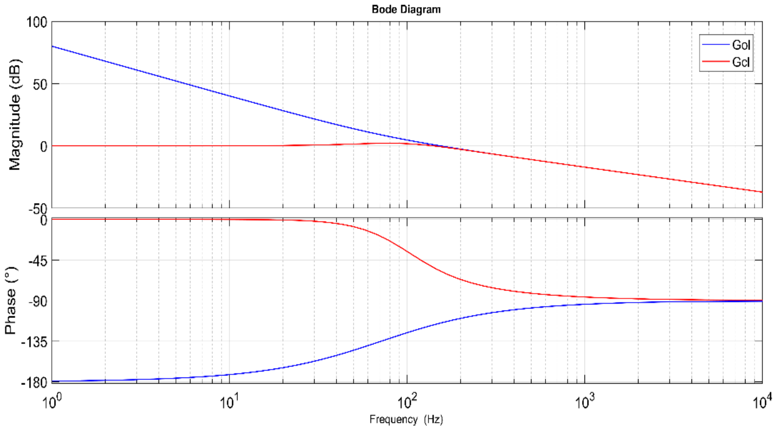

Figure 3-16 *Bod-plot of the transfer function of the PLL system.*

3.8 Introduction to fuzzy logic theory

The application of the fuzzy logic theory in the processes of decision making and system's control is very well established particularly in the beginning of the nineties [145][146]. Among other things, it finds applications in electro-energetic systems [147][148], power electronics systems and electrical drives [149][150][151]. For inverter controller in PV applications, several contributions have emerged, especially during the last decade [135].

Fuzzy logic control (FLC) theory is based on the principle of human experience and intuition, compared to the conventional linear controllers, the FLC design does not require the exact mathematical model of the system, along with their ability to handle the nonlinearities. Indeed, unlike classical logic, which recognizes information that is only absolutely true or absolutely false, that is to say in binary language either 1 or 0, fuzzy logic admits information always with a degree of truth and a degree of falsity, therefore in this logic the decision can be from 0 to 1. The theory of fuzzy logic is based on the *fuzzy sets* introduced by *Zedah* [152].

3.8.1 Fuzzy sets

A fuzzy set is a set without sharp clearly defined boundaries. A classic set can be defined by:

$$A = \{x \in U | P(x)\} \tag{3-29}$$

Where the element of A has the property P, and U denotes the universal discourse. The function characteristic $\mu_A(x): U \rightarrow \{0,1\}$ takes the value 0 if x is not an element of A and 1 if x is an element of A. For example if on the universal discourse of [-10, 10] we consider as a property $x > 5$, then it is logical that $\mu_A(0) = 0, \mu_A(10) = 1$, and $\mu_A(4.9) = 0, \mu_A(5.1) = 1$. However, according to our opinion, is the value 4.9 small compared to 5? or is 5.1 large compared to 5?

In fuzzy set theory, the concept of the characteristic function is generalized, and known as the *membership function* $\mu_A(x): U \rightarrow \{0,1\}$. This membership function assigns each element x in U a membership value or a membership degree between 0 and 1. Thus, in the example above, for the value 10, the property $x > 5$ is 100% true, i.e $\mu_A(10) = 1$, but for 5.1, this property may not be true at 5% for example, i.e $\mu_A(5.1) = 1$. A fuzzy set is defined by:

$$A = \{(x, \mu_A(x)) | x \in U\} \tag{3-30}$$

3.8.2 Membership function

There are several forms of membership functions used in fuzzy set theory. The best known are given in Figure 3-17. It is generally not easy to choose one shape over another, however in control applications triangular and Gaussian shapes are the most popular [153].

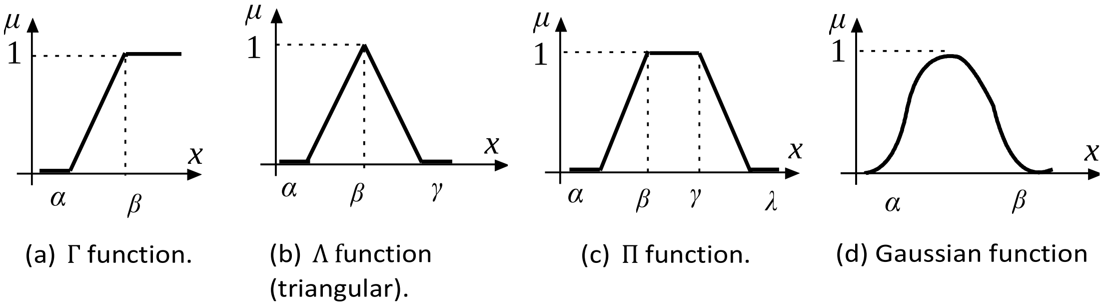

(a) Γ function.
(b) Λ function (triangular).
(c) Π function.
(d) Gaussian function

Figure 3-17 *Some different forms of membership functions.*

3.8.3 Linguistic variables

The concept of linguistic variable is used to describe real physical variables. It is the basis of fuzzy controllers. A conventional variable is defined by a precise numerical value, when a linguistic variable is larger and imprecise. A linguistic variable is often a word or a sentence, which qualifies from a human perception the state of a physical variable, for example, between -10 and 10, one can qualify the elements between -10 and 0 as *NEGATIVES*, those between -5 and 5 as *ZEROS*, and between 0 and 10 as *POSITIVES*. We can notice on one hand the imprecision of these variables, and on the other hand, the interference between the variables, that is to say an element can be negative and zero at the same time.

3.8.4 Fuzzy logic operators

The linguistic variables are related to each other at the level of fuzzy inferences by operators of fuzzy logic intervening on the membership functions representing the linguistic variables. Here are four main operators:

$$\begin{array}{ll} \text{Negation } (\textbf{NOT}) & \mu_{\bar{A}}\,(x) = 1 - \mu_A\,(x) \\ \text{Conjunction } (\textbf{AND}) & \mu_C\,(z) = \mu_{A\,AND\,B}\,(z) = min[\mu_A\,(x), \mu_B\,(x)] \\ \text{Disjunction } (\textbf{OR}) & \mu_C\,(z) = \mu_{A\,OR\,B}\,(z) = max[\mu_A\,(x), \mu_B\,(x)] \\ \text{Implication} & If \ldots then \ldots\ statement \end{array} \tag{3-31}$$

Implication is an important connection in fuzzy logic control algorithms, because the enslavement strategy is often dictated by a set of rules ($If \ldots then \ldots$). There are several methods of involvement, but the most well-known are:

Implication of Zadeh
$$\mu_C\,(x,y) = \max\{min[\mu_A\,(x), \mu_B\,(y)], 1 - \mu_A\,(x)\} \tag{3-32}$$

Implication of Mamdani
$$\mu_C\,(x,y) = min[\mu_A\,(x), \mu_B\,(y)] \tag{3-33}$$

3.9 General structure fuzzy logic control

Figure 3-18 demonstrates the general block diagram of a fuzzy controller. Four main elements should be distinguished, namely: Fuzzification module, Rule-base, Inference engine and Defuzzification module. Input and output gains (Scaling factors) may possibly be required.

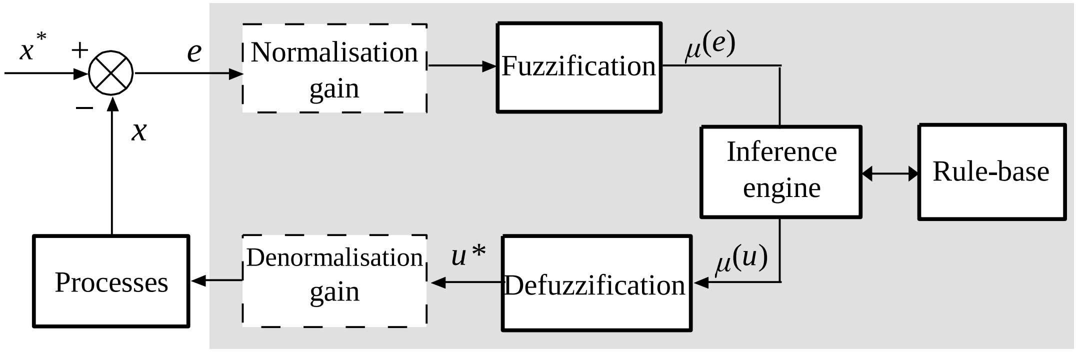

Figure 3-18 *Gneral schimatic block of fuzzy logic controller.*

3.9.1 Fuzzification

The fuzzification is an input interface step used to convert the real or crisp input value which is generally the error between the value of a variable and its set-point, into linguistic values using Membership Functions (MFs), the linguistic values or terms will be then processed by the fuzzy inference engine and the rule-base by assigning for each input variable a set of fuzzy subsets on the universal discourse.

3.9.2 Rule-base

The rule base consists of entering all the rules ($If \ldots then \ldots$) into the inference engine. These rules will be interpreted by the technique of implication. The rule base is very important (if it is not the most important), because it dictates the reaction of the fuzzy controller in the face of variations of the slave variable. Knowledge of the system to be controlled is often necessary to formulate these rules.

Fuzzy inference links the input quantities (fuzzified) and the output quantities (fuzzified), by the set of dictated rules. These rules are combined by the operators (AND, OR, NOT). There are several types of fuzzy inferences, and the best known are illustrated graphically in Figure 3-19.

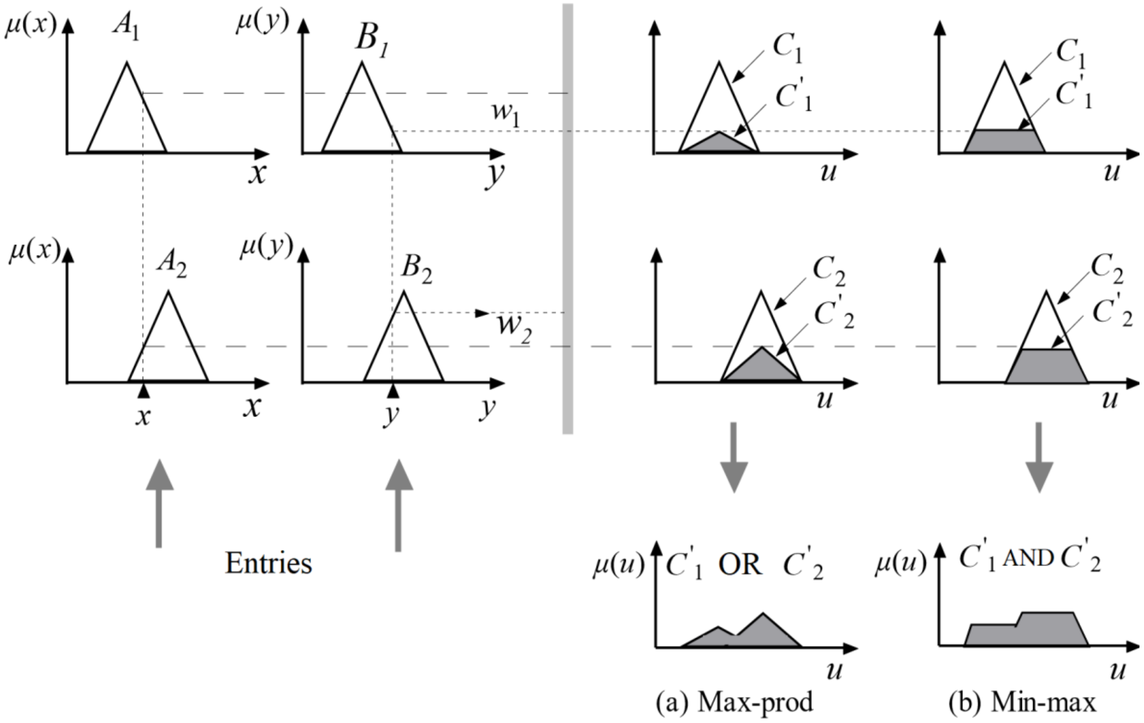

Figure 3-19 *Graphical representation of fuzzy inference by max-prod and min-max methods.*

3.9.2.1 Max-prod method

This method uses the standard representations for the input and output subsets. The activation weight of a rule is used to multiply the membership function of the output subset imposed by this rule. The global action (or the command value) is the union of the actions produced by each subset individually.

3.9.2.2 Min-max method

This method is the most mentioned in the literature. It uses the same descriptions for the output subsets as for the input subsets on the condition of each rule R_i is assigned an activation weight w_i, which depends on the condition itself and input values. For the operation AND, we use the min operator. The activation weight is used as the clipping constant for the output subset imposed by the consequent part of the rule R_i. The union of the clipped subsets forms the output subset.

3.9.3 Defuzzification

The result of fuzzy inference is a membership function, however, a controller requires an accurate control signal. The transformation of fuzzy information into determined information is defuzzification. There are several defuzzification methods proposed in the literature, in here, we are going to present two main methods.

3.9.3.1 Mean-of-Maximum method (MOM)

This method generates a precise order by calculating the average of the values for which the membership is maximum (Figure 3-20 (a)). This command can be determined mathematically by:

$$u^* = \frac{\int_S udu}{\int_S udu} \quad or \quad S = \{u_i \in U: \mu(u_i) = \sup(\mu(u))\} \tag{3-34}$$

3.9.3.2 Center-of-Gravity method (COG)

This is the most widely used defuzzification method. It consists in determining the cordinator of the center of gravity u^* of the membership function resulting from the inference $\mu(u)$. This cordinator corresponds to the output value of the regulator. Figure 3-20 (b) shows the principle of this defuzzification method.

$$u^* = \frac{\int u\mu(u)du}{\int \mu(u)du} \tag{3-35}$$

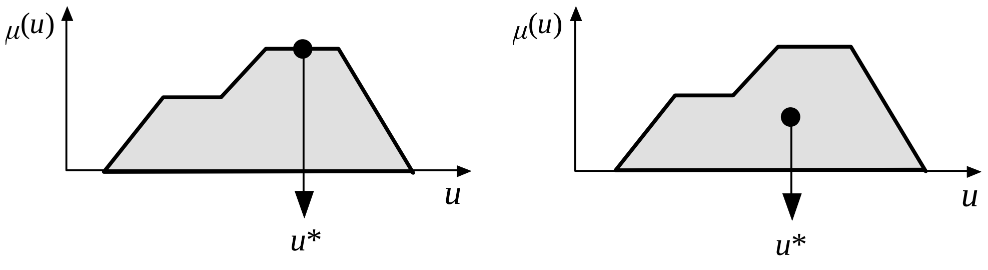

(a) Mean-of-Maximum method (MOM) (b) Center-of-Gravity method (COG)

Figure 3-20 *Defuzzification methods.*

3.10 The proposed PI-like FLC for multi-functional inverter control

The control equation of conventional PI-controller is given as follows:

$$u = K_p * e + K_i * \int e \, dt \tag{3-36}$$

Where K_p and K_i are the proportional and the integral gain coefficients.

Using the digital approximation of the equation (3-36),

$$u_k = K_p * e_k + K_i * \sum_{j=1}^{k} e_j * T_s \tag{3-37}$$

Furthermore, by analogy with a conventional controller, we have the following:

$$\begin{cases} e_k = y_{ref} - y_k \\ \Delta e_k = e_k - e_{k-1} = y_{k-1} - y_k \\ \Delta u_k = u_k - u_{k-1} \end{cases} \tag{3-38}$$

In the above expressions, e_k is the error between the reference y_{ref} and the process output y_k, Δe_k and Δu_k are the change-of-error and the change-of-control output respectively, and k refers to the time instant. In our case y may represent either the DC-link voltage or the inverter AC current.

From (3-38) and (3-37) we deduce:

$$\Delta u_k = \left(K_p * e_k + K_i * \sum_{j=1}^{k} e_j * T_s \right) - \left(K_p * e_{k-1} + K_i * \sum_{j=1}^{k-1} e_j * T_s \right) \tag{3-39}$$

$$\Delta u_k = K_p * \Delta e_k + K_i * e_k * T_s \tag{3-40}$$

A Fuzzy controller can be represented as [153]:

$$\Delta U_k = F_n(E_k + \Delta E_k) \tag{3-41}$$

$$G_u * \Delta u_k = F_n(G_e * e_k + G_{\Delta e} * \Delta e_k) \tag{3-42}$$

Where G_e, $G_{\Delta e}$, and G_u are the scaling factors for e_k, Δe_k, and Δu_k respectively, and F_n is the nonlinear function representing the FLC input-output function.

Therefore, it is possible to obtain the fuzzy PI controller (PI-FLC) using the error e_k and the change of error Δe_k as inputs to the FLC, while the output of the FLC is an incremental change of the control signal Δu_k. The schematic structure of the PI-FLC is illustrated in Figure 3-21.

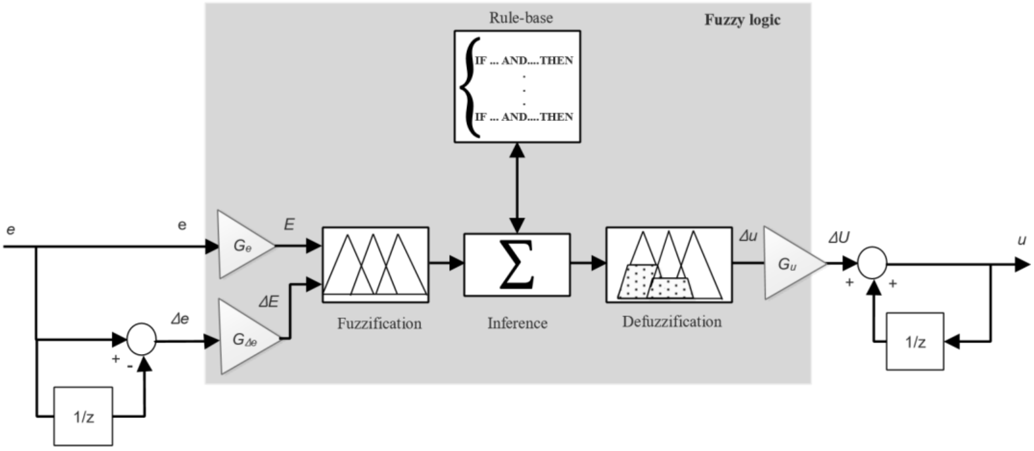

Figure 3-21 *The proposed PI-like fuzzy logic controller architecture.*

3.10.1 The proposed strategy for PI-FLC tuning

The Fuzzy controller design implies the selection of the parameters pertaining to each of the three essential processes (Fuzzification, Fuzzy inference, and Defuzzification). The complexity comes from the fact that different options are available for each parameter and hence the optimized structure is difficult to achieve. In our work, a systematic method is proposed to tune the fuzzy controller gains (*Scaling Factors*) and to set the fuzzy control rules.

3.10.1.1 Tuning the scaling factors

Upon the comparison of equations (3-40) and (3-42), one can deduce that, beside the normalization function, the scaling factors G_e, $G_{\Delta e}$, and G_u have similar effects of (K_p, K_i) of the conventional *PI* controller in terms of control performance and stability issues.

From the above, the control signal u_n is the sum of all previous increments,

$$u_k = \sum_j (\Delta u_j * G_u * T_s) \tag{3-43}$$

Herein, the linear approximation of the controller can be expressed as follows:

$$\begin{aligned} u_k &= \sum_{j=1}^{k} (E_j + \Delta E_j) * G_u * T_s \\ &= G_u * \sum_{j=1}^{k} \left[G_e * e_j + G_{\Delta e} * \frac{e_j - e_{j-1}}{T_s} \right] * T_s \\ &= G_u * \left[G_e * \sum_{j=1}^{k} e_j * T_s + G_{\Delta e} * \sum_{j=1}^{k} (e_j - e_{j-1}) \right] \end{aligned}$$

$$= G_{\Delta e} * G_u * \left[\frac{G_e}{G_{\Delta e}} * \sum_{j=1}^{k} e_j * T_s + e_k \right]$$

$$= (G_{\Delta e} * G_u) * e_k + (G_e * G_u) * \sum_{j=1}^{k} e_j * T_s \qquad (3\text{-}44)$$

Comparing (3-37) to (3-44) it is clear that the scaling factors from the linear approximation are related to the *PI* gains in the following way,

$$\begin{cases} K_p = G_{\Delta e} * G_u \\ K_i = G_e * G_u \end{cases} \qquad (3\text{-}45)$$

Notice that the proportional gain relies on $G_{\Delta e}$, while the integral gain relies on G_e. Therefore, the obtained tuning method is based on linearization of the PI-FLC function. The tuning process implies the adjusting the change-of-error scaling factor gain ($G_{\Delta e}$) to set the overshoot or the amplitude of oscillation and adjusting the scaling factor gain of the error (G_e) to set the process response.

Firstly, the maximum value of G_e is set in order to exploit the full range of the input error. For example, if the maximal absolute value of the reference step signal error that is processed by the conventional PI controller ($e_k = y_{ref} - y_k$) is equal to value (X). Therefore, to map the real input error within the boundary of the normalized universal discourse $[-1,1]$, the scaling factor G_e should be set to ($1/X$). Then the other scaling factors $G_{\Delta e}$ and G_u are calculated initially based on equation (3-45) and tuned according to the desired performance criteria.

3.10.1.2 Determination of fuzzy rules

The PI-FLC consists of rules of the form:

> *if* e_k is $< property\ symbol >$ and Δe_k is $< property\ symbol >$ *then* Δu_k is $< property\ symbol >$.

The process state variables of the rule-base representing the contents of the rule-antecedent (*if-part*) are the *error* e_k and the *change–of–error* Δe_k. While the output variable control representing the contents of the rule-consequent (*then-part*) is the change-of-control output Δu_k. Finally, in order to obtain the value of the control output variable u_k, the change of control output Δu_k is added to u_{k-1}.

Prior to the process of setting the appropriate rule base, selection of the number and type of fuzzy sets for input and output variable must be done. To this, the same fuzzy values, {*NB, NM, NS, ZE, PS, PM, PB*}, have been chosen for the three variables of e, Δe, and Δu where *NB* reads (negative big), *NM* (negative medium), *NS* (negative small), *ZE* (zero), *PS* (positive small), *PM* (positive medium), and *PB* (positive big).

For the efficient use of memory, computational efficiency, and simplicity, seven triangular-shaped membership functions covering the normalized universal discourse $[-1, 1]$ of each variable were selected as shown in Figure 3-22. Consequently, a total of forty-nine possible rules can be driven from the seven membership functions of each input variable. Figure 3-23 shows the surface characteristic of the PI-FLCs that corresponds to the input and output MFs.

For the sake of simplicity, the same number of fuzzy sets are applied in the three fuzzy controllers, DC-link voltage and inverter currents. One can notice that the triangular membership functions are asymmetrical (not equally-spaced) which implies that the FLC is drifted from linearity to nonlinearity. This would improve the controller performance in terms, i.e., overshoot value, rise-time, and amplitude of oscillations.

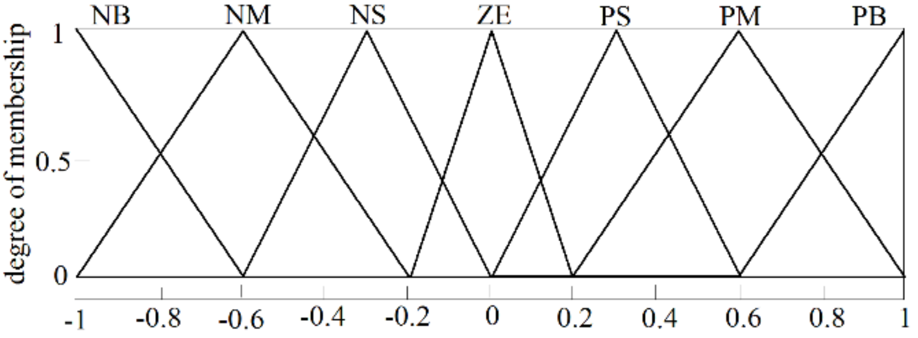

(a)

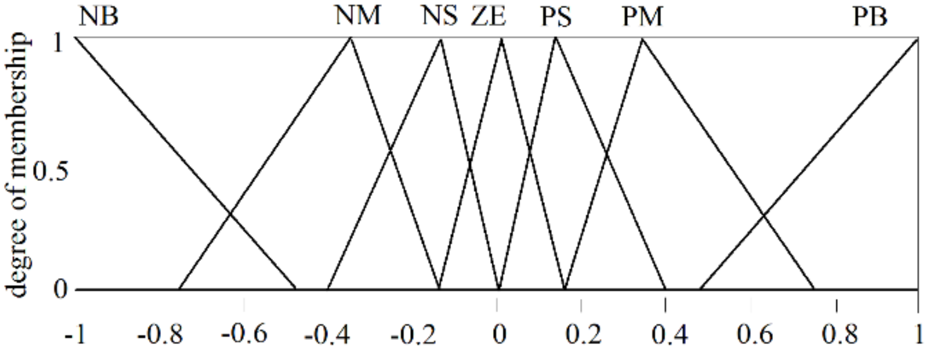

(b)

Figure 3-22 *(a) Input fuzzy variables membership functions* $\boldsymbol{e}$ *and* $\boldsymbol{\Delta e}$*, (b) output fuzzy variable membership functions* $\Delta \boldsymbol{u}$*.*

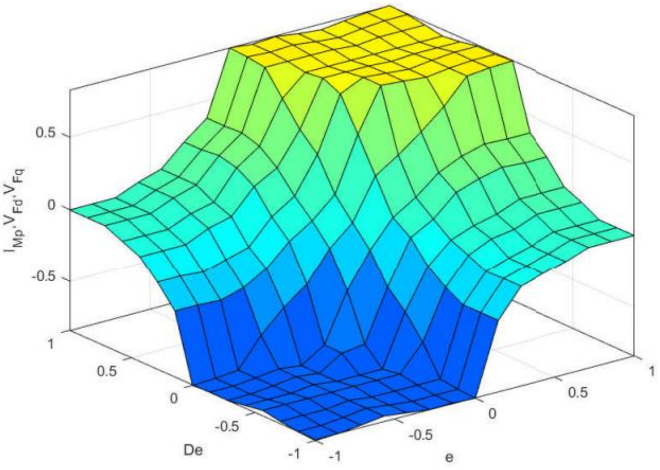

Figure 3-23 *Surface characteristic of the PI-FLC for the three controllers ($\boldsymbol{V_{DC}}$ controller, $\boldsymbol{i_{Fd}}$ controller, and $\boldsymbol{i_{Fq}}$ controller).*

In our work, a systematic method is proposed to set the required decision for a given set of inputs (e_k and Δe_k). By analyzing the phase plane trajectory defined by the error and change-of-error for any closed-loop controlled system. It can be noticed that knowing the location of (e_k, Δe_k) within the plane allows for the selection of the appropriate fuzzy value of the control variable, the desired phase plane trajectory is shown in Figure 3-24 (a). At any sample time e_k, Δe_k are computed where the first term $\left(e_k = y_{ref} - y_k\right)$ indicates the distance of the controlled variable with respect to the reference while the second term ($\Delta e_k = y_{k-1} - y_k$) indicates whether the variable is converging to or diverging from the reference point. The latter depends on the first term as for the same value of second term ($\Delta e_k > 0$), the controlled variable is said to be diverging if ($e_{k_{ref}} < 0$) and converging if ($e_{k_{ref}} > 0$). Therefore, if the process output y_k is much below the reference y_{ref} (e_k is *PB*) and it is diverging from the reference-point with a small step (Δe_k is *PS*) then the magnitude of this step has to be significantly increased (Δu_k is *PB*). This point corresponds to quadrant I. The rule corresponding to this case in Table 3-1 is defined by the intersection of the last row and the fifth column and it is read as follows:

if e_k is *PB* and Δe_k is *PS then* Δu_k is *PB*

When the point belongs to the quadrant III, that is, if y_k is much above the reference y_{ref} (e_k is *NB*) and it is diverging from the reference-point with a quite large step (Δe_k is *NM*) then the magnitude of this step has to be significantly decreased (Δu_k is *NB*). The corresponding rule is represented as follows:

if e_k is *NB* and Δe_k is *NM then* Δu_k is *NB*

In the second quadrant, if y_k is much above the reference y_{ref} (e_k is *NB*) but it is converging to the reference-point with a small step (Δe_k is *PS*) then the magnitude of this step may be decreased (Δu_k is *NM*). This rule is written as follows:

if e_k is *NB* and Δe_k is *PS then* Δu_k is *NM*

By approaching the desired point $(0, 0)$, the decision determines the smoothness of the system response. If the error and the change of error have different signs assuming that (e_k is *PS*) and (Δe_k is *NS*). In this case, the variable is slightly below the reference point and converging to it, the change of control variable can by zero to avoid overshoots. The rule will be:

if e_k is *PS* and Δe_k is *NS then* Δu_k is *ZE*

By analyzing all fuzzy values of the error and the change of error, the rule base shown in Table 3-1 can be obtained. Based on setting these rules, Figure 3-24 (b) (c), and (d) shows respectively the simulated plot of the voltage's and current's error-change versus the error in the closed-loop system after the normalization. The figure shows the trajectory of $(\Delta e, e)$ until reach the origin point of the system axes. This point is the desired operating point after reference change or the occurrence of any disturbance to the system. However, the trajectory shows also that the convergence is not straightforward as shown in Figure 3-24 and some oscillations are observed.

Table 3-1 *Fuzzy rule base for fuzzy controller.*

Δe / e	NB	NM	NS	ZE	PS	PM	PB
NB	NB	NB	NB	NB	NM	NS	ZE
NM	NB	NB	NB	NM	NS	ZE	PS
NS	NB	NB	NM	NS	ZE	PS	PM
ZE	NB	NM	NS	ZE	PS	PM	PB
PS	NM	NS	ZE	PS	PM	PB	PB
PM	NS	ZE	PS	PM	PB	PB	PB
PB	ZE	PS	PM	PB	PB	PB	PB

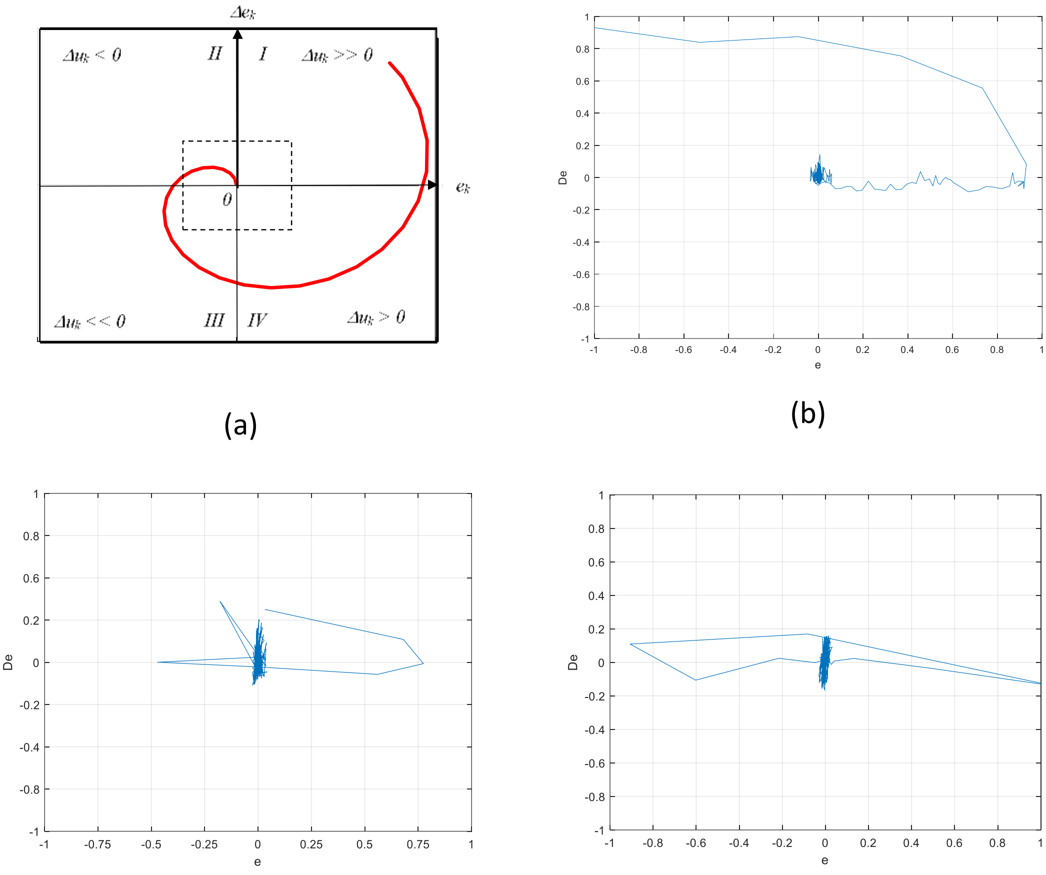

(a) (b)

(c) (d)

Figure 3-24 *(a) Fuzzy rule determination based on phase plane trajectory, (b) Δe versus e in the closed-loop system of the PI-FLC used to regulate* V_{dc} *, (c) Δe versus e for the current controller in d axis , (d) Δe versus e for the current controller in q axis.*

3.11 Conclusion

This chapter has been mainly devoted to the multi-functional inverter control based on PI-like fuzzy logic controller. First, we started with a state of the art where we have summarized the work completed in the literature of multi-functional inverter control strategies. Subsequently, the principle and the operation of each stage of the proposed control satisfying all the functions were explained. Finally, a deep analysis has been given to the proposed PI-like FLC.

In the next chapter, the validation of the proposed system will be tested using STM32F4 Discovery board through a processor-in-the-loop (PIL) test.

Chapter 4: Contribution to Preventive Solution for Harmonic Pollution Control in Grid-tied PV System: Processor-in-the-loop Test Validation

4.1 Introduction

In such field of research, many types of validation can be performed i.e. (Simulation, Software-in-the-loop (SIL), Processor-in-the-loop (PIL), Hardware-in-the-loop (HIL), Hardware implementation…etc.). Each type has its purpose depending on the application; however, these types of validation can come in hierarchical steps starting from the simulation to end-up with reliable and safe hardware implementation.

In this chapter, the Simulink model is configured to perform the PIL test using STM32F4 discovery board for our multi-functional inverter, the purpose of this test is perform the hardware verification of the inverter control algorithm using a low-cost STM32F4 discovery board. Therefore, the control part of the system is replaced with the created PIL block and lunched into the STM32F4 board using the target's compiler and embedded coder tool. The obtained results of the proposed system have been presented in detail under steady state and dynamic conditions. Finally, a comparative study has been established over the conventional PI controller and other proposed controllers in order to show the superiority of the proposed PI-FLC controller.

4.2 PIL test structure using STM32F4 board for system validation

In order to evaluate the performance of the proposed multi-functional three-level T-type inverter through PIL test, the electrical power circuit that corresponds to Figure 4-1 was modelled using Matlab/Simulink software while the control part of the system was implemented in the STM32F4 board. The specifications of the system and its design parameters are reported in Appendix C Table C-1.

The PIL test aims to create the PIL block in Simulink/Matlab and lunch it in the STM32F4 board. In each iteration step of the simulation, PV array voltage and current (V_{pv}, I_{pv}), PCC voltages (v_a, v_b, v_c), AC side inverter currents (i_{Fa}, i_{Fb}, i_{Fc}), and the nonlinear load currents (i_{La}, i_{Lb}, i_{Lc}) values are sent to the board as an input information. While duty cycle of the inverter pulsation ($S_{a1}, S_{a2}, S_{b1}, S_{b2}, S_{c1}, S_{c2}$) are read from the board and applied to the Simulink model.

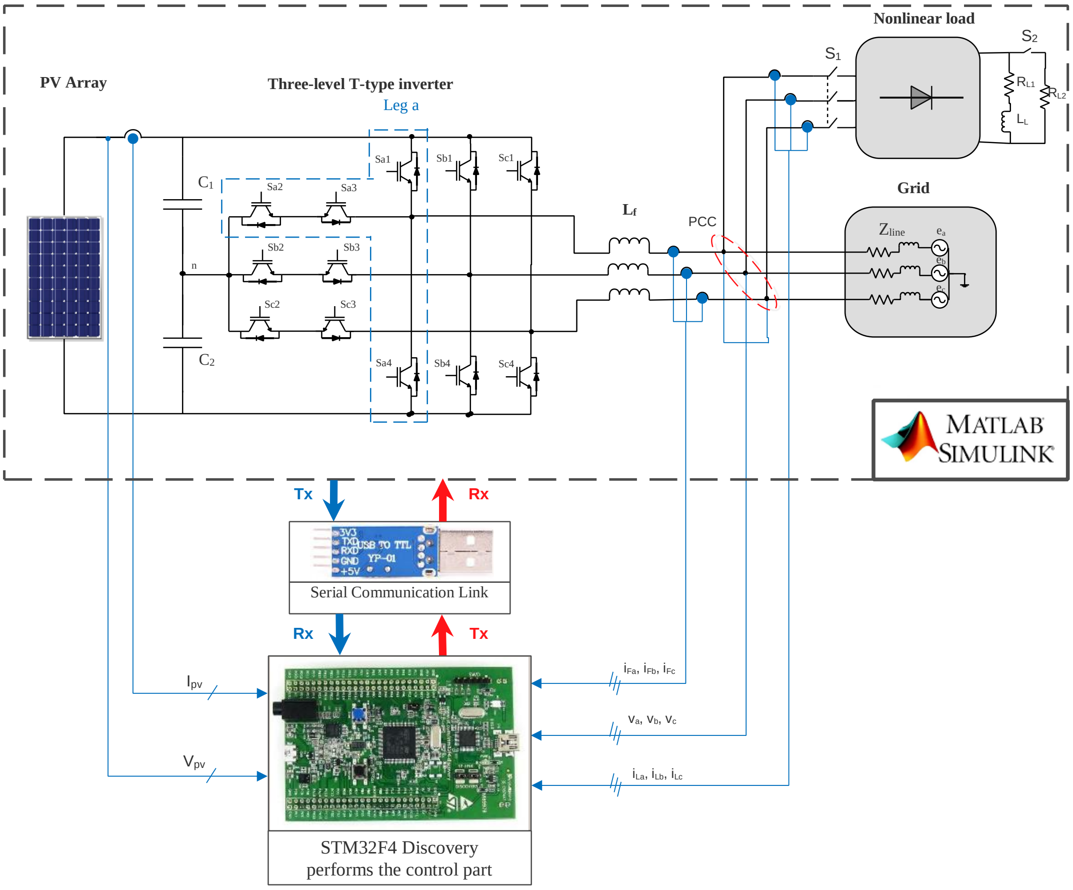

***Figure 4-1** PIL test structure of the multi-fuctional inverter using SM32F4 board.*

The communication between the Simulink/Matlab and the board is established using communication serial link (*USB-TO-TTL YP-01*) through UART (Universal Asynchronous Receiver Transmitter) communication protocol. In our case, the communication was achieved using the *UART2* unit where *PA3* and *PA2* pins were set as receive (*Rx*) and transmit (*Tx*) pins, respectively. The Serial communication is configured with one stop bit, no parity bit, 8-bit data and 9600 bps (bit per second).

The configuration steps of the *PIL* test using the STM32F4 board in Matlab/Simulink are illustrated in detail in Appendix D.

In our work, the PIL test was undertaken to verify and validate all the functions of the inverter control: maximum power extraction capability, harmonics mitigation, reactive power compensation and the robustness of the proposed PI-like FLC.

4.3 Dynamic power flow assessment

Throughout the testing, different perturbations in the system have been considered, variation of solar irradiance and load demand. The irradiance variation profile is shown in Figure 4-2 (A) while the load demand profile is given Figure 4-3 (green line). Figure 4-2 (B) shows the maximum power extracted from the PV array with respect to the irradiance level and Figure 4-2 (C) illustrates the inverter DC side voltage including the voltages across the split capacitors. The power flow that exchanged between the three elements (PV system, grid, and Nonlinear load) is demonstrated in Figure 4-3 for the entire simulation time.

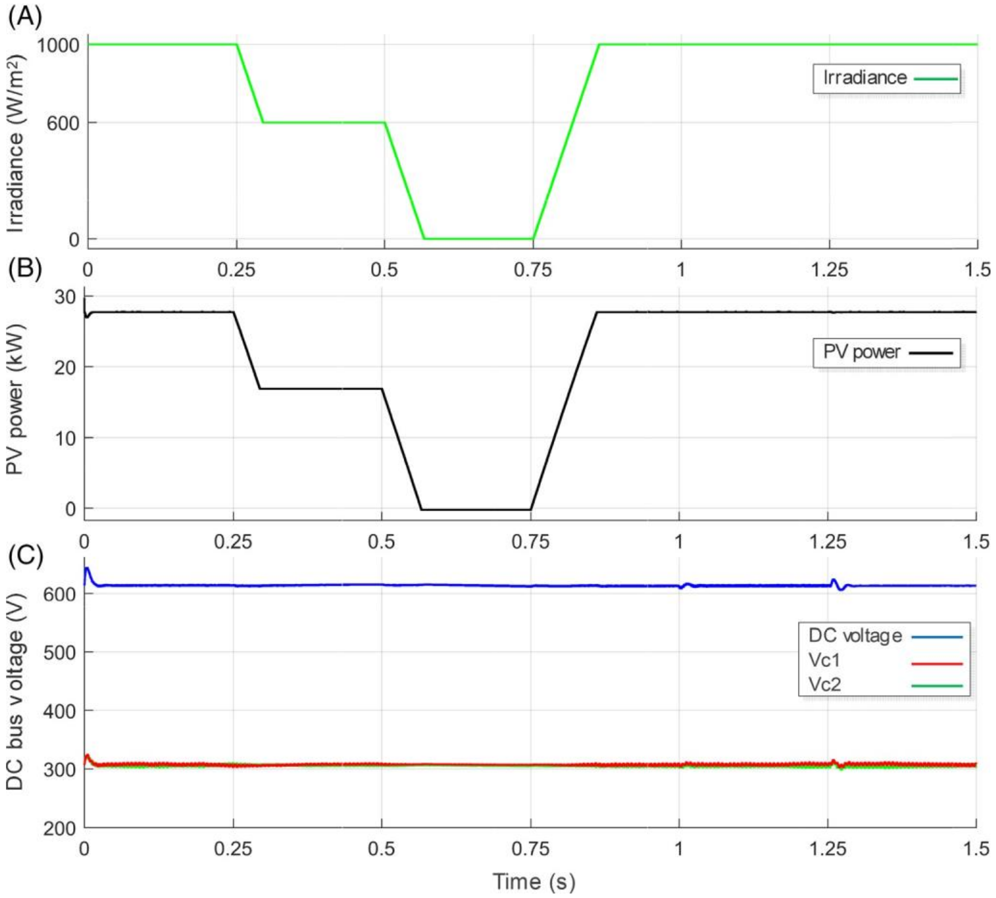

Figure 4-2 *(A) Irradiance profile, (B) PV array output power, (C) Inverter DC side voltage.*

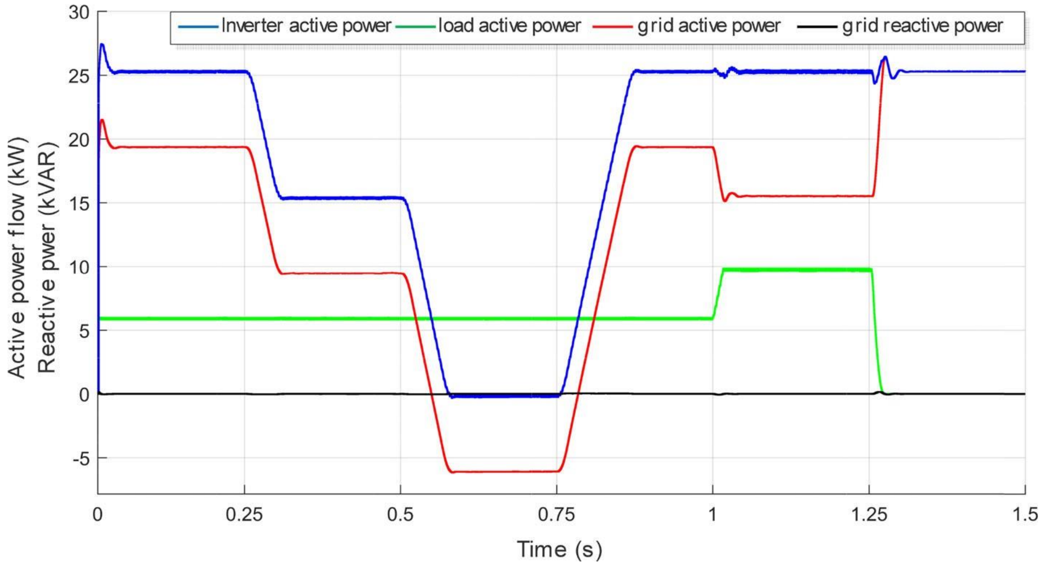

***Figure 4-3** Power flow at PCC.*

Thus, different scenarios along the simulation period are assessed in details as follows:

1. From initial time until $\mathrm{t} = 0.25\mathrm{s}$, the PV system operates at STC ($1000\ \mathrm{W/m^2}, 25\ \mathrm{C°}$) and the nonlinear load is initially connected to the PCC where switch S_1 is close and S_2 is open (See Figure 4-1). The maximum PV output power in this case is $27.74\ kW$ while the maximum point DC voltage is about $613.7\ V$ as depicted in Figure 4-2. According to Figure 4-3, within this condition, the inverter output power of $25.31\ kW$ is feeding the nonlinear load of $5.97\ kW$ and the surplus of this power about $19.37\ kW$ is injected to the grid (*Given that: the positive sign of the grid power indicates that the power is being transferred from the PCC to the grid*). The value of the grid current in this condition is equal to $45.56\ A$ with THD of 1.05% as it is demonstrated in Figure 4-4 (a).
2. From $t = 0.25s$ to $t = 0.5s$, the irradiance is decreased to $600\ W/m^2$ with a fixed ramp while the temperature is set to be constant at $25\ C°$ during the entire simulation period. Consequently, the PV power is reduced to $16.88\ kW$ while the DC voltage becomes $612\ V$. The DC voltage level has not changed significantly, simply because the maximum point voltage is affected by the temperature change mostly. This condition is performed to verify the effectiveness of the proposed IncCond MPPT algorithm. The IncCond MPPT controller determines the appropriate inverter current reference matching the irradiation level (${I_{MP}}^*$), and therefore forcing the inverter to extract the maximum PV output power

accordingly. The power flow in this condition has the same behaviour as the first condition however with a lower power rate where a $15.42\ kW$ inverter output power is supplied to the nonlinear load for the same power demand, and the rest is injected to the gird as illustrated in Figure 4-3. In this case, the grid current is equal to $22.24\ A$ with THD of 1.43% as it is shown in Figure 4-4 (b).

3. From $t = 0.5s$ to $t = 0.75s$, there is no power generated from the PV system where the irradiance level is reduced to $0\ W/m^2$. As explained before the inverter in this case will get the energy from the grid to maintain the voltage at the desired reference value that is $613\ V$ as shown in Figure 4-2 (C). Moreover, it is noticed that the DC capacitors' voltage is well balanced, and this, for any case during the operation. From Figure 4-3, it can be seen that the full demand of the nonlinear load is supplied only by the utility grid (*hence the grid output power is negative*). Therefore, the proposed inverter acts only as a shunt active power filter in this case. The drawn current from the grid in this case equals 14.56 A with THD of 2.56% (Figure 4-4 (c)).

The two following scenarios are simulated to test the system viability under load variation. Meanwhile, the PV system is back to operates at STC during these conditions.

4. At $t = 1s$, switch S_2 is switched on and the load demand is suddenly increased from $5.97\ kW$ to $9.78\ kW$. As can be noticed from Figure 4-3 the PV system keeps supplying the same amount of power to satisfy the power demand and the rest is injected to the grid. In this case, the grid current equals to $36.5\ A$ with THD of 1.88% (Figure 4-4 (d)).
5. At $t = 1.25s$ the load is disconnected completely from the system where S_1 is opened here. Therefore, the total power produced from the PV system will be injected fully into the grid as clearly demonstrated in Figure 4-3. The grid current here equals $59.34\ A$ which is the maximum current the grid can get from the PV system with THD of 0.75% (Figure 4-4 (e)).

4.4 Power quality assessment

After the assessment of the power flow, a detailed analysis of the power quality in terms of *THD* and unity power factor operation will be performed herein.

The reactive power of the utility grid is null during the whole operation as shown in Figure 4-3 (black line). This corresponds to unity power factor operation of the grid-connected system. Figure 4-4 can also confirm the unity power factor operation as the grid current is totally in phase with the voltage when the grid acts as a receiving end (Figure 4-4 (a), (b), (d), (e)) and in opposite phase when the grid behaves like a sending end (Figure 4-4 (c)).

As far as the harmonic content is concerned for power quality aspect, *FFT* analysis of the grid current is performed. Figure 4-4 also shows the harmonic representation as well as the *THD* value of the grid current in each scenario.

The results demonstrate that the proposed multi-functional inverter can effectively compensate both the reactive power and the harmonics that are required by the nonlinear load. This allows to meet international stander requirements that state the *THD* of the grid current should be less than 6.5% according to IEC 61000-3-6 standard while operating at unity power factor.

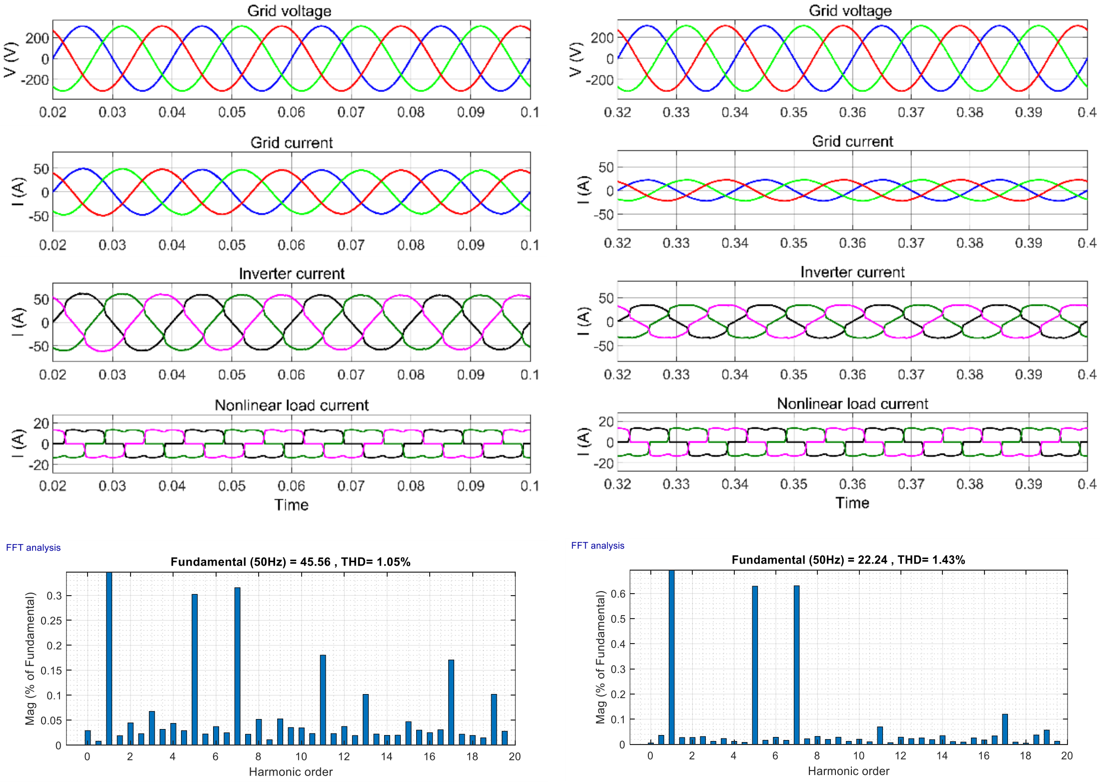

(a) (b)

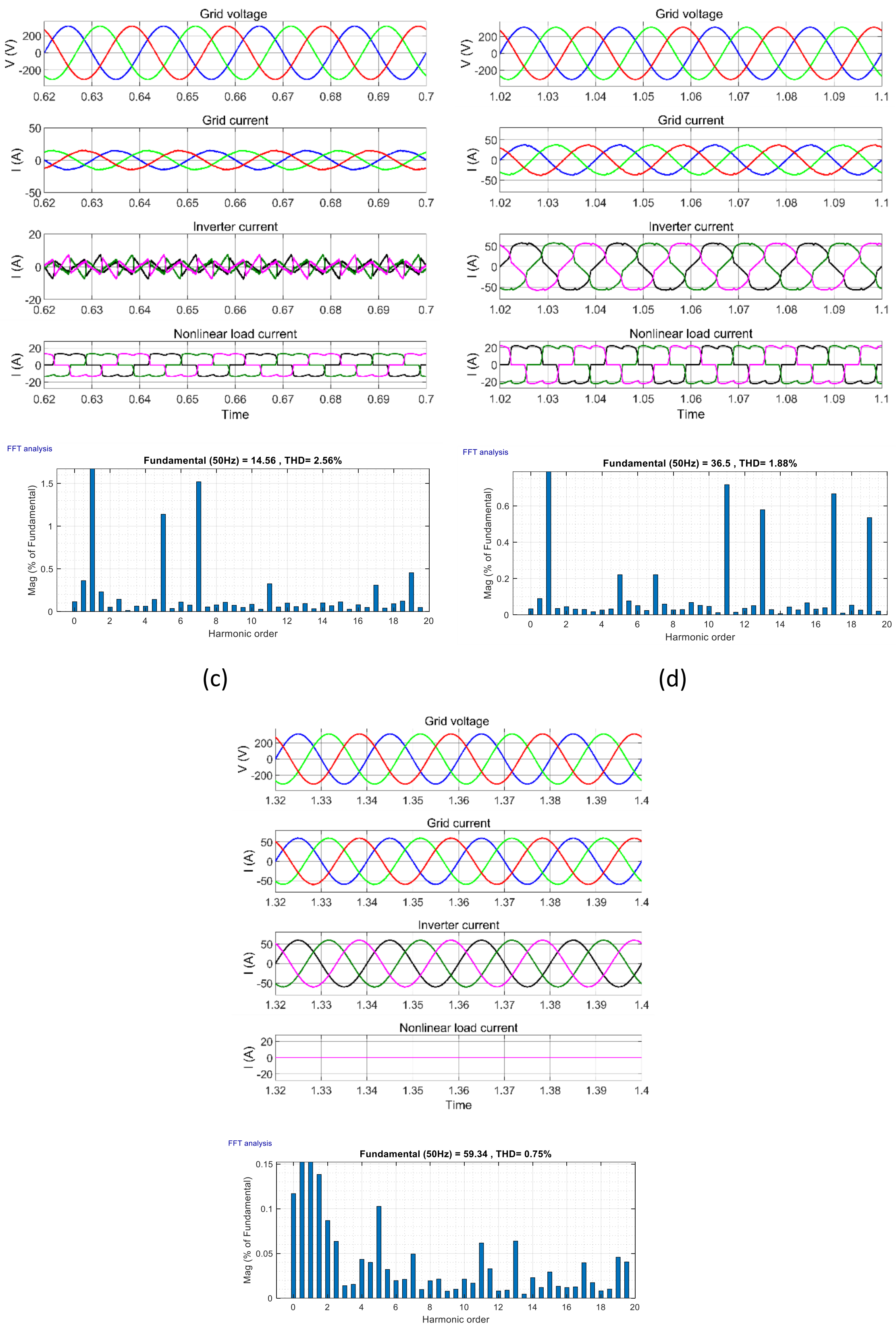

(c)

(d)

(e)

Figure 4-4 *Demonstration of grid voltage, grid current, inverter current, nonlinear current, and the FFT analysis of the grid current for each scenario.*

4.5 Control Signal Generation

In this part, we try to visualize what is going on inside the control block and analyse each signal separately.

Figure 4-5 (A) and (D) show respectively the instantaneous real power p_L and the imaginary power q_L that drawn by the nonlinear load. This power is calculated using p-q theory as explained in section 3.6.2. The real power p_L is composed of average $\bar{p}_L$and oscillating $\tilde{p}_L$ parts. The oscillating part $\tilde{p}_L$ is the energy flowing per time unity that normally produces a zero-average value as shown in Figure 4-5 (C) which represents all the undesirable current harmonics. Therefore, Figure 4-5 (C) and (D) illustrate the undesirable power drawn by the nonlinear load that should be compensated.

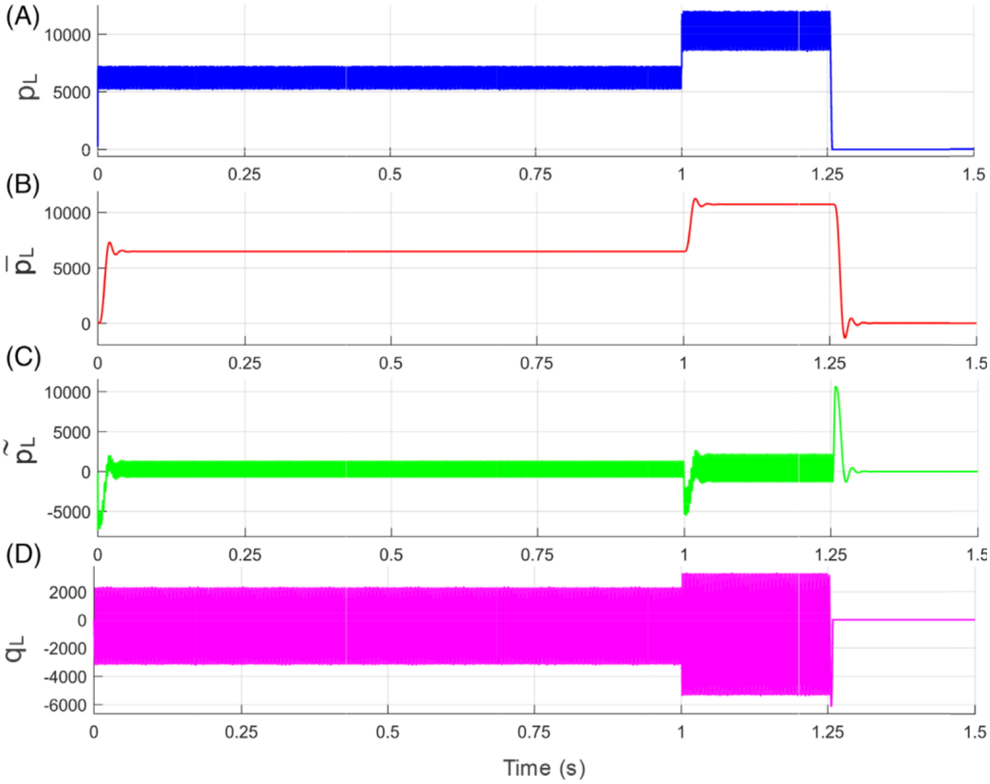

Figure 4-5 *(A) Real power absorbed by the nonlinear load, (B) average power, (C) oscillating part the real power, (D) nonlinear load reactive power.*

Figure 4-6 shows the inverter current references in DC component (*dq coordinates*), where $i_{Fd}{}^{*}$ represents the fundamental component reference provided by MPPT algorithm ($I_{MP}{}^{*}$) corresponding to the irradiance level plus the compensating current harmonics ($i_{cd}{}^{*}$), and $i_{Fq}{}^{*}$ is the reference current that is dedicated to componsate the reactive power.

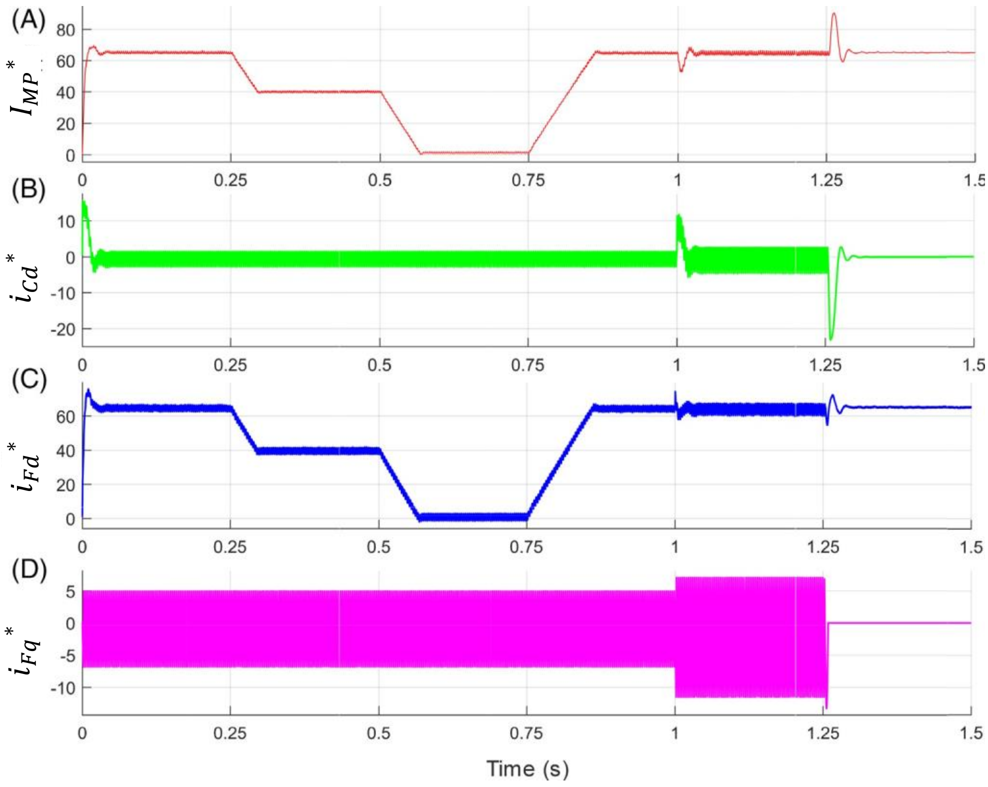

Figure 4-6 *(A) Reference current generated by IncCon MPPT algorithm, (B) reference current for harmonic compensation, (C) total d component of the inverter current reference, (D) q component of the inverter current reference for reactive power compensation.*

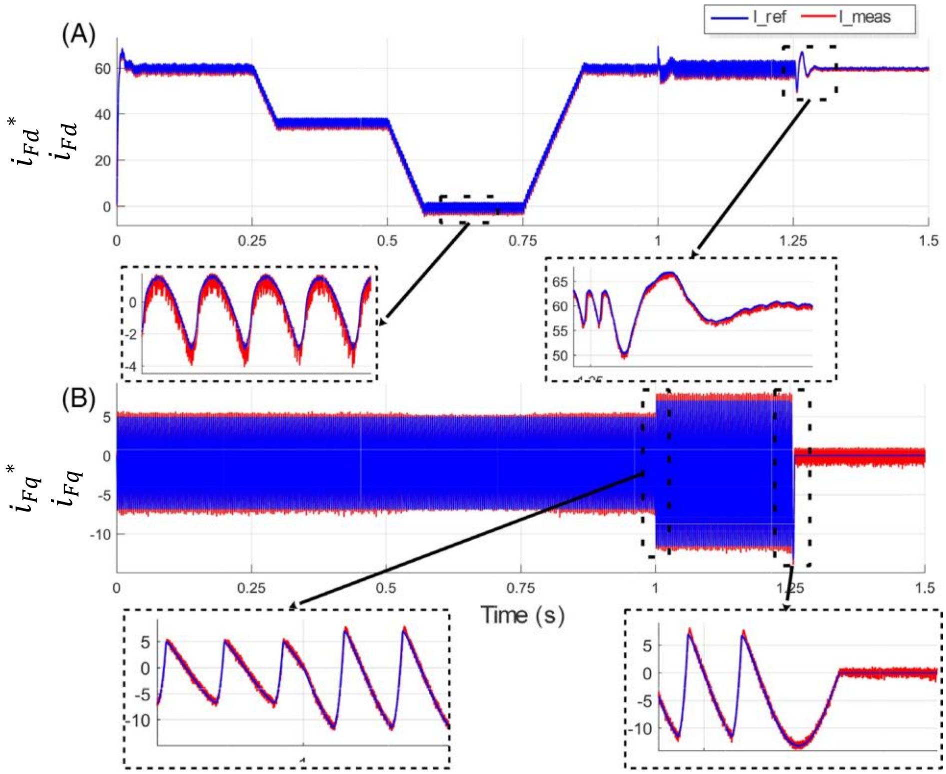

Figure 4-7 *Inverter current tracking in dq frames.*

Furthermore, in Figure 4-7, it is clearly show that the proposed control forces the inverter to tracks perfectly the *dq* reference currents, during steady and dynamic states.

To clearly demonstrate the M-SVPWM operation, Figure 4-8 (A) and (B) demonstrate respectively the sectors and regions where the voltage vector reference is located during the On-time calculation process. Since $\left|\overrightarrow{V_{ref}}\right|$ and V_{DC} almost constant during the whole operation, and $V_{dc}/3 < \left|\overrightarrow{V_{ref}}\right| < 2V_{dc}/3$, therefore only regions *2*, *3*, and *4* will be depicted for each sector as illustrated in Figure 4-9. Consequently, the three nearest switching states for each region will be selected taking into consideration the redundant switches in order to ensure the DC voltage balance between the capacitors.

The normalized On-times for switches S_{a1}, S_{b1}, S_{c1} with modulation index ($m_a = 0.85$) are exported to Matlab and drawn on the same graph axes as given in Figure 4-8 (C).
The three-phase shifted On-time reference waves are compared with one triangular wave having a carrier frequency of ($f_s = 10\ kHz$) to generate gating signals driving the proposed multi-functional three-level T-type inverter.
Figure 4-8 (D) shows the output line-to-line voltage of the three-level inverter (V_{ab}), where it is noticed that the line-to-line voltage consists of three steps (levels); zero, $V_{DC}/2$ and V_{DC}. The result confirms the effectiveness of the M-SVPWM algorithm in controlling a three-level three-phase T-type inverter.

4.6 PI-FLC robustness

In order to investigate the effectiveness and the robustness of the proposed PI-like FLC, a comparison with the conventional PI controller is performed. The PI parameters are adjusted using the Ziegler-Nichols method in this study. While the PI-like FLC scaling factors are calculated and tuned according to the proposed methodology as explained previously in Section 3.10.

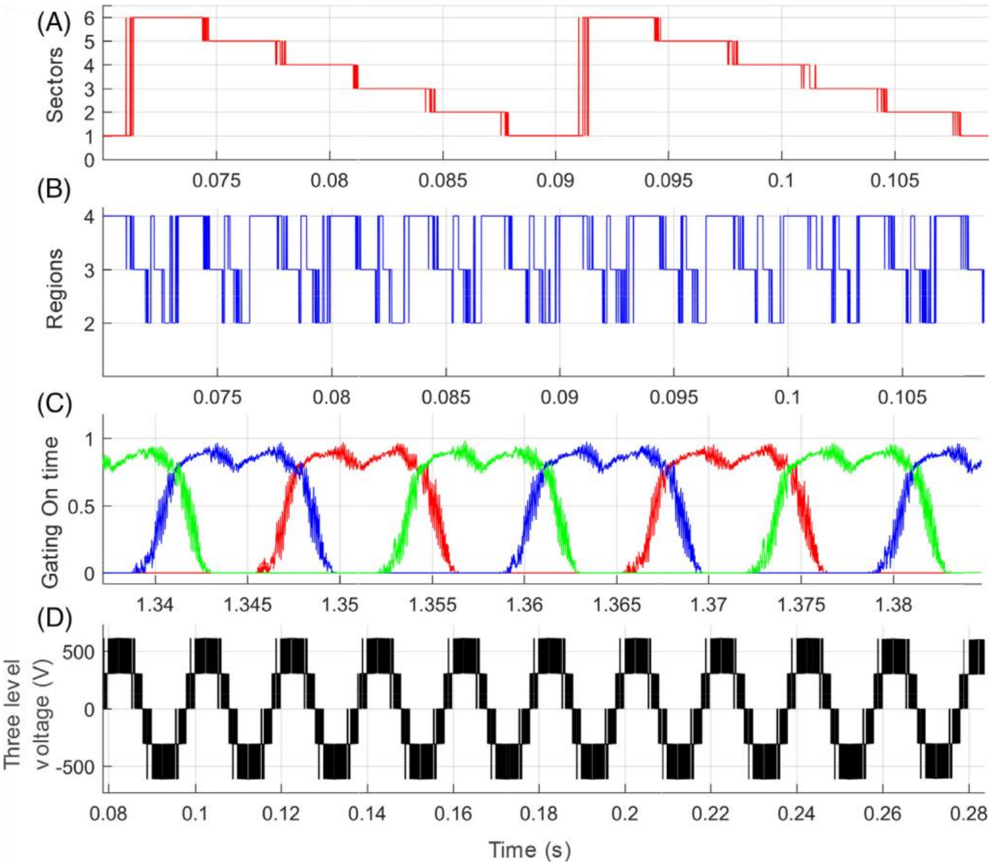

Figure 4-8 *(A) Selected sector according to the $\boldsymbol{V_{ref}}$ location, (B) selected region in each sector, (C) normalized On-time for switches $\boldsymbol{S_{a1}}$, $\boldsymbol{S_{b1}}$ and $\boldsymbol{S_{c1}}$ in the upper arms of phases A, B and C respectively with ($\boldsymbol{m_a = 0.85}$), (D) line-to-line V_{ab} three-level inverter voltage.*

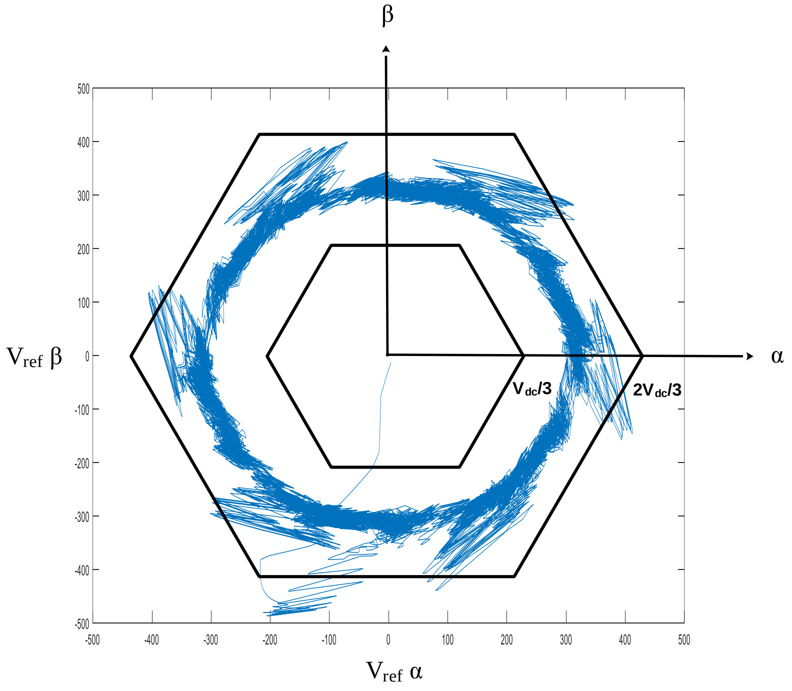

Figure 4-9 *M-SVPWM voltage reference trajectory in αβ coordination.*

All the parameters of the conventional PI and the proposed PI-like FLC scaling factors are listed in Table 4-1.

Table 4-1 *Convetional PI and proposed PI-FLC parameters.*

Control type	**PI**		**PI-FLC**		
	K_p	K_i	G_e	$G_{\Delta e}$	G_u
V_{dc} control	0.8	30	0.05	0.01	80
I_d current control	500	60	0.062	1	1000
I_q current control	1000	90	0.66	10	500

Figure 4-10 and Figure 4-11 show the superiority of using PI-like FLC compared to the conventional PI controller in terms of the dynamic response of the grid active power and DC-link voltage, respectively. It is observed in the zoomed area of the Figure 4-10 that, under different disturbance scenarios, the PI-like FLC offers a fast transient response with low overshoot and short recovery time, comparatively.

Moreover, it is clearly demonstrated in Figure 4-11 that the proposed controller offers excellent maximum point voltage tracking performance during disturbances.

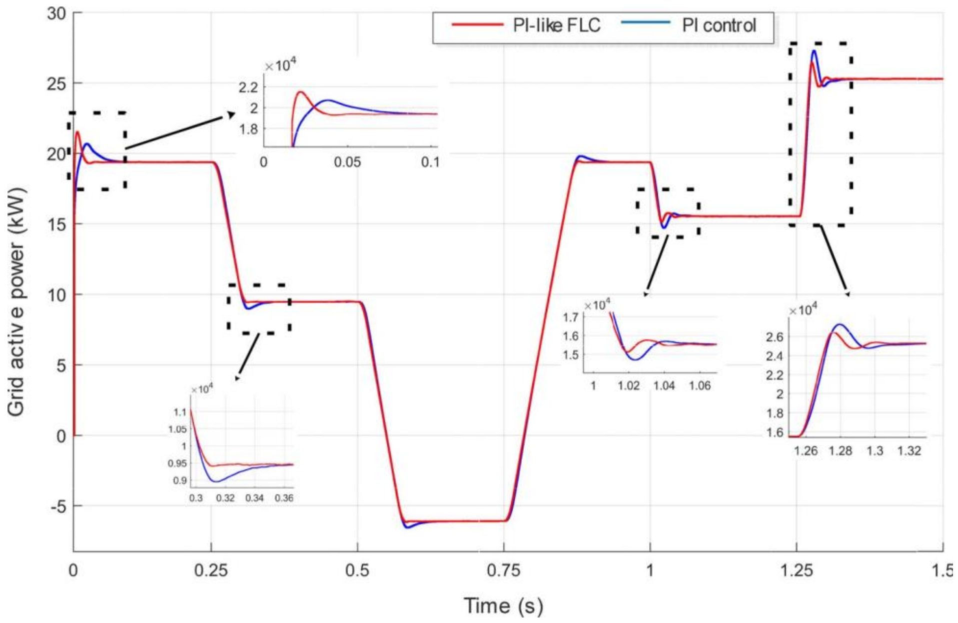

Figure 4-10 *Active power response during different disturbances.*

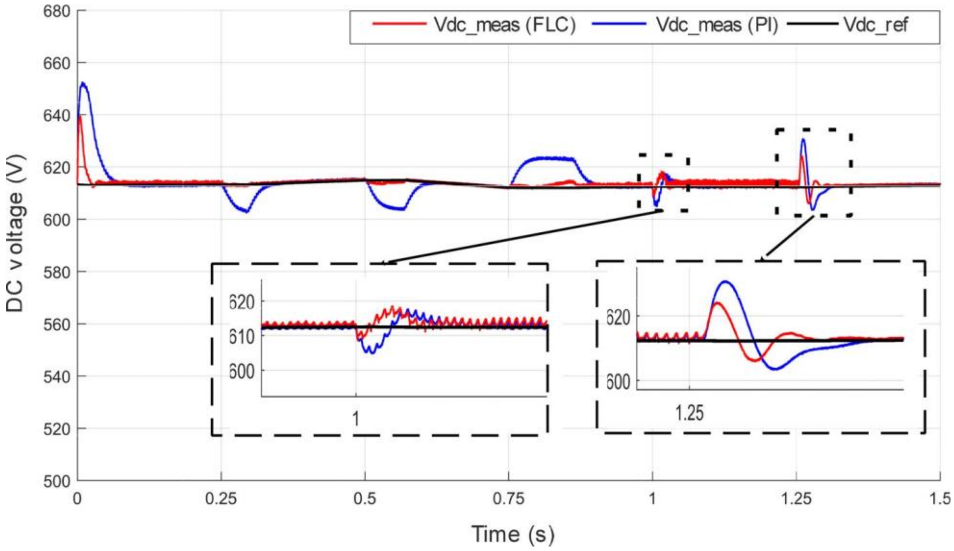

Figure 4-11 *DC-link voltage behavior using PI and PI-FLC.*

Table 4-2 summarizes the response performance characteristics of the current controller, including the rise time (*Tr*), the settling time (*Ts*), the percentage overshoot (*P.O%*), and the FFT analysis of the grid's current (*THD%*) of the two controllers PI and PI-like FLC.

According to the tabulated data, in the dynamic-state condition for either irradiance variation or load rate changing, the proposed controller performs outstandingly with faster response time, shorter settling time, and significantly, lower overshoot compared to the conventional controller. Knowing that in the irradiance variation at $t = 0.25s$, $t = 0.5s$, and $t = 0.75s$ the rise time (*Tr*) and settling time (*Ts*) are calculated taking into consideration the time of the decreasing and increasing of the irradiance ramp.

Table 4-2 *Comarative analysis of system response and power quality using the two controllers.*

Disturbance time	**T_r (ms)**		**T_s (ms)**		**P.O (%)**		**THD_i (%)**	
	PI	**PI-FLC**	**PI**	**PI-FLC**	**PI**	**PI-FLC**	**PI**	**PI-FLC**
t = 0s	9.5	1.3	144	44	6.71	11.04	1.5	1.05
t=0.25s	59	55	110	90	5.38	0.55	2.63	1.43
t=0.5s	80.5	77.5	145	103	7.37	0.95	4.03	2.56
t=0.75s	125	122	190	160	2.27	0.41	1.5	1.05
t=1s	16	15	72	68	5.34	2.64	2.64	1.88
t=1.25s	17	16	90	74	7.95	4.63	0.99	0.75

Once more, FFT has been carried out to calculate the grid current THD for both controllers. From the table, it can be noted that the proposed controller keeps the THD as low as possible irrespective of the different perturbations.

4.7 Comparison between the proposed and other's Work

In this section, the above results will be compared with other works introduced in the literature in terms of system performance. Table 4-3 shows the performance comparison between the proposed approach and relevant systems based on different control strategies. It can be noticed that the proposed PI-FLC offers better performance in terms of response characteristics and low THD of the grid current.

Table 4-3 *Comparison table with other works.*

References	DC voltage controller	Current controller	Harmonic elimination technique	T_s (ms)	P.O (%)	THD (%)
Kumar R. *et al.* [93]	ANFIS	Hysteresis current controller	SRF theory	> 100	N/A	1.98
Singh Y. *et al.* [88]	PI	Hysteresis current controller	Sixth-order generalized integrator	N/A	N/A	2.4
Youcefa B E. *et al.* [154]	Back stepping controller	Back stepping controller	p-q theory	25	N/A	1.55
Demirdelen T. *et al.* [91]	PI	N/A	Selective harmonic extraction	> 50	N/A	1.64
Vigneysh T. *et al.*[100]	AFPI	AFPI	N/A	42	9	1.14
Proposed [155]	PI-like FLC	PI-like FLC	p-q theory	44	2.64	1.05

*N/A: not available

4.8 Conclusion

This chapter was devoted to the validation of the proposed multi-functional inverter and its control strategy through PIL test using a cost-effective STM32F4 board. Considering different perturbations that may happen in the grid-tied PV system, the proposed Three-level T-type multi-functional inverter has shown an effective and robust performance in terms of PV power extraction and power quality improvement through the application of proposed PI-FLC controller. Finally, the proposed PI-like fuzzy logic controller has been compared with the conventional PI controller and other recent control proposals.

General Conclusion and Future Work

1. General conclusion

The objective of this thesis was to study and contribute to the control and modelling of a grid-connected photovoltaic PV system, supplying a non-linear load. After having identified the origins and consequences of the environmental and electrical pollution, different practical solutions were presented, and the choice of a solution based on the principle of active filtering with photovoltaic solar system integration was retained. Our research work then focused on the multi-functional inverter control-command assembly, which we presented in four main parts:

- Extract the maximum of the solar PV power, serving as an auxiliary, clean, and sustainable energy source to satisfy the load demand.
- Decrease the impact of the non-linear load on the electrical network, by eliminating current harmonics and reactive power compensation.
- Enhance further the power quality by mean of three-level T-type inverter based-M-SVPWM switching controlled.
- Improve the dynamic response of the system using PI-like Fuzzy Logic Control.

In this study, a single-stage three-phase grid-tied PV system with active power filtering capability is proposed where the maximum power tracking is ensured without using a chopper interfaced between the PV generator and the inverter. The proposed control strategy can be divided into three hierarchical control blocks. The first control block uses the maximum PV power extraction based IncCond MPPT algorithm and DC bus voltage regulation. The second block uses the instantaneous power theory for reactive power compensation and harmonic filtering, while the last block uses the M-SVPWM to generate the appropriate switching signals to the proposed three-level T-type inverter.

To improve the dynamic response of the system, a fuzzy logic control system is used to regulate the DC voltage as well as the *dq* component of the inverter reference current. A new approach for tuning the fuzzy controller gains and the determination of fuzzy rules has been introduced. The proposed process of gain tuning allows for reducing the long time required by trail-and-error method that is mostly used for the design of fuzzy controllers, the analysis of error trajectory to select the fuzzy decision seems to be a powerful tool and can be investigated further to enhance the performance of fuzzy control.

Considering the different perturbations that may happen in the grid-tied PV system, the proposed PI-like fuzzy controller has shown better performance compared to the conventional controller. Finally, the preventive solution for harmonic pollution Control in Grid-tied PV System was verified and validated using STM32F4 board through a PIL test. The obtained results show that the proposed multi-functional inverter could perform all the functions, maximum power tracking, harmonic mitigation, unity power factor operation, and bidirectional power flow control from and into the grid within the limits of the international standard.

2. Future work

As a perspective aimed at this modest work, a set of points can be treated in the future:

- Suggest other MPPT algorithms for the photovoltaic generator to operate under partial shading effect.
- Consider other possible grid side effects like voltage sag (dip), voltage flicker, and voltage unbalance.
- Investigating on the filter that interfacing between the inverter and PCC by introducing higher order filter like LCL filter due to its advantages such as the ability to operate at lower switching frequency, better attenuation, and lower current ripple; therefore, reducing the cost and size of the coupling filter.
- Investigating of the islanding mode of the system.

References

[1] Y. Zahraoui, M. R. Basir Khan, I. Alhamrouni, S. Mekhilef, and M. Ahmed, “Current status, scenario, and prospective of renewable energy in algeria: A review,” *Energies*, vol. 14, no. 9, 2021, doi: 10.3390/en14092354.

[2] P. Gadonneix, A. Sambo, Z. Guobao, Y. . Kim, J. Teyssen, and J. A. . Lleras, “World Energy Issues Monitor 2020,” 2020. https://www.worldenergy.org/ (accessed May 20, 2020).

[3] “Algerian Ministry of Energy and Mines, MEM. (2011) Renewable Energy and Energy Efficiency Program.” .

[4] A. Zino, “Renewable Energies in Algeria, Arab Climate Resilience initiative: Climate Change Impacts in the Arab Region Towards Sustainable Energy: Resources, Challenges and Opportunities,” *Manama, Bahrain, 06-07 October, 2010*.

[5] C. Hill, M. Such, D. Chen, J. Gonzalez, and W. Grady, “Battery energy storage for enabling integration of distributed solar power generation,” *IEEE Trans. smart grid*, vol. 3, no. 2, pp. 850–857, 2021.

[6] M. A. Eltawil and Z. Zhao, “Grid-connected photovoltaic power systems: Technical and potential problems—A review,” *Renew. Sustain. energy Rev.*, vol. 14, no. 1, pp. 112–129, 2010.

[7] A. Q. Al-Shetwi, M. A. Hannan, K. P. Jern, A. A. Alkahtani, and A. E. P. G. Abas, “Power quality assessment of grid-connected PV system in compliance with the recent integration requirements,” *Electron.*, vol. 9, no. 2, pp. 1–22, 2020, doi: 10.3390/electronics9020366.

[8] R. Beres, X. Wang, F. Blaabjerg, C. L. Bak, and M. Liserre, “A review of passive filters for grid-connected voltage source converters,” *2014 IEEE Appl. Power Electron. Conf. Expo. 2014*, 2014.

[9] B. Singh, K. Al-Haddad, and A. C. Chandra, “A Review of Active Filters for Power Quality Improvement,” *IEEE Trans. Ind. Electron.*, vol. 46, pp. 690–971, 1999.

[10] R. Kumar and H. O. Bansal, “Shunt active power filter: Current status of control techniques and its integration to renewable energy sources,” *Sustain. Cities Soc.*, vol. 42, pp. 574–592, 2018.

[11] R. D. Silveira, S. A. O. da Silva, L. P. Sampaio, and L. B. G. Campanhol, “Comparative static and dynamic analysis of single- and double-stage multifunctional 3-phase grid-tied photovoltaic systems,” *IET Renew. Power Gener.*, vol. 15, no. 5, pp. 990–1004, 2021, doi: 10.1049/rpg2.12083.

[12] Y. L. Zhu, J. G. Yao, and D. Wu, “Comparative study of two stages and single stage topologies for grid-tie photovoltaic generation by PSCAD/EMTDC,” in *APAP 2011 - Proceedings: 2011 International Conference on Advanced Power System Automation and Protection*, 2011, vol. 2, pp. 1304–1309, doi: 10.1109/APAP.2011.6180580.

[13] Y. P. Kumar and B. Ravikumar, “A simple modular multilevel inverter topology for the power quality improvement in renewable energy based green building microgrids,” *Electr. Power Syst. Res.*, vol. 140, pp. 147–161, 2016.

[14] D. Soto and T. C. Green, “A comparison of high-power converter topologies for

the implementation of FACTS controllers," *IEEE Trans. Ind. Electron.*, vol. 49, no. 5, pp. 1072–1080, 2002, doi: 10.1109/TIE.2002.803217.

[15] A. . Stambouli, Z. Khiat, S. Flazi, and Y. Kitamura, "A review on the renewable energy development in Algeria: Current perspective, energy scenario and sustainability issues," *Renew. Sustain. Energy Rev.*, vol. 16, pp. 4445–4460, 2012.

[16] SONALGAZ, "The National Balance of Electricity and Gas 2015; 2015; Volume 15," 2015. https://www.sonelgaz.dz/en/home.

[17] Creg.dz, "Commission for Regulation of Electricity and Gas.," *Program Indicative of the Requirements for Means of Production of Electricity (2008–2017).* https://creg.dz/ (accessed Jun. 12, 2020).

[18] "Ministère de l'énergie et des Mines. Guide des Energies Renouvelables 2007.," 2007. https://www.energy.gov.dz/articlecontact (accessed May 26, 2020).

[19] Y. Himri, A. . Malik, A. . Stambouli, S. Himri, and B. Draoui, "Review and use of the Algerian renewable energy for sustainable development," *Renew. Sustain. Energy Rev.*, vol. 13, pp. 1584–1591, 2009.

[20] A. . Stambouli and H. Koinuma, "A primary study on a long-term vision and strategy for the realisation and the development of the Sahara Solar Breeder project in Algeria," *Renew. Sustain. Energy Rev.*, vol. 16, pp. 591–598, 2012.

[21] "Administration USEI. Country Analysis Executive Summary: Iran," 2019. https://www.eia.gov/international/content/analysis/countries_long/Iran/pdf/iran_exe.pdf (accessed Jun. 12, 2020).

[22] "Africa Energy Series. Algeria Special Report; 2020." www.africaoilandpower.com/ (accessed May 20, 2020).

[23] M. N. Kraimia and M. Boudour, "Harmonic Impedance Response of Electrical Algerian Network," *Proc. Alger. Large Electr. Netw. Conf. CAGRE 2019*, no. 1, pp. 83–88, 2019, doi: 10.1109/CAGRE.2019.8713174.

[24] M. N. KRAIMIA, M. ZELLAGUI, and M. BOUDOUR, "Harmonic Power Flow Calculations for Algerian Electric Transmission System with Multiple Non Linear Loads," *Alger. Large Electr. Netw. Conf. to Electr. Networks Futur. CIGRÉ 2015 Alger. Conf. Hilton-Algiers-Algeria Algiers*, no. April 2019, 2015.

[25] S. O. Amrouche *et al.*, "Distributed photovoltaic systems in Algeria and control of DC-DC converters for grid integration - An overview," *Energy Procedia*, vol. 136, pp. 356–361, 2017, doi: 10.1016/j.egypro.2017.10.289.

[26] S.BOUCHAKOUR, A.CHOUDER, F.CHERFA, K.ABDELADIM, and K.KERKOUCHE, "The First Grid-Connected Photovoltaic System in Algeria : Power Quality Observation," *2èmes Journées Int. sur les Energies Renouvelable le Développement Durable*, no. June, pp. 1–8, 2012.

[27] S. Bouchakour, K. Abdeladim, F. Cherfa, and A. H. Arab, "Pv systems and power quality in algerian distribution grid," *29th Eur. Photovolt. Sol. Energy Conf. Exhib.*, no. November, pp. 1–5, 2014, doi: 10.13140/2.1.1725.4080.

[28] "Photovoltaic cell." https://energyeducation.ca/encyclopedia/Photovoltaic_cell (accessed Mar. 11, 2021).

[29] ABB, "Technical Application Papers No.10 Photovoltaic plants," 2014.

[30] R. F. Habbati Bellia, “A detailed modeling of photovoltaic module using MATLAB,” *NRIAG J. Astron. Geophys.*, vol. 3, no. 1, pp. 53–61, 2014.

[31] M. Saida and K. Aissa, “Bond graph based modeling for parameter identification of photovoltaic module,” *Energy*, vol. 141, pp. 1456–1465, 2017, doi: https://doi.org/10.1016/j.energy.2017.11.077.

[32] K. Ishaque, Z. Salam, and G. Lauss, “The performance of perturb and observe and incremental conductance maximum power point tracking method under dynamic weather conditions,” *Appl. Energy*, vol. 119, pp. 228–236, 2014.

[33] J. Ahmed and Z. Salam, “An improved perturb and observe (P&O) maximum power point tracking (MPPT) algorithm for higher efficiency,” *Appl. Energy*, vol. 150, pp. 97–108, 2015.

[34] R. Ika, S. Wibowo, and M. Rifa, “Maximum power point tracking for photovoltaic using incremental conductance method,” *Energy Procedia*, vol. 68, pp. 22–30, 2015.

[35] K. S. Tey and S. Mekhilef, “Modified incremental conductance MPPT algorithm to mitigate inaccurate responses under fast-changing solar irradiation level,” *Sol. Energy*, vol. 101, pp. 333–342, 2014.

[36] X. Xiao, X. Huang, and Q. Kang, “A Hill-Climbing-Method-Based Maximum-PowerPoint-Tracking Strategy for Direct-Drive Wave Energy Converters,” *IEEE Trans. Ind. Electron.*, vol. 63, no. 1, pp. 257–267, 2016.

[37] S. B. Kjær, “Evaluation of the hill climbing and the incremental conductance maximum power point trackers for photovoltaic power systems,” *IEEE Trans. Energy Convers.*, vol. 27, no. 4, pp. 922–929, 2021.

[38] Z. Salam, J. Ahmed, and B. S. Merugu, “The application of soft computing methods for MPPT of PV system: A technological and status review,” *Appl. Energy*, vol. 107, pp. 135–148, 2013.

[39] A. Sandali, T. Oukhoya, and A. Cheriti, “Modeling and design of PV grid connected system using a modified fractional short-circuit current MPPT,” *2014 Int. Renew. Sustain. Energy Conf.*, pp. 224–229, 2014.

[40] M. M. Shebani, T. Iqbal, and J. E. Quaicoe, “Comparing bisection numerical algorithm with fractional short circuit current and open circuit voltage methods for MPPT photovoltaic systems,” *2016 IEEE Electr. Power Energy Conf.*, pp. 1–5, 2016.

[41] C. Boonmee and Y. Kumsuwan, “Implementation of ripple correlation control MPPT for single-phase VSI grid-connected PV systems,” *12th Int. Conf. Electr. Eng. Comput. Inf. Technol*, 2015.

[42] G. Chujia, Z. Aimin, Z. Hang, Z. Chao, and B. Yunfei, “A fuzzy MPPT method for PV array in power system,” *27th Chinese Control Decis. Conf. CCDC 2015*, pp. 5085–5089, 2015.

[43] L. B. Prasad, S. Sahu, M. Gupta, R. Srivastava, L. Mozhui, and D. N. Asthana, “An Improved Method for MPPT using ANN and GA with Maximum Power Comparison Through Perturb & Observe Technique,” *IEEE Uttar Pradesh Sect. Int. Conf. Electr. Comput. Electron. Eng.*, pp. 206–211, 2016.

[44] N. Khemiri, A. Khedher, and M. F. Mimouni, “A sliding mode control approach applied to a photovoltaic system operated in MPPT,” *10th Int. Multi-Conferences Syst. Signals Devices 2013*, pp. 1–6, 2013.

[45] P. Kumar, G. Jain, and D. K. Palwalia, “Genetic Algorithm Based Maximum Power Tracking in Solar Power Generation,” *Int. Conf. Power Adv. Control Eng.*, pp. 1–6, 2015.

[46] H. Renaudineau *et al.*, “A PSO-based global MPPT technique for distributed PV power generation,” *IEEE Trans. Ind. Electron.*, vol. 62, no. 2, pp. 1047–1058, 2015.

[47] P. Kumar, G. Jain, and D. K. Palwalia, “Development of an Improved P&O Algorithm Assisted Through a Colony of Foraging Ants for MPPT in PV System,” *IEEE Trans. Ind. Informatics*, vol. 12, no. 1, pp. 187–200, 2016.

[48] P. Tsawant, P. C. Lbhattar, and C. Lbhattar, “Enhancement of PV System Based on Artificial Bee Colony Algorithm under dynamic Conditions,” *IEEE Int. Conf. Recent Trends Electron. Inf. Commun. Technol*, vol. 1, pp. 1251–1255, 2016.

[49] D. E. Rice, “Adjustable-Speed Drive and Power Rectifier Harmonics. Their Effects on Power System Components,” *IEEE Trans. Ind. Appl.*, vol. 22, no. 1, pp. 161–177, 1986.

[50] J. K. Phipps, J. P. Nelson, and P. K. Sen, “Power Quality and Harmonic Distortion on Distribution Systems,” *IEEE Trans. Ind. Appl.*, vol. 30, no. 2, pp. 476–484, 1994.

[51] A. Acha, V. G. Agelidis, O. Anaya-Lara, and T. J. E. Miller, *Power Electronic Control in Power Systems*. 1st Edition, Newnes, Oxford, 2002.

[52] R. C. Dugan, M. F. McGranaghan, and H. W. Beaty, *Electrical Power Systems Quality*, 2nd Editio. 2004.

[53] R. Redl, P. J. D. Tenti, and W. Van, “Power Electronics’ Polluting Effects,” *IEEE Spectr.*, vol. 34, no. 5, pp. 32–39, 1997.

[54] W. M. Grady and R. J. Gilleskie, “Harmonics and How They Relate to Power Factor,” *Proceeding EPRI Power Qual. Issues Oppor. Conf. (PQA93), San Diego, USA*, 1993.

[55] C. I. Budeanu, “Puissances réactives et fictives,” *Inst. Romain l’Energie, Publ. 27, Bucharest, Rom.*, 1927.

[56] S. Fryze, “Active, Reactive and Apparent Power in Circuits with Non-Sinusoidal Voltage and Current,” *Przegl. Elektrotech*, vol. 7, pp. 193–203, 1931.

[57] A. E. Emanuel, “Apparent and Reactive Powers in Three-Phase Systems, In Search of a Physical Meaning and a Better Resolution,” *Eur. Trans. Electr. Power Eng. ETEP*, vol. 3, no. 1, pp. 7–14, 1993.

[58] M. Depenbrock, “The FBD-Method, A Generally Applicable Tool for Analyzing Power Relations,” *IEEE Trans. Power Syst.*, vol. 8, no. 2, pp. 381–387, 1993.

[59] L. S. Czarnecki, “Scattered and Reactive Current, Voltage, and Power in Circuits with Nonsinusoidal Waveforms and Their Compensation,” *IEEE Trans. Instrum. Meas.*, vol. 40, no. 3, pp. 563–577, 1991.

[60] A. Ferrero and G. Superti-furga, “A New Approach to the Definition of Power Components in Three-Phase Systems Under Nonsinusoidal Conditions,” *IEEE*

Trans. Instrum. Meas., vol. 40, no. 3, pp. 568–577, 1991.

[61] H. Akagi, Y. Kanazawa, and A. Nabae, “Generalized Theory of Instantaneous Reactive Power in Three-Phase Circuits,” *Int. Power Electron. Conf.*, 1983.

[62] IEEE Std 519-1992, “Recommended Practices and Requirements for Harmonic Control in Electric Power Systems,” 1992.

[63] IEC 61000-2-2(1993), “Electromagnetic Compatibility (EMC). Part 2 : Environment. Section 2 : Compatibility Levels for Low-Frequency Conducted Disturbances and Signaling in Public Low-Voltage Power Supply Systems,” 1993.

[64] IEC 61000-3-4(1998), “Electromagnetic Compatibility (EMC). Part 3 : Limits. Section 4 : Limitation of Emission of Harmonic Currents in Low-Voltage Power Supply Systems for Equipment with Rated Current Greater Than 16 A.,” 1998.

[65] IEC 61000-3-2(2000), “Electromagnetic Compatibility (EMC). Part 3 : Limits. Section 2 : Limits for Harmonic Current Emissions (Equipment Input Current Up to and Including 16 A per Phase).,” 2000.

[66] B. Singh, S. Gairola, B. N. Singh, A. Chandra, and K. Al-Haddad, “Multipulse ACDC Converters for Improving Power Quality : A Review,” *IEEE Trans. Power Electron.*, vol. 23, no. 1, pp. 260–281, 2008.

[67] L. Gyugyi and E. C. Strycula, “Active AC Power Filters,” *IEEE/IAS Annu. Meet.*, pp. 529–535, 1976.

[68] N. Mohan, “Active Filters for AC Harmonic Suppression,” *IEEE/PES winter Meet. A77 026-8*, 1977.

[69] M. Grandpierre and B. Trannoy, “A Static Power Device to Rebalance and Compensate Reactive Power in Three-Phase Network : Design and Control,” *Proceeding Annu. Meet. IEEE Trans. Ind. Appl. Soc.*, pp. 127–135, 1977.

[70] H. Akagi, Y. Kanazawa, and A. Nabae, “Instantaneous Reactive Power Compensators Comprising Switching Devises without Energy Storage Components,” *IEEE Trans. Ind. Appl.*, vol. 20, no. 3, pp. 625–630, 1984.

[71] F. Z. Peng, H. Akagi, and A. Nabae, “A Novel Harmonic Power Filter,” *Rec. PESC’88*, pp. 1151–1159, 1988.

[72] H. Akagi, “New Trends in Active Filters for Power Conditioning,” *IEEE Trans. Ind. Appl.*, vol. 32, no. 6, pp. 1312–1322, 1996.

[73] P. Salmerón, J. C. Montaño, J. R. Vázquez, J. Prieto, and A. P. Vallés, “Compensation in Nonsinusoidal, Unbalanced Three-Phase Four-Wire Systems with Active Power Line Conditioner,” *IEEE Trans. Power Deliv.*, vol. 19, no. 4, pp. 1968–1974, 2004.

[74] P. Salmeron and J. R. Vazquez, “Practical Design of a Three-Phase Active Power-Line ´ Conditioner Controlled by Artificial Neural Networks,” *IEEE Trans. Power Deliv.*, vol. 20, no. 2, pp. 1037–1044, 2005.

[75] Y. Hoon, M. A. M. Radzi, M. K. Hassan, and N. F. Mailah, “Neutral-point voltage deviation control for three-level inverter-based shunt active power filter with fuzzy-based dwell time allocation,” *IET Power Electron.*, vol. 10, no. 4, pp. 429–441, 2017, doi: 10.1049/iet-pel.2016.0240.

[76] Y. Hoon, M. A. M. Radzi, M. K. Hassan, and N. F. Mailah, “DC-link capacitor voltage regulation for three-phase three-level inverter-based shunt active power filter with inverted error deviation control,” *Energies*, vol. 9, no. 7, 2016, doi: 10.3390/en9070533.

[77] Y. Hoon, M. A. Mohd Radzi, M. K. Hassan, and N. F. Mailah, “A Dual-Function Instantaneous Power Theory for Operation of Three-Level Neutral-Point-Clamped Inverter-Based Shunt Active Power Filter,” *Energies*, vol. 11, no. 6, 2018, doi: 10.3390/en11061592.

[78] A. Chandra, B. Zingh, B. N. Zingh, and K. Al-Haddad, “An Improved Control Algorithm of Shunt Active Filter for Voltage Regulation, Harmonic Elimination, Power Factor Correction and Balancing of Nonlinear Loads,” *IEEE Trans. Power Electron.*, vol. 15, no. 3, pp. 495–507, 2000.

[79] A. Campos, G. Joos, P. Ziogas, and J. Lindsay, “Analysis and Design of a Series Voltage Unbalance Compensator Based on a Three-Phase VSI Operating with Unbalanced Switching Function,” *IEEE Trans. Power Electron.*, vol. 9, no. 3, pp. 269–274, 1994.

[80] V. B. Bhavaraju and P. Enjeti, “A Fast Active Power Filter to Correct Line Voltage Sags,” *IEEE Trans. Ind. Electron.*, vol. 41, no. 3, pp. 333–338, 1994.

[81] F. Kamran and T. G. Habetler, “Combined Deadbeat Control of a Series-Parallel Converter Combination Used as a Universal Power Filter,” *IEEE Trans. Power Electron.*, vol. 13, no. 1, 1998.

[82] M. Aredes, K. Heumann, and E. H. Watanabe, “An Universal Active Power Line Conditioner,” *IEEE Trans. Power Deliv.*, vol. 13, no. 2, pp. 545–551, 1998.

[83] H. Fujita and H. Akagi, “The Unified Power Quality Conditioner : The Integration of Series and Shunt Active Filters,” *IEEE Trans. Power Electron.*, vol. 12, no. 2, pp. 315–322, 1998.

[84] J. Prieto, P. Salmeron, J. R. Vazquez, and A. Pérez, “A Series-Parallel Configuration of Active Power Filters for VAR and Harmonic Compensation,” *Proceeding Int. Conf. Ind. Electron. IECON’02, Seville, Spain,* vol. 4, pp. 2945–2950, 2002.

[85] Y. Bouzelata, E. Kurt, N. Alt, and R. Chenni, “Design and simulation of a solar supplied multifunctional active power filter and a comparative study on the current-detection algorithms,” vol. 43, pp. 1114–1126, 2015, doi: 10.1016/j.rser.2014.11.095.

[86] R. Noroozian and G. B. Gharehpetian, “An investigation on combined operation of active power filter with photovoltaic arrays,” *Int. J. Electr. Power Energy Syst.*, vol. 46, no. 1, pp. 392–399, 2013, doi: 10.1016/j.ijepes.2012.10.033.

[87] S. Sezen, A. Aktaş, M. Uçar, and E. Özdemir, “Design and operation of a multifunction photovoltaic power system with shunt active filtering using a single-stage three-phase multilevel inverter,” *Turkish J. Electr. Eng. Comput. Sci.*, vol. 25, no. 2, pp. 1412–1425, 2017, doi: 10.3906/elk-1602-381.

[88] Y. Singh, I. Hussain, B. Singh, and S. Mishra, “Implementation of grid interfaced photovoltaic system with active power filter capabilities,” *Int. Trans. Electr. Energy Syst.*, vol. 28, no. 11, pp. 1–13, 2018, doi: 10.1002/etep.2616.

[89] de O. Fernando M, O. da S. Sérgio A, F. R. Durand, L. P. Sampaio, V. D. Bacon, and

L. B. G. Campanhol, “Grid-tied photovoltaic system based on PSO MPPT technique with active power line conditioning,” *IET Power Electron.*, vol. 9, no. 6, pp. 1180–1191, 2016, doi: 10.1049/iet-pel.2015.0655.

[90] A. Safa, E. L. Madjid Berkouk, Y. Messlem, and A. Gouichiche, “A robust control algorithm for a multifunctional grid tied inverter to enhance the power quality of a microgrid under unbalanced conditions,” *Int. J. Electr. Power Energy Syst.*, vol. 100, pp. 253–264, 2018, doi: 10.1016/j.ijepes.2018.02.042.

[91] T. Demirdelen, R. Kayaalp, and M. Tumay, “Simulation modelling and analysis of modular cascaded multilevel converter based shunt hybrid active power filter for large scale photovoltaic system interconnection,” *Simul. Model. Pract. Theory*, vol. 71, pp. 27–44, 2017, doi: 10.1016/j.simpat.2016.11.003.

[92] Electric Schneider, “A Quantitative Comparison of Central Inverters and String Inverters in Utility-Scale Solar Systemsin North America.”

[93] R. Kumar and H. O. Bansal, “Real-time implementation of adaptive PV-integrated SAPF to enhance power quality,” *Int. Trans. Electr. Energy Syst.*, vol. 29, no. 5, pp. 1–22, 2019, doi: 10.1002/2050-7038.12004.

[94] K. Ravinder and H. O. Bansal, “Investigations on shunt active power filter in a PV-wind-FC based hybrid renewable energy system to improve power quality using hardware-in-the-loop testing platform,” *Electr. Power Syst. Res.*, vol. 177, p. 105957, 2019, doi: 10.1016/j.epsr.2019.105957.

[95] S. K. Prince, K. P. Panda, and G. Panda, “Kalman filter variant intelligent control for power quality improvement in photovoltaic active power filter system,” *Int. Trans. Electr. Energy Syst.*, vol. 30, no. 3, pp. 1–22, 2020, doi: 10.1002/2050-7038.12239.

[96] J. A. Cortajarena, O. Barambones, P. Alkorta, and J. Cortajarena, “Sliding mode control of an active power filter with photovoltaic maximum power tracking,” *Int. J. Electr. Power Energy Syst.*, vol. 110, no. December 2018, pp. 747–758, 2019, doi: 10.1016/j.ijepes.2019.03.070.

[97] M. Alaa, E. Alalia, Z. Sabiri, Y. B. Shtessel, and J. Barbota, “Study of a Common Control Strategy for Grid-Connected Shunt Active Photovoltaic Filter without DC / DC converter Study of a common control strategy for grid-connected shunt active photovoltaic filter without DC / DC converter,” *Sustain. Energy Technol. Assessments*, vol. 45, p. 101149, 2021, doi: 10.1016/j.seta.2021.101149.

[98] B. Boukezata, A. Chaoui, J. P. Gaubert, and M. Hachemi, “Power Quality Improvement by an Active Power Filter in Grid-connected Photovoltaic Systems with Optimized Direct Power Control Strategy,” *Electr. Power Components Syst.*, vol. 44, no. 18, pp. 2036–2047, 2016, doi: 10.1080/15325008.2016.1210698.

[99] S. Ouchen, A. Betka, S. Abdeddaim, and A. Menadi, “Fuzzy-predictive direct power control implementation of a grid connected photovoltaic system , associated with an active power filter,” *Energy Convers. Manag.*, vol. 122, pp. 515–525, 2016, doi: 10.1016/j.enconman.2016.06.018.

[100] T. Vigneysh and N. Kumarappan, “Grid interconnection of renewable energy sources using multifunctional grid-interactive converters: A fuzzy logic based approach,” *Electr. Power Syst. Res.*, vol. 151, pp. 359–368, 2017, doi:

10.1016/j.epsr.2017.06.010.

[101] M. Schweizer and J. W. Kolar, “High efficiency drive system with 3-level T-type inverter,” *Proc. 2011 14th Eur. Conf. power Electron. Appl. IEEE*, pp. 1–10, 2011.

[102] S. Mondal, K. Bose, and V. Oleschuk, “Space vector pulse width modulation of three-level inverter extending operation into over modulation region,” *IEEE Trans. Power Electron.*, vol. 18, no. 2, pp. 604–611, 2003.

[103] O. Rosli, R. Mohammed, and S. Marizan, “Comparative study of a three phase cascaded H-bridge multilevel inverter for harmonic reduction,” *TELKOMNIKA Indones. J. Electr. Eng.*, vol. 14, no. 3, pp. 481–492, 2015, doi: 10.11591/telkomnika.v14i3.7949.

[104] J. M. Maza-Ortega, A. Gomez-Exposito, M. Barragan-Villarejo, E. Romero-Ramos, and A. Marano-Marcolini, “Voltage source converter-based topologies to further integrate renewable energy sources in distribution systems,” *IET Renew. Power Gener.*, vol. 6, no. 6, pp. 435–445, 2012.

[105] J. Rodríguez, J. Leon, S. Kouro, and R. Portillo, “The age of multilevel converters arrives,” *IEEE Ind Electron Mag*, vol. 2, no. 2, pp. 28–39, 2008.

[106] Z. Zeng, H. Yang, R. Zhao, and C. Cheng, “Topologies and control strategies of multifunctional grid-connected inverters for power quality enhancement: a comprehensive review,” *Renew Sustain Energy Rev*, vol. 24, pp. 223–70, 2013.

[107] I. Patrao, E. Figueres, F. González-Espín, and G. Garcerá, “Transformer-less topologies for grid-connected single-phase photovoltaic inverters,” *Renew Sustain Energy Rev*, vol. 15, pp. 3423–31, 2011.

[108] N. Prabaharan and K. Palanisamy, “A comprehensive review on reduced switch multilevel inverter topologies, modulation techniques and applications,” *Renew. Sustain. Energy Rev.*, vol. 76, no. March, pp. 1248–1282, 2017, doi: 10.1016/j.rser.2017.03.121.

[109] D. Lalili, E. M. Berkouk, F. Boudjema, T. Lourci, N., Taleb, and J. Petzold, “Simplified space vector PWM algorithm for five-level inverter,” *Eur. Phys. Journal-Applied Phys.*, vol. 40, no. 3, pp. 335–342, 2007.

[110] M. Schweizer and J. Kolar, “Design and implementation of a highly efficient three-level t-type converter for low-voltage applications,” *IEEE Trans. Power Electron.*, vol. 28, no. 2, pp. 899–907, 2013.

[111] N. I. Systems, U. Choi, S. Member, J. Lee, and S. Member, “New Modulation Strategy to Balance the Neutral-Point Voltage for Three-Level,” vol. 29, no. 1, pp. 91–100, 2014.

[112] X. Li, S. Member, S. Dusmez, S. Member, and B. Akin, “A New SVPWM for the Phase Current Reconstruction of Three-Phase Three-level T-type Converters,” *IEEE Trans. Power Electron.*, vol. 31, no. 3, pp. 2627–2637, 2016, doi: 10.1109/TPEL.2015.2440421.

[113] A. Mokhtar, M. Gamal, and S. Masahito, “Design and validation of SVPWM algorithm for thermal protection of T-type threelevel inverters,” *IEEE Int. Telecommun. Energy Conf. (INTELEC), Osaka, Japan*, 2015.

[114] Y. Zhezhi, Y. Lingzhi, P. Hanmei, F. Xi, and D. Dong, “Study of simplified SVPWM

algorithm based on three-level inverter," *2009 IEEE 6th Int. Power Electron. Motion Control Conf. IPEMC '09*, vol. 3, pp. 876–881, 2009, doi: 10.1109/IPEMC.2009.5157508.

[115] D. Zhang, L. Zhang, J. Jiang, J. Li, B. Wang, and Z. Zhou, "Design of T-type three-level energy storage inverter and grid-connected control strategy," *Proc. IECON 2017 - 43rd Annu. Conf. IEEE Ind. Electron. Soc.*, vol. 2017-Janua, no. 1, pp. 1072–1076, 2017, doi: 10.1109/IECON.2017.8216184.

[116] H. W. van der Broeck, H.-C. Skudel, and G. V. Stanke, "Analysis and realization of a pulsewidth modulator based on voltage space vectors," *IEEE Trans. Ind. Appl.*, vol. 24, no. 1, pp. 142–150, 1988, doi: 10.1109/28.87265.

[117] H. Hu, W. Yao, and Z. Lu, "Design and implementation of three-level space vector PWM IP core for FPGAs," *IEEE Trans. Power Electron.*, vol. 22, no. 6, pp. 2234–2244, 2007, doi: 10.1109/TPEL.2007.909296.

[118] S. de Pablo, A. B. Rey, L. C. Herrero, and J. M. Ruiz, "A simpler and faster method for SVM implementation," *Power Electron. Appl. 2007 Eur. Conf.*, no. 1, pp. 1–9, 2007, doi: 10.1109/EPE.2007.4417751.

[119] F. Liu, Y. Zhou, J. Duan, and B. Yin, "Parameter design of a two-current-loop controller used in a grid-connected inverter system with LCL filter," *IEEE Trans. Ind. Electron.*, vol. 56, no. 11, pp. 4483–4491, 2009.

[120] A. Bouafia, J. Gaubert, and F. Krim, "Predictive direct power control of three-phase pulse width modulation (PWM) rectifier using space-vector modulation," *IEEE Trans. Power Electron.*, vol. 25, no. 1, pp. 228–236, 2010.

[121] C. R. Balamurugan, S. P. Natarajan, B. Shanthi, and T. S. Anandhi, "Simulation and dSPACE based implementation of various PWM strategies for a new H-type FCMLI topology," *Int. J. Power Electron. Drive Syst.*, vol. 6, no. 3, pp. 615–624, 2015.

[122] Data Brief Website, "STM32F4Discovery – Discovery Kit with STM32F407VG MCU, pdf file," 2014. http://www.st.com/en/evaluation-tools/stm32f4discovery.html (accessed Apr. 11, 2020).

[123] St.com, "STM32F407-DISCOVERY." https://www.st.com/en/evaluation-tools/stm32f4discovery.html (accessed Nov. 04, 2021).

[124] "Waijung Software," 2017. http://waijung.aimagin.com (accessed Mar. 20, 2019).

[125] A. A. Yacine, H. Farid, K. Aissa, M. Abdeslam, M. Brahim, and L. Youssouf, "Implementation of Modified SVPWM for Three-level Inverter Using STM32F4," *Proc. 2018 3rd Int. Conf. Electr. Sci. Technol. Maghreb, Cist. 2018*, pp. 1–6, 2019, doi: 10.1109/CISTEM.2018.8613592.

[126] Y. Ayachi Amor, A. Kheldoun, B. Metidji, F. Hamoudi, A. Merazka, and Y. Lazoueche, "Design and implementation of three-level T-type inverter based on simplified SVPWM using cost-effective STM32F4 board," *Int. J. Digit. Signals Smart Syst.*, vol. 5, no. 1, p. 20, 2021, doi: 10.1504/ijdsss.2021.112792.

[127] R. Wai, W. Wang, and C. Lin, "High-performance stand-alone photovoltaic generation system," *IEEE Trans. Ind. Electron.*, vol. 55, no. 1, pp. 240–250, 2008.

[128] M. A. Hannan *et al.*, "Advanced Control Strategies of VSC Based HVDC Transmission System: Issues and Potential Recommendations," *IEEE Access*, vol.

1, no. 13, 2018.

[129] X. Chen, Q. Fu, S. Yu, and L. Zhou, “Unified control of photovoltaic grid-connection and power quality managements,” in *Proceedings - 2008 Workshop on Power Electronics and Intelligent Transportation System, PEITS 2008*, 2008, pp. 360–365, doi: 10.1109/PEITS.2008.66.

[130] N. Hamrouni, M. Jraidi, A. Dhouib, and A. Cherif, “Design of a command scheme for grid connected PV systems using classical controllers,” *Electr. Power Syst. Res.*, vol. 143, pp. 503–512, 2017, doi: 10.1016/j.epsr.2016.10.064.

[131] Z. Zeng, H. Li, S. Tang, H. Yang, and R. Zhao, “Multi-objective control of multi-functional grid-connected inverter for renewable energy integration and power quality service,” *IET Power Electron.*, vol. 9, no. 4, pp. 761–770, 2016, doi: 10.1049/iet-pel.2015.0317.

[132] R. Teodorescu, F. Blaabjerg, M. Liserre, and P. . Loh, “Proportional-resonant controllers and filters for grid-connected voltage-source converters,” *IEE Proceedings-Electric Power Appl.*, vol. 153, no. 5, pp. 750–762, 2003.

[133] Z. Yao and L. Xiao, “Control of single-phase grid-connected inverters with nonlinear loads,” *IEEE Trans. Ind. Electron.*, vol. 60, no. 4, pp. 1384–1389, 2013, doi: 10.1109/TIE.2011.2174535.

[134] K. M. Passino, “Intelligent control: an overview of techniques,” in *Perspectives in Control Engineering: Technologies, Applications, and New Directions*, 2001, pp. 104–133.

[135] M. A. Hannan, Z. A. Ghani, M. M. Hoque, P. J. Ker, A. Hussain, and A. Mohamed, “Fuzzy logic inverter controller in photovoltaic applications: Issues and recommendations,” *IEEE Access*, vol. 7, no. c, pp. 24934–24955, 2019, doi: 10.1109/ACCESS.2019.2899610.

[136] H. M. Hasanien and M. Matar, “A fuzzy logic controller for autonomous operation of a voltage source converter-based distributed generation system,” *IEEE Trans. Smart Grid*, vol. 6, no. 1, pp. 158–165, 2015, doi: 10.1109/TSG.2014.2338398.

[137] M. A. Hannan, Z. A. Ghani, M. M. Hoque, and M. S. Hossain Lipu, “A fuzzy-rule-based PV inverter controller to enhance the quality of solar power supply: Experimental test and validation,” *Electron.*, vol. 8, no. 11, 2019, doi: 10.3390/electronics8111335.

[138] H. A. Mosalam, R. A. Amer, and G. A. Morsy, “Fuzzy logic control for a grid-connected PV array through Z-source-inverter using maximum constant boost control method,” *Ain Shams Eng. J.*, vol. 9, no. 4, pp. 2931–2941, 2018, doi: 10.1016/j.asej.2018.10.001.

[139] I. V. Banu, R. Beniugă, and M. Istrate, “Comparative Analysis of the Perturb-and-Observe and Incremental Conductance MPPT Methods,” *8th Int. Symp. Adv. Top. Electr. Eng.*, pp. 23–26, 2013.

[140] H. Akagi, E. H. Watanabe, and M. Aredes, “Instantaneous Power Theory and Applications to Power Conditioning,” in *IEEE PRESS Wiley*, 2017, pp. 111–236.

[141] H. Akagi, Y. Kanazawa, and A. Nabae, “Generalized theory of instantaneous reactive power and its applications,” *Trans. IEE-Japan, Part B*, vol. 103, no. 7, pp. 483–490, 1983.

[142] H. Akagi, Y. Kanazawa, and A. Nabae, “Generalized theory of the instantaneous reactive power in three-phase circuits,” *IPEC’83—International Power Electron. Conf. Tokyo, Japan*, pp. 1375–1386, 1983.

[143] H. Akagi, Y. Kanazawa, and A. Nabae, “Instantaneous reactive power compensator comprising switching devices without energy storage components,” *IEEE Trans. Ind. Appl.*, vol. IA-20, no. 3, pp. 625–630, 1984.

[144] E. Clarke, *Circuit Analysis of A-C Power Systems*. New York: John Wiley & Sons, 1943.

[145] C. Lee, “Fuzzy logic in control systems : Fuzzy Logic Controller, Part I & II,” *IEEE Trans. Syst. Man, Cebernetics*, vol. 20, no. 2, pp. 404–435, 1990.

[146] R. J. Ross, *Fuzzy Logic with Engineering Applications*. McGraw-Hill, 1995.

[147] Y. Song and A. T. Johns, “Applications of Fuzzy Logic in Power Systems, Part 1,” *IEE Power Eng. J.*, 1997.

[148] Y. Song and A. T. Johns, “Applications of Fuzzy Logic in Power Systems, Part 2,” *IEE Power Eng. J.*, pp. 185–190, 1998.

[149] G. C. D. Sousa and B. K. Bose, “A Fuzzy Set Theory Based Control of a Phase-Controlled Converter dc Machine Drive,” *IEEE Trans. Ind. Appl.*, vol. 30, pp. 34–44, 1994.

[150] S. Saetieo and D. A. Torrey, “Fuzzy Logic Control of a Space-Vector PWM Current Regulator for Three-Phase Power Converters,” *IEEE Trans. Power Electron.*, vol. 13, no. 3, pp. 419–426, 1998.

[151] M. N. Cirstea, A. Dinu, J. G. Khor, and M. McCormick, *Neural and Fuzzy Logic Control of Drives and Power Systems*, 1st Editio. Newnes, Elsevier Science, 2002.

[152] L. A. Zedah, “Fuzzy Sets,” *Inf. Control*, vol. 8, pp. 338–353, 1965.

[153] D. Driankov, H. Hellendoorn, and M. Reinfrank, *An introduction to fuzzy control*. Munchen, Germany: Springer Verlag, 1993.

[154] B. E. Youcefa *et al.*, “Backstepping Direct Power Control for Power Quality Enhancement of Grid-connected Photovoltaic System Implemented with PIL Co-simulation Technique,” vol. 74, no. 1, pp. 1–14, 2019.

[155] Y. Ayachi Amor, F. Hamoudi, A. Kheldoun, G. Didier, and Z. Rabiai, “Fuzzy logic enhanced control for a single-stage grid-tied photovoltaic system with shunt active filtering capability,” *Int. Trans. Electr. Energy Syst.*, vol. 31, no. 10, pp. 1–28, 2021, doi: 10.1002/2050-7038.13008.

Appendix A: The three main bodies of IEC standards

- **IEC 61000-2-2**: It establishes the levels of compatibility of harmonic voltages on low voltage public networks and its purpose is to protect equipment connected to the network. The compatibility levels of the individual rates (relative to fundamental) of the harmonic voltages are summarized in Table A-1. This standard limits the THD to 8% up to the 40th rank.
- **IEC 61000-3-2** and **IEC 61000-3-4**: These two standards define the limits of harmonic current emissions for equipment connected to the low-voltage network, the current per phase of which is respectively less than or equal, and greater than 16 A. The objective of these limits is to reduce the impact of harmonic currents on the voltage, in order to respect the compatibility limits set by IEC 61000-2-2. The limits of these emissions are summarized in Table A-2 and Table A-3 respectively for the two standards IEC 61000-3-2 and 3-4. For the latter, the limits are calculated in percent with respect to the fundamental.
- There is also the **IEC 61000-3-6** standard, which limits the emissions of harmonic currents from equipment connected to the medium and high voltage network, as well as the compatibility levels for individual harmonic voltages. This standard sets the THD limited to 6.5%.

Table A-1 *Compatibility levels for individual harmonic voltages on public low voltage networks (IEC 61000-2-2 standard).*

Odd harmonics				**Even harmonics**	
Non-multiples of 3		**multiples of 3**			
Order *h*	THD_{max} (%)	Order h	THD_{max} (%)	Order h	THD_{max} (%)
5	6	3	5	2	2
7	5	9	1.5	4	1
11	3.5	15	0.3	6	0.5
13	3	21	0.2	8	0.5
17	2	> 21	0.2	10	0.5
19	1.5			12	0.2
23	1.5			> 12	0.2
25	1.5				
> 25	$0.2 + 1.3 \times 25/h$				

Table A-2 *Limits of harmonic current emissions (IEC 61000-3-2 standard).*

Odd harmonics		**Even harmonics**	
Order h	Max admissible current (A)	Order h	Max admissible current (A)
3	2.30	2	1.08
5	1.14	4	0.43
7	0.77	6	0.3
9	0.40	$8 \leq h \leq 40$	$0.23 * 8/h$
$\boldsymbol{11}$	0.33		
13	0.21		
$\boldsymbol{15 \leq h \leq 39}$	$0.15 * 15/h$		

Table A-3 *Limits of harmonic current emissions according to IEC 61000-3-4 standard.*

$\boldsymbol{Order\ h}$	$\boldsymbol{THD_{max}}$ **(%)**	$\boldsymbol{Order\ h}$	$\boldsymbol{THD_{max}}$ **(%)**
3	21.6	19	1.1
5	10.7	21	0.6
7	7.2	23	0.9
9	3.8	25	0.8
11	3.1	27	0.6
13	2	29	0.7
15	0.7	31	0.7
17	1.2	33	0.6

Appendix B: Modified SVPWM M-file MATLAB code

```
%% Alpha Beta transformation of the voltage reference
function [valpha,vbeta] = fcn(va,vb,vc)
valpha=2/3*(va-vb/2-vc/2);
vbeta=2/3*(vb*sqrt(3)/2-vc*sqrt(3)/2);
end

%% Voltage reference phase angle
function deta = fcn(vbeta,valpha)
deta=atan2(vbeta,valpha);
end

%% Voltage reference amplitude
function verf = fcn(valpha,vbeta)
verf=sqrt(valpha^2+vbeta^2);
end

%% Sector identification in numbers
function n = SECTOR(deta)
n=0;
if ((deta>=0)&&(deta<pi/3))
n=1;
end
if((deta>=pi/3)&&(deta<2*pi/3))
n=2;
end
if ((deta>=2*pi/3)&&(deta<pi))
n=3;
end
if ((deta>=-pi/3)&&(deta<0))
n=6;
end
if ((deta>=-2*pi/3)&&(deta<-pi/3))
n=5;
end
if ((deta>=-pi)&&(deta<-2*pi/3))
n=4;
end
end

%% Sector identification in phase
function phi = fcn(n,deta)
phi=0;
if (n==1)
    phi=deta;
end
if (n==2)
    phi=deta-pi/3;
end
if (n==3)
    phi=deta-2*pi/3;
end
if (n==6)
    phi=pi/3+deta;
end
if (n==5)
    phi=2*pi/3+deta;
end
if (n==4)
    phi=pi+deta;
end
```

```
%% Region identification
function R = fcn(vref,phi,udc)
R=0;
m=vref/(2/3*udc);
m1=m*2/sqrt(3)*sin(pi/3-phi);
m2=m*2/sqrt(3)*sin(phi);
if (m1<0.5)&&(m2<0.5)&&(m1+m2<0.5)
    R=1;
end
if (m1<0.5)&&(m2<0.5)&&(m1+m2>0.5)
    R=2;
end
if (m1>0.5)
    R=4;
end
if (m2>0.5)
    R=3;
end

%% Dwell times (On-time) calculation for the first sector
function [ta,tb,tc] = fcn(vref,R,phi,udc)
ta=0;
tb=0;
tc=0;
m=vref/(2/3*udc);
k=2/sqrt(3)*m;
if (R==1)
    ta=2*k*sin(pi/3-phi);
    tb=1-2*k*sin(pi/3+phi);
    tc=2*k*sin(phi);
end
if (R==2)
    ta=1-2*k*sin(phi);
    tb=2*k*sin(pi/3+phi)-1;
    tc=1-2*k*sin(pi/3-phi);
end
if (R==3)
    ta=2*k*sin(phi)-1;
    tb=2*k*sin(pi/3-phi);
    tc=2-2*k*sin(pi/3+phi);
end
if (R==4)
    ta=2-2*k*sin(pi/3+phi);
    tb=2*k*sin(phi);
    tc=2*k*sin(pi/3-phi)-1;
end
end

%% PWM firing time of the first sector
function [s1a,s2a,s1b,s2b,s1c,s2c] = fcn(R,ta,tb,tc)
s1a=0;
s2a=0;
s1b=0;
s2b=0;
s1c=0;
s2c=0;
if (R==1)
    s1a=tc/4+ta/4;
    s2a=1/2;
    s1b=tc/4;
    s2b=1/2-ta/4;
    s1c=0;
    s2c=1/2-ta/4-tc/4;
```

```
end
if (R==2)
     s1a=tc/4+ta/4+tb/2;
     s2a=1/2;
     s1b=tc/4;
     s2b=1/2-ta/4;
     s1c=0;
     s2c=ta/4+tc/4;
end
if (R==3)
     s1a=1/2-tc/4;
     s2a=1/2;
     s1b=tc/4+ta/2;
     s2b=1/2;
     s1c=0;
     s2c=tc/4;
end
if (R==4)
     s1a=1/2-ta/4;
     s2a=1/2;
     s1b=0;
     s2b=ta/4+tb/2;
     s1c=0;
     s2c=ta/4;
end
end

%% Extend the operation to the other sectors
function [ps1a,ps2a,ps1b,ps2b,ps1c,ps2c] =
fcn(n,s1a,s2a,s1b,s2b,s1c,s2c)
ps1a=0;
ps2a=0;
ps1b=0;
ps2b=0;
ps1c=0;
ps2c=0;
if (n==1)
   ps1a=s1a;
ps2a=s2a;
ps1b=s1b;
ps2b=s2b;
ps1c=s1c;
ps2c=s2c;
end
if (n==2)
   ps1a=1/2-s2b;
ps2a=1/2-s1b;
ps1b=1/2-s2c;
ps2b=1/2-s1c;
ps1c=1/2-s2a;
ps2c=1/2-s1a;
end
if (n==3)
   ps1a=s1c;
ps2a=s2c;
ps1b=s1a;
ps2b=s2a;
ps1c=s1b;
ps2c=s2b;
end
if (n==4)
   ps1a=1/2-s2a;
ps2a=1/2-s1a;
```

```
ps1b=1/2-s2b;
ps2b=1/2-s1b;
ps1c=1/2-s2c;
ps2c=1/2-s1c;
end
if (n==5)
   ps1a=s1b;
ps2a=s2b;
ps1b=s1c;
ps2b=s2c;
ps1c=s1a;
ps2c=s2a;
end
if (n==6)
   ps1a=1/2-s2c;
ps2a=1/2-s1c;
ps1b=1/2-s2a;
ps2b=1/2-s1a;
ps1c=1/2-s2b;
ps2c=1/2-s1b;
end
end
```

Appendix C: System's parameter

The equivalent DC capacitor of the inverter DC bus is calculated as follows:

$$C_{eq} = \frac{I_{pv}}{2 * \omega * \Delta V_{DC\,rip}} = \frac{45.24}{2 * 314 * 0.05 * 613} = 2400\ \mu F \tag{B1}$$

Where, I_{pv} is the DC-link current, ω is the angular frequency and $\Delta V_{DC\,rip}$ is the maximum peak to peak DC voltage ripple that shouldn't exceed 5%.

The interfacing inductance filter value is given by:

$$L_f = \frac{m_a * V_{DC}}{8 * \alpha * f_s * \Delta i_{g\,rip}} = \frac{0.85 * 613}{8 * 1.2 * 10000 * 0.03 * 46} = 0.0039 \cong 4\ \text{mH} \tag{B2}$$

where m_a is the modulation index (practically, the value of 'm_a' is less than 1), V_{DC} is the DC-link voltage, α is the overloading factor, f_s is the switching frequency and $\Delta i_{g\,rip}$ is the maximum ripple allowed in grid current (about 3%).

Table C-1 *System's parameters.*

PV array	Nbr of panels	126 (SolarWorld SW220)
	PV Open-circuit voltage, V_{oc} at STC	768.6 V
	PV short-circuit current, I_{sc} at STC	48.48 A
	PV MPP voltage, V_{mp} at STC	613.2 V
	PV MPP current, I_{mp} at STC	45.24 A
	PV maximum power, P_{mp} at STC	27.74 kW
Inverter and the attached passive elements	Inverter	3 Level T-type
	Switching frequency, f_s	10 kHz
	PWM Switching control	Space Vector Modulation
	DC-link capacitor, C_1& C_2	2400 µF
	Filter inductance, L_f	4 mH
Utility grid	Grid voltage, V_g (Line to Line RMS)	380 V_{rms}
	Grid frequency, f_g	50 Hz
	Grid short-circuit impedance ratio X/R	7
Uncontrolled three-phase rectifier balanced nonlinear load	R_{L1}	40 Ω
	L_L	1 mH
	R_{L2}	60 Ω
	Switch S_1 initially closed, opens at	1.25 s
	Switch S_2 initially opened, closes at	1 s

Appendix D: PIL Configuration

In order to perform the PIL test we have the following requirements:

Required Package:

- Install the Embedded Coder Support Package for STMicroelectronics Discovery Boards in Matlab.

Required Hardware:

- STMicroelectronics STM32F407G-Discovery Board.
- USB type A to Mini-B cable.
- USB TO TTL YP-01 (serial communication for STM32F4-Discovery board).

To configure the code generation on the STM32F4-Discovery board in our model, go to **Configuration Parameters > Hardware Implementation > Target Hardware pane** and select STM32F4-Discovery. In **Target Hardware Resources** > **PIL** > **PIL communication interface**, select **Serial (USART2)** to choose the communication method for PIL simulations.

In the same pane, enter the COM port of the serial interface on Windows. To do so, open Device Manager in Windows® and copy the COM port number to the Simulink model as shown in Figure D-0-1.

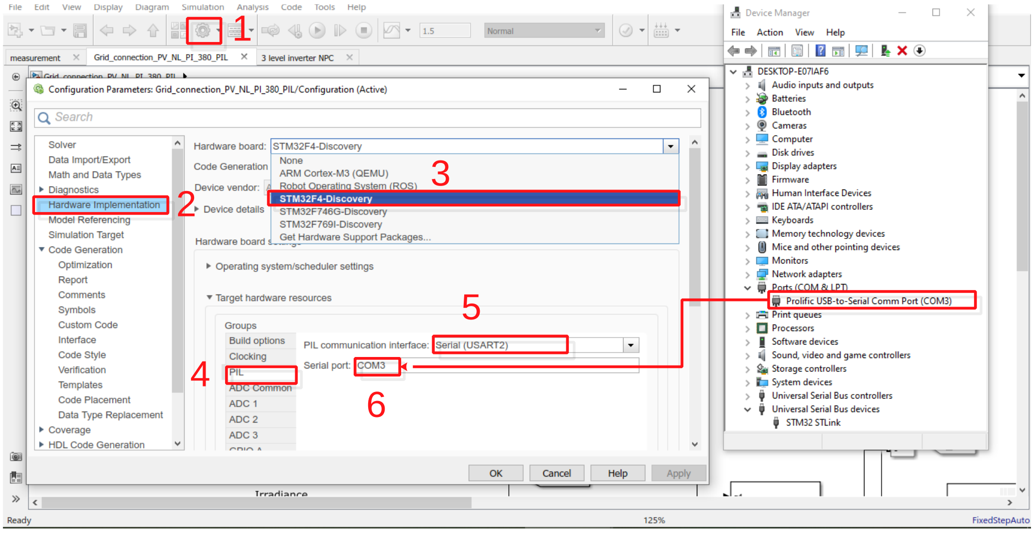
Configuration Parameters: Grid_connection_PV_NL_PI_380_PIL/Configuration (Active)

Hardware board: STM32F4-Discovery

PIL communication interface: Serial (USART2)

Serial port: COM3

Prolific USB-to-Serial Comm Port (COM3)

__Figure D-0-1__ Selection of STM32F4 board and communication port configuration.

To be able to create the PIL block, go to **Configuration Parameters > Code Generation > Create block** then select **PIL** as illustrated in Figure D-0-2.

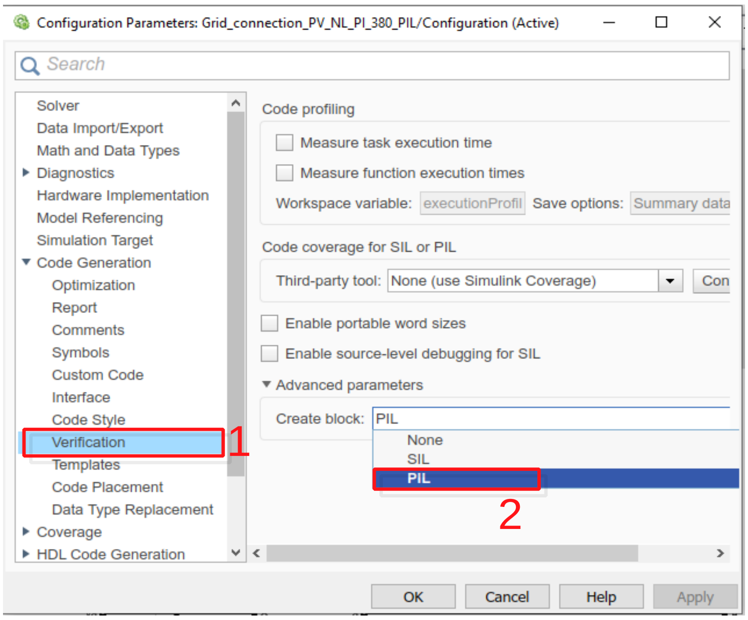

Configuration Parameters: Grid_connection_PV_NL_PI_380_PIL/Configuration (Active)

Code profiling

☐ Measure task execution time

☐ Measure function execution times

Workspace variable: executionProfil Save options: Summary data

Code coverage for SIL or PIL

Third-party tool: None (use Simulink Coverage)

☐ Enable portable word sizes

☐ Enable source-level debugging for SIL

Advanced parameters

Create block: PIL

Figure D-0-2 *Configuring the creation of PIL block.*

To create the PIL block of the control part, do right click on the control block, go to **C/C++ Code**, and then click on **Deploy this subsystem to Hardware**, a new window will pop-up to build the corresponding PIL block. After that, replace the Simulink control block by the new PIL block as shown in Figure D-0-3 (dashed red square).

Finally, run the PIL simulation.

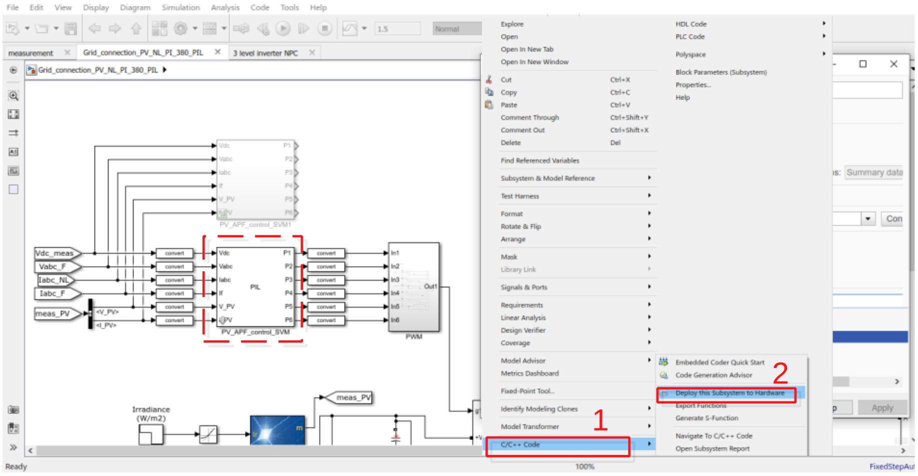

Figure D-0-3 *Building the PIL block.*

Appendix E: Main components of the PCB circuit of the three-Level Three-phase T-type Inverter

➢ Electronic components:

- Power supply circuit: Buffers and opto-coupler all needs DC power supply. In general, for solar systems, DC power supplies are provided using batteries or directly from the panels. However, in this study, components are fed using the grid's power.

  A step down centre-tape transformer that converts the 230 V AC to 17 V AC, a Wheaston bridge for signal rectification, 220 µF/50V smoothing capacitors C1 and C2, to remove the ripples, two regulator ICs to generate the desired voltages +15V and -12V that feeds the opto-couplers by power. Using the same method another circuit of 5 Vdc is implemented to power the buffers.
- Buffers: A buffer with the reference (4LS540 MOTOROLA) is used, its main role is protect the STM32F4 from high current and providing the complementary pulses, 2 of them are used.
- Opto-coupler: The HCNW3120 opto-couplers are ideally suited for driving power IGBTs and MOSFETs used for several applications such as inverters, it transfers electrical signals between two isolated circuits by using light. Opto-isolators has very high insulation voltage so that prevents high voltages from affecting the system receiving the signal.

  Twelve identical opto-couplers are used in our application since we have 12 power MOSFET's.
- Diodes: Three identical diodes for each leg are used in the implementation of the floating power supply with reference (1N4001). These diodes are used to implement the floating power supply of the first opto-coupler in each leg.
- Resistors: Different resistors with variety of values are used.

➢ Power components:

- Power supplies: One power supplies is used of 20V instead of using panels since the inverter working in open loop.
- Polarized capacitors: two of them are used to provide the neutral point for the whole configuration as being able to split the DC voltage, this two capacitors ought to have equal charges.

- Power MOSFET: A MOSET is a type of transistor used for amplifying or switching electronic signals. Twelve MOSFET with the reference of (IRFP32N50K/V DSS=500V- ID=32A) are used in our circuit (4 for each leg), turning on/off of this MOSFET's give us the desired voltage levels. The main advantage of a MOSFET over a regular transistor is that it requires very little current to turn on (less than 1mA), while delivering a much higher current to a load (10 to 50A or more) and has lower switching loss compared with IGBT.

Abstract

Abstract

This thesis is a part of the research carried out on a single-stage three-phase grid-connected photovoltaic (PV) system with active power filtering capability by means of a three-level T-type inverter based-space vector modulation. The system is intended to fulfil many functions simultaneously such as power conversion, maximum power extraction from PV source, harmonic mitigation, and reactive power compensation. In order for the proposed system to achieve these tasks with a good dynamic performance, a new control strategy based on the fuzzy logic controller is developed. Fuzzy control has three main stages and each one requires many settings or a selection of parameters. A new approach to setting the scaling factors which considerably affect the system's response is proposed. Furthermore, a methodology to properly set the fuzzy rules is suggested. The electrical power chain of the system comprises a farm of a PV source, three-level T-type inverter modified space vector switching controlled, inductor filter, non-linear load and the utility grid. To evaluate the performance of the proposed control, a Processor-in-the-Loop (PIL) is performed as a hardware verification of the inverter control algorithm using a low-cost STM32F4 Discovery board, while the power circuit plant is modelled in the host computer using Matlab/Simulink. The obtained results are very satisfactory and confirm the role of each component, especially in terms of maximum power tracking, power quality, unity power factor operation and control robustness.

الملخص

هذه الأطروحة جزء من البحث الذي تم إجراؤه على نظام الخلايا الكهروضوئية (PV) المرتبط بالشبكة الكهربائية ثلاثي الأطوار مع إمكانية ترشيح الطاقة النشطة عن طريق عاكس ثلاثي المستويات من النوع T. يهدف النظام إلى أداء العديد من الوظائف في آن واحد مثل تحويل الطاقة ، استخراج الطاقة القصوى من مصدر الكهروضوئية ، التخفيف التوافقي ، وتعويض الطاقة التفاعلية. من أجل أن يحقق النظام المقترح هذه المهام بأداء ديناميكي جيد ، تم تطوير إستراتيجية تحكم جديدة تعتمد على وحدة التحكم المنطقية الضبابية (FLC). يحتوي التحكم الضبابي على ثلاث مراحل رئيسية وكل مرحلة تتطلب العديد من الإعدادات أو اختيار المعلمات. تم اقتراح نهج جديد لتحديد عوامل القياس التي تؤثر بشكل كبير على استجابة النظام. علاوة على ذلك ، تم اقتراح منهجية لتعيين القواعد الغامضة بشكل صحيح. تشتمل سلسلة الطاقة الكهربائية للنظام على مزرعة من مصدر الكهروضوئية ، وعاكس ثلاثي المستويات من النوع T للتحكم في تبديل ناقل الفضاء المعدل ، ومرشح الحث ، والحمل غير الخطي ، وشبكة المرافق. لتقييم أداء عنصر التحكم المقترح ، يتم إجراء معالج في الحلقة (PIL) لتتحقق من الأجهزة لخوارزمية التحكم في العاكس باستخدام لوحة تحكم STM32F4 منخفضة التكلفة ، بينما تم تصميم محطة دائرة الطاقة في المضيف الكمبيوتر باستخدام Matlab/Simulink . النتائج التي تم الحصول عليها مرضية للغاية وتؤكد دور كل عنصر ، لا سيما فيما يتعلق بأقصى تتبع للطاقة وجودة الطاقة وتشغيل عامل الطاقة الموحد وقوة التحكم.

Résumé

Cette thèse fait partie de la recherche menée sur un système photovoltaïque (PV) triphasé connecté au réseau électrique avec une capacité de filtrage de puissance active au moyen d'une modulation vectorielle spatiale basée sur un onduleur de type T à trois niveaux. Le système est destiné à remplir de nombreuses fonctions simultanément, telles que la conversion de puissance, l'extraction de puissance maximale de la source PV, l'atténuation des harmoniques et la compensation de la puissance réactive. Afin que le système proposé réalise ces tâches avec de bonnes performances dynamiques, une nouvelle stratégie de contrôle basée sur le contrôleur à logique floue est développée. La commande floue comporte trois étapes principales et chacune nécessite de nombreux réglages ou sélections de paramètres. Une nouvelle approche pour définir les facteurs d'échelle qui affectent considérablement la réponse du système est proposée. En outre, une méthodologie pour définir correctement les règles floues est suggérée. La chaîne d'alimentation électrique du système comprend un parc d'une source PV, un onduleur à trois niveaux de type T à modulation vectorielle spatiale modifiée, un filtre inducteur, une charge non linéaire et le réseau électrique. Pour évaluer les performances du contrôle proposé, un processeur dans la boucle (PIL) est effectué en tant que vérification matérielle de l'algorithme de contrôle de l'onduleur à l'aide d'une carte de STM32F4 Discovery, tandis que la centrale électrique est modélisée dans l'hôte ordinateur avec Matlab/Simulink. Les résultats obtenus sont très satisfaisants et confirment le rôle de chaque composant, notamment en termes de poursuite de puissance maximale, de qualité de puissance, de fonctionnement à facteur de puissance unitaire et de robustesse de commande.